
Analysis of New Cryogenic Detectors with Light Nuclei to Extend the CRESST Dark Matter Sensitivity

Anna Bertolini



München 2024

Analysis of New Cryogenic Detectors with Light Nuclei to Extend the CRESST Dark Matter Sensitivity

Anna Bertolini

Dissertation
der Fakultät für Physik
der Ludwig-Maximilians-Universität
München

vorgelegt von
Anna Bertolini
aus Mailand

München, den 4. April 2024

This work is licensed under **CC BY 4.0**.

Erstgutachter: Prof Dr. Otmar Biebel
Zweitgutachter: PD Dr. Stafan Kluth
Tag der mündlichen Prüfung: 28. Mai 2024

Contents

1	Introduction to Dark Matter	11
1.1	Cosmological Framework	11
1.1.1	Thermal history of the Universe	11
1.1.2	Mathematical description of an expanding Universe	13
1.2	Motivation for dark matter	14
1.2.1	Rotational velocity of galaxies	14
1.2.2	Cosmic Microwave Background	16
1.2.3	The bullet cluster	16
1.3	Dark Matter Candidates	18
1.3.1	Thermal production	19
1.3.2	Non-thermal production	22
1.3.3	Summary	24
2	Dark Matter Detection	25
2.1	Signal in Direct Detection	25
2.1.1	Dark Matter Halo Model	25
2.1.2	Expected Signal	26
2.1.3	Differential Rate of Elastic scattering	27
2.1.4	Scattering cross-section	28
2.1.5	Expected Recoil Spectrum	30
2.2	Background in Direct Detection	30
2.2.1	Neutrons and Neutrinos	30
2.2.2	Muons	31
2.2.3	Gammas, Electrons, Alphas	32
2.2.4	New Backgrounds	32
2.3	Current Status of Dark Matter Searches	32
2.3.1	Spin-Independent Searches	32
2.3.2	Spin-Dependent Searches	33
3	The CRESST Experiment	35
3.1	Signal read-out	35
3.1.1	Cryogenic Calorimeters	35
3.1.2	The Transition Edge Sensor	36
3.1.3	Thermal Model	37
3.1.4	Maximization of the Signal	40

3.2	The CRESST Facility	41
3.2.1	Backgrounds at LNGS	42
3.2.2	Cryostat and Shielding	42
3.2.3	CRESST-III Detector Modules	43
3.2.4	Resistance Read-out	45
3.2.5	Temperature Control	46
3.2.6	Data Acquisition	47
3.3	Latest Run - Run36	48
3.3.1	Goal of the Run	48
3.3.2	Run36 Detector Modules	48
4	Data Acquisition and Analysis	51
4.1	Raw Data Processing	51
4.1.1	The Optimum Filter	52
4.1.2	Triggering Process	54
4.1.3	Event Building	57
4.1.4	Calculation of Main Parameters	59
4.2	Low Level Analysis	61
4.2.1	Data Selection	61
4.2.2	Energy Determination	64
4.2.3	Efficiency Estimation	69
4.3	High Level Analysis	71
4.3.1	Definition of ROI	72
4.3.2	Exclusion Limits Calculation	73
5	Lithium-Based Detectors	77
5.1	Tested Lithium-Based Crystals	78
5.1.1	Lithium Molybdate	78
5.1.2	Lithium Aluminate	79
5.1.3	Lithium Fluoride	81
5.1.4	Choice of the Material	81
5.2	Analysis of Run36	81
5.2.1	Detector Design	81
5.2.2	Data Taking and processing	82
5.2.3	Calibration	83
5.2.4	Data Selection	84
5.2.5	Energy Spectrum	86
5.2.6	Efficiency Estimation	87
5.3	DM Results	88
5.3.1	Exclusion Limits	88
5.3.2	Comparison of Li1 and Li2 Modules	88
5.4	Conclusions	89
5.5	Outlook	90

6	Diamond Detectors	93
6.1	Experimental Setup	94
6.1.1	Detector Design	94
6.1.2	Data Taking and Processing	96
6.2	Detector performance	97
6.2.1	Calibration Factor	97
6.2.2	Baseline Resolution Estimation	98
6.2.3	Energy Threshold	100
6.3	Dark Matter results	101
6.3.1	Data Cleaning	102
6.3.2	Data Calibration	105
6.3.3	Efficiency Estimation	106
6.3.4	Comparison of Energy Spectra	109
6.3.5	Exclusion Limits	111
6.4	Conclusions	111
6.4.1	Evaluation of Results	111
6.4.2	Outlook	113
7	Conclusion and Outlook	115

Zusammenfassung

Seit Jahrzehnten sieht sich die wissenschaftliche Gemeinschaft mit mehreren astronomischen Beobachtungen konfrontiert, die auf die Existenz einer unbekannt, nicht leuchtenden Materie hinweisen, die heute als dunkle Materie bezeichnet wird. Es wurden mehrere Theorien über die Natur dieser neuen Materie aufgestellt. Die Theorie, die in der wissenschaftlichen Gemeinschaft die größte Akzeptanz genießt, ist die Teilchentheorie, bei der angenommen wird, dass die dunkle Materie aus einem oder mehreren Teilchen besteht, die im Standardmodell nicht vorgesehen sind. Es wurden mehrere Kandidaten vorhergesagt, die ein breites Spektrum an Massen und Wechselwirkungen mit den Teilchen des Standardmodells abdecken. Daher werden die experimentellen Bemühungen zur Untersuchung jedes möglichen Kandidaten auf zahlreiche Experimente mit unterschiedlichen Nachweisansätzen verteilt.

Kryogenexperimente spielen eine wesentliche Rolle bei der Untersuchung potenzieller Teilchen der dunklen Materie mit Massen unterhalb des GeV-Bereichs. Ihr typischer Nachweisansatz besteht darin, die elastische kohärente Streuung eines Teilchens aus dunkler Materie an einem Zielkern mit Hilfe von extrem empfindlichen Kalorimetern zu identifizieren. Eines dieser Experimente ist das CRESST-Experiment, bei dem die von potenziellen Teilchen der dunklen Materie deponierte Energie als Temperaturanstieg in einem Zielkristall mit supraleitenden Phasenübergangsthermometern (*Transition Edge Sensors* - TES) gemessen wird. Die bemerkenswert niedrigen Energieschwellen, die mit diesen Sensoren erreicht werden, haben die Empfindlichkeit von CRESST für dunkle Materie im Sub-GeV-Bereich an vorderster Front etabliert.

Einer der Vorteile von kryogenen Kalorimetern ist die Möglichkeit, verschiedene Materialien als Absorber zu verwenden. Wenn man die Sensitivität für noch niedrigere Massen dunkler Materie anstrebt, sind daher Zielkristalle mit leichten Kernen die beste Wahl, da sie kinematisch bevorzugt sind, die Streuung von Teilchen mit geringer Masse zu untersuchen.

In dieser Arbeit wird zunächst eine kurze Einführung in die Dunkle Materie und ihren Nachweis in Kapitel 1 und 2 gegeben, gefolgt von einer Darstellung des CRESST-Experiments in Kapitel 3 und seiner Analysemethoden in Kapitel 4. Nach dieser Einführung wird die Verwendung von zwei leichten Elementen in kryogenen Kalorimetern untersucht: Lithium und Kohlenstoff.

In Kapitel 5 wird die erste unterirdische Messung eines Kristalls auf Lithiumbasis, in Form von Lithiumaluminat, vorgestellt. Lithium ist das leichteste Element, das in die für die CRESST-Technologie erforderliche kristalline Struktur eingebettet werden kann. In Verbindung mit einer niedrigen Energieschwelle haben solche

Kristalle daher das Potenzial, bei der Suche nach leichter dunkler Materie höchste Empfindlichkeit zu bieten. Dank des Kerndrehimpulses im Grundzustand, der von 0 verschieden ist, können nicht nur die typischen spinunabhängigen Wechselwirkungen untersucht werden, sondern auch spinabhängige. Das Potenzial dieses Materials wird in dieser Arbeit bestätigt, indem die weltweit führenden oberen Grenzwerte für den spinabhängigen Dunkle-Materie-Nukleon-Wirkungsquerschnitt durch elastische Streuung, die mit einem Lithiumaluminat-Kristall erzielt werden konnten, vorgestellt werden.

In Kapitel 6 wird eine Messung mit Diamantkristallen vorgestellt, die die erste Verwendung dieses Materials als kryogenes Kalorimeter für die Suche nach dunkler Materie darstellt. Heutzutage besteht ein großes Interesse an diesem Material in kryogenen Experimenten, nicht nur wegen seines leichten Kerns, sondern auch, weil es die notwendigen Eigenschaften aufweist, um beispiellose Energieschwellen zu erreichen. In dieser Arbeit wird gezeigt, wie mit einer Proof-of-Principle-Messung die vorhergesagten niedrigen Energieschwellen erreicht wurden und konkurrenzfähige obere Grenzen für den spinunabhängigen Dunkle-Materie-Nukleon-Wirkungsquerschnitt der elastischen Streuung gesetzt werden konnten. Die möglichen weiteren Verbesserungen für eine vollständige Nutzbarmachung der beiden vorgestellten innovativen Materialien werden ebenfalls kurz skizziert.

Abstract

For decades, the scientific community has been faced with several astronomical observations pointing to the existence of an unknown non-luminous matter, now referred to as dark matter. Several theories have been advanced regarding the nature of such a type of new matter. The theory that holds the highest acceptance within the scientific community lies in the particle framework, where dark matter is hypothesized to be composed of one or more particles not foreseen in the standard model. Multiple candidates have been predicted which cover a broad range of masses and interaction types with the standard model particles. Therefore, the experimental effort to investigate each possible candidate is shared between numerous experiments adopting different detection approaches.

Cryogenic experiments have engaged an essential role in probing potential dark matter particles with sub-GeV masses. Their typical detection approach is to identify the elastic coherent scattering of a dark matter particle off a target nucleus by means of extremely sensitive calorimeters. One of these is the CRESST experiment, which measures the energy deposit generated by potential dark matter particles as a temperature rise in a target crystal with superconducting thermometers, called transition edge sensors (TES). The remarkably low energy thresholds achieved with these sensors have established the sensitivity of CRESST to sub-GeV dark matter at the forefront.

One of the advantages of cryogenic calorimeters is the possibility to employ different materials as absorbers. Therefore, when aiming at sensitivity to low dark matter masses, targets with light nuclei represent the best choice, as they are kinematically favored.

In this thesis, a brief introduction to dark matter and its detection is outlined in chapters 1 and 2, followed by a presentation of the CRESST experiment in chapter 3 and its analysis chain in chapter 4. After this introduction, this thesis explores the use of two light elements in cryogenic calorimeters: lithium and carbon.

Chapter 5, presents the first underground measurement of a lithium-based crystal, in the form of lithium aluminate. Lithium is the lightest element that can be embedded in the crystalline structure the CRESST technology requires. Therefore, combined with a low energy threshold, such crystals have the potential to provide ultimate sensitivity to light dark matter searches. Thanks to its nuclear ground state angular momentum that is different from 0, not only the typical spin-independent interactions can be probed, but also spin-dependent ones. The potential of lithium is confirmed in this thesis by presenting the world-leading upper limits on the elastic scattering spin-dependent dark

matter-nucleon cross-section that could be achieved with a lithium aluminate crystal. In chapter 6, a measurement employing diamond crystals is presented, which represents the first use of this material as a cryogenic calorimeter for a dark matter search. Nowadays, there is a widespread interest in this material within cryogenic experiments, not only because of its light nucleus but also because it features the necessary characteristics to achieve unparalleled energy thresholds. In this work, it is shown how, with a proof-of-principle measurement, the predicted low energy thresholds were achieved and competitive upper limits on the elastic scattering spin-independent dark matter-nucleon cross-section could be set. The possible further improvements for a full exploitation of the two innovative materials presented are also briefly outlined.

Chapter 1

Introduction to Dark Matter

In the last century, scientists have been faced with several unexpected astronomical observations that cannot be explained with the standard model (SM) and general relativity. Nowadays, the best explanation for these cosmological observations is in the particle framework, where it has been hypothesized the existence of a new class of particles called dark matter (DM). Many years after the first hypothesis of its existence [1], the scientific community has yet to find an answer to the nature of this matter. Nonetheless, over the years, physicists succeeded in gathering some characteristics of DM and even in estimating its abundance, 26% of the energy density in the Universe. Looking at the magnitude of this share, it is easy to understand how the answer to the DM puzzle became progressively crucial.

In this chapter, a brief introduction to DM will be given, starting with the cosmological framework in which DM should be included. The most striking observations that align with the existence of an unknown matter will then be described. To conclude, a few examples of DM candidates will be presented.

1.1 Cosmological Framework

1.1.1 Thermal history of the Universe

Before looking at the observations that motivate the existence of DM, it is worth taking a step back and looking at the history of the Universe, as foreseen by the standard cosmological model [2]. To simplify it, the 13.8 billion-year-long [3] history of the Universe can be divided into three phases, based on the composition of the Universe: the radiation dominated, the matter dominated, and finally, the Lambda dominated era (see figure 1.1) [4].

The **radiation dominated era** covers the first fifty thousand years of the Universe. During the first seconds of the Universe formation, protons and neutrons were in thermal equilibrium, coupled via weak interactions:

$$n + \nu_e \longleftrightarrow p + e^- \quad , \quad n + e^+ \longleftrightarrow p + \bar{\nu}_e \quad (1.1)$$

Due to the expansion of space, the temperature of the Universe decreased continuously. Once $k_B T < 1.3$ MeV, the conversion from protons into neutrons was not energetically

possible anymore. Neutrons instead, being slightly heavier than protons, continued decaying into protons. The number of neutrons decayed exponentially until it eventually froze out, reaching a number density smaller than the one of protons [5]:

$$\frac{n_n}{n_p} = 0.18 \quad (1.2)$$

At this stage, protons and neutrons were constantly hit by highly energetic photons. However, once the temperature dropped at $k_B T < 0.06$ MeV, these photons became low energetic enough for neutrons and protons to create bound states, such as Deuterium [6]:



With the continuous expansion of the Universe, the matter and radiation energy densities continued decreasing. While the energy density of matter decreased inversely proportional to the volume ($\rho_m \propto a^{-3}$), the energy density of radiation decreased as $\rho_r \propto a^{-4}$ due to the additional loss in energy given by the redshift of individual relativistic particles [4]. This resulted in a faster decay of the radiation energy density over time. Due to this difference, after around 50,000 years, the matter density in the Universe exceeded the radiation density, and the Universe entered the **matter dominated era**. During this era, the Universe continued expanding and cooling down. 380,000 years after the Big Bang, the process of **recombination** began, where photons were not energetic enough to ionize the lightest possible atoms (for Hydrogen $E_{ion} = 13.6$ eV) and the first atoms started to form. The Universe became neutral and photons started to move freely, resulting in the Cosmic Microwave Background (CMB) (described in more detail in section 1.2.2). This process is referred to as **decoupling**. At this stage structures, such as galaxies and clusters, began forming from small matter over-densities. The evolution of these matter densities over time could strongly vary, depending on whether DM was relativistic or non-relativistic in the early Universe. Due to its high velocity, relativistic DM, also referred to as Hot Dark Matter (HDM), requires a much larger over-density to collapse into a gravitational potential. Therefore, small-scale structures cannot form from HDM but large-scale ones can. Smaller structures would then form later, from the fragmentation of large structures. This means that a HDM type would have led to a **top-down** structure formation. CDM instead, having smaller velocities, would have led to the formation of small structures first. Bigger structures would have then formed later, resulting in a **bottom-up** structure formation. Following this observation, it is possible to infer whether DM is hot or cold by studying the structure formation of the Universe today. For this purpose, the scientific community has conducted N-body simulations that predict which structures would be present today based on a hot or cold DM type. The comparison of these simulations with large-scale surveys today clearly favor a CDM scenario [7]. To conclude, we now live in a **cosmological constant dominated era**. This constant Λ represents the dark energy that is supposed to be causing an accelerated expansion of the Universe.

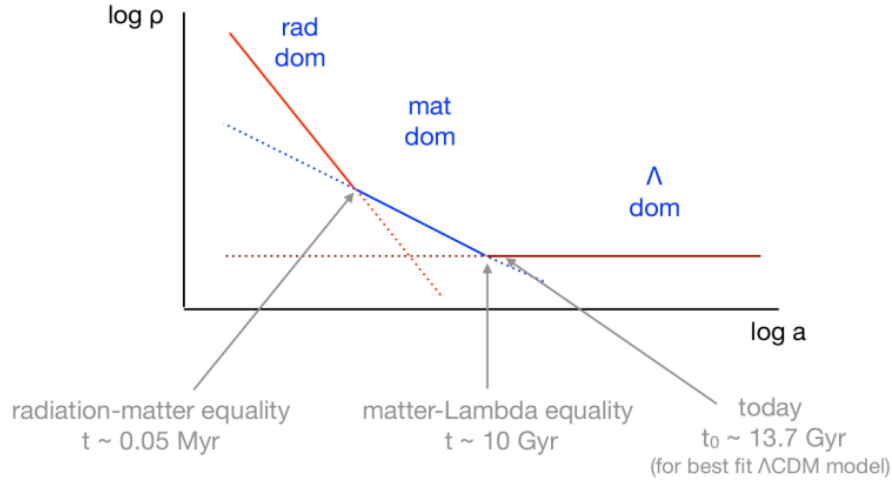


Figure 1.1: Evolution of the density of the Universe. Figure reproduced from [4].

1.1.2 Mathematical description of an expanding Universe

In modern cosmology, the description of the evolution of the Universe, the Standard Cosmological Model, is based on general relativity and on the *cosmological principle*, which postulates the Universe as an isotropic and homogeneous space. The Universe as an isotropic and homogeneous expanding space is described by the **Friedmann equation**:

$$\left(\frac{\dot{a}}{a}\right)^2 = \frac{8\pi G}{3}\rho - \frac{kc^2}{a^2} + \frac{\Lambda c^2}{3} \quad (1.4)$$

where Λ is the cosmological constant, ρ is the total energy density of the Universe, and k is a factor for the curvature of space. For the latter parameter, three different values are possible that correspond to three possible curvatures of space

$$k = \begin{cases} -1, & \text{spherical space} \\ 0, & \text{flat space} \\ +1, & \text{hyperbolic space (saddle)} \end{cases} \quad (1.5)$$

This equation therefore tells that the expansion rate of the Universe depends on its geometry (curvature) and content (energy density and cosmological constant).

The expansion rate of the Universe, first observed by Hubble, is characterized by the **Hubble rate** $H(t) = \frac{\dot{a}}{a}$, named after him. With the Hubble constant H_0 , which denotes the expansion rate at the present time, one can define a critical density as the energy density of the Universe in the case of $k=0$ and $\Lambda=0$:

$$\rho_c = \frac{3H_0^2}{8\pi G} \quad (1.6)$$

introducing the **density parameter** Ω , which describes the energy density relative to the critical density

$$\Omega = \frac{\rho}{\rho_c} \quad (1.7)$$

the Friedmann equation can then be rewritten as

$$\frac{kc^2}{a^2 H^2} = \Omega - 1 \quad (1.8)$$

From this equation, it is evident that ρ determines the sign of k : for $\rho < \rho_c$ k is negative, for $\rho = \rho_c$, k vanishes, and for $\rho > \rho_c$ k is positive. In terms of the critical density, it is common to distinguish the separate contributions to the energy density of the Universe

$$\Omega = \Omega_m + \Omega_r + \Omega_\Lambda \quad (1.9)$$

where Ω_m describes the contribution to the energy density given by matter, Ω_r due to radiation, and Ω_Λ due to the cosmological constant. These three values can be measured at the present time and, as already mentioned, Ω_Λ is the currently dominating contribution. The parameterization of the expanding Universe, as described before, that accounts for a cosmological constant Λ and structure formation due to cold dark matter, is indicated as the Λ CDM model. In this model, Ω_m is given by the contribution of two different types of matter:

$$\Omega_m = \Omega_b + \Omega_c \quad (1.10)$$

where Ω_b is the contribution of baryonic matter, which could also be called visible matter, and Ω_c the contribution of cold dark matter. The observations that lead to the postulation of such a type of matter are described in the next section.

1.2 Motivation for dark matter

While in the 1930s the idea of an expanding Universe was already strongly supported by some observational evidence [8], the concept of dark matter only began to gain attention. In 1937, Zwicky calculated the velocity of galaxies beyond the central bulge of the *Coma cluster*, which were significantly higher than the ones that could be gravitationally bound by the visible mass in the cluster [1]. This observation could have been explained by assuming an enormous amount of non-luminous matter in the galaxies. However, only in the second half of the 20th century, the idea of the presence of an invisible matter became more concrete, thanks to various observations that could altogether be explained by the existence of dark matter.

1.2.1 Rotational velocity of galaxies

In 1970, Rubin and Ford measured the rotational velocity of the Andromeda Nebula and found that the speed of stars does not fall beyond the central bulge of the galaxy but

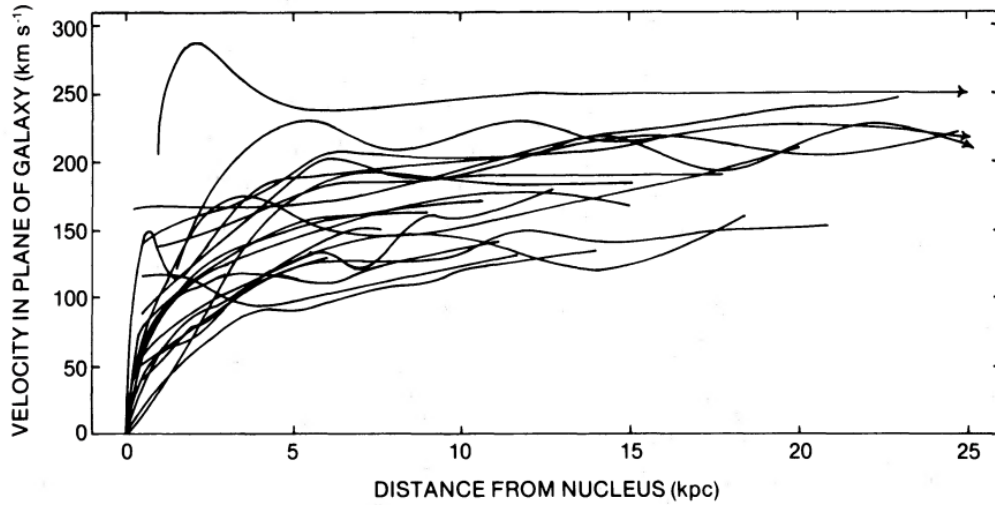


Figure 1.2: Superposition of rotational curves measured in 21 galaxies. The velocity of stars in the spiral galaxy is given as a function of distance to the galactic center. Picture reproduced from [10].

remains constant [9] (the rotational curve can be seen in 1.2). This unexpected result was then reinforced in 1980 when the same behavior was measured in 21 other different galaxies. With this data, they finally deduced that "non-luminous matter exists beyond the optical galaxy" [10]. How they arrived at this conclusion can be understood using simple Newtonian gravity. Assuming that most of the mass is concentrated in the central bulge at a distance r larger than the radius of the bulge, one expects

$$v_{rot} = \sqrt{\frac{GM}{r}} \sim \frac{1}{\sqrt{r}} \quad (1.11)$$

where G is the gravitational constant, and M is the mass in the bulge. What Rubin and Ford measured, namely

$$v_{rot} = \sqrt{\frac{GM}{r}} \propto \text{constant} \quad (1.12)$$

points to the relation $M(r) \propto r$, that implies, if Newtonian gravity is correct,

$$\rho(r) \propto \frac{1}{r^2} \quad (1.13)$$

This means that the observed spiral galaxies are surrounded by an invisible **dark matter halo** with density $\rho(r) \propto \frac{1}{r^2}$.

This observation represents one of the strongest arguments for the existence of a new type of matter.

1.2.2 Cosmic Microwave Background

In the early 90s, the scientific community's confidence in the existence of DM grew stronger thanks to the first measurements of temperature anisotropies in the Cosmic Microwave Background (CMB) [11]. This observation not only pointed to the existence of a non-luminous matter but also quantified its presence in the Universe. To understand how this information could be inferred, it is important to recognize that the CMB is a black body radiation composed of photons that started moving freely in space at times of decoupling (see section 1.1.1). Therefore, with the CMB one can deduce information about the Universe exactly at that time. For instance, the fluctuations in temperature (with respect to the black body temperature of $T = 2.7255$ K [12]) can be traced back to density inhomogeneities at the time of decoupling.

To visualize this relevant information, one can create a map of the Universe regarding the intensity of photons at the time of decoupling. The correlations between separate parts of the Universe can be modeled with progressively finer angular scales using spherical harmonics (Y_ℓ^m). The result can be seen in figure 1.3.

The peaks present at intermediate ℓ values can be used to infer the density parameters for baryonic matter and dark matter, as their height is strongly correlated to the amount of baryonic/dark matter at the time of decoupling. They originate from oscillations in the photon fluid in the early Universe, called *Baryonic Acoustic Oscillations* (BAOs). At that time, anisotropies in the density of space-time generated gravitational potentials in which the charged photon-baryon fluid was trapped. Such gravitational wells were primarily caused by DM, with which the fluid did not interact. The electromagnetic force of this plasma created an outward pressure that competed with the gravitational potential. This competition resulted in oscillating acoustic waves of the fluid's propagation that can be recognized in the CMB and with which the following parameters could be derived [12]:

$$\begin{aligned}
 \Omega_b h^2 &= 0.02237 \pm 0.00015 \\
 \Omega_c h^2 &= 0.1200 \pm 0.0012 \\
 h &= 0.674 \pm 0.005 \\
 \Omega_\Lambda &= 0.685 \pm 0.007
 \end{aligned}
 \tag{1.14}$$

These numbers state that only 4.9 % of the energy density in the Universe is given by baryonic mass, 26.5 % by dark matter, and 68.5 % by dark energy.

It is also important to mention that the CMB power spectrum measured by telescopes like Planck, WMAP, etc. fits significantly well with the expectations of the Λ CDM model, strengthening therefore the hypothesis that dark matter is cold (non-relativistic).

1.2.3 The bullet cluster

A further observation that supports the existence of dark matter is given by the collision of two galaxy clusters (1E 0657-56), commonly referred to as *the bullet-cluster* [13]. Beyond thousands of galaxies, these clusters also contain hot gas and dark matter.

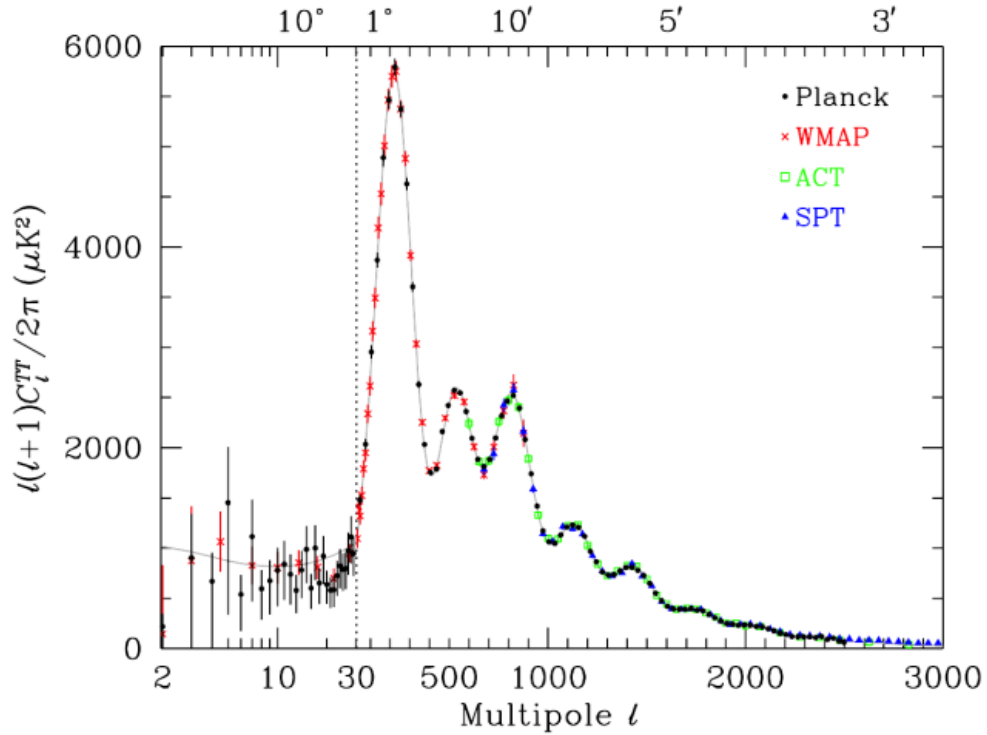


Figure 1.3: Power spectrum of the Cosmic Microwave Background (CMB). Figure reproduced from [12]. This plot shows the result from four different telescopes: Planck (black), WMAP (red), ACT (green), and SPT (blue).

The mass distribution of the hot gas can be reconstructed thanks to **X-rays** emitted by electron bremsstrahlung. The gravitational potential is instead quantified with **gravitational lensing** (for more details, see for example [14]). Figure 1.4 shows the mass distributions of the hot gas (pink), gravitational potential (blue), and luminous galaxies. The collision point of these galaxy clusters can be recognized by the shock shape of the hot gas accumulation on the right, which is clearly moving away from the one to the left (therefore the name *bullet*). From this picture it is therefore evident that the hot gas (composed of baryonic, ordinary matter) of the two clusters interacted with each other, thereby slowing down compared to stars that are further away from the collision point. Thanks to the gravitational lensing, it can be recognized that dark matter populates two regions coincident with the visible galaxies (blue in the picture). This means that the two DM distributions have passed through each other and through the gas without experiencing any friction. This picture is therefore a direct indication that dark matter interacts at most, very weakly with visible matter as well as among itself. This observation has been used to set limits on the DM self-interaction cross-section [15].

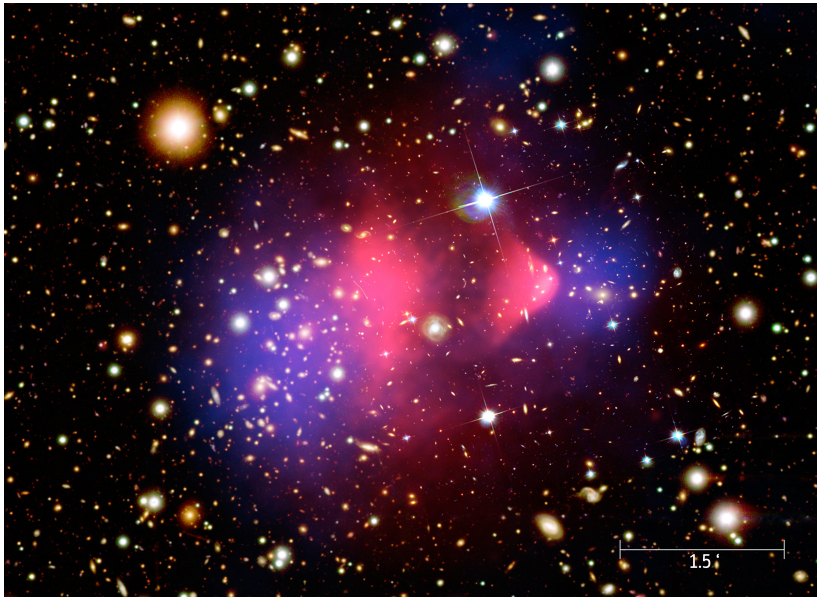


Figure 1.4: The *bullet cluster*. In this figure, three pictures are superimposed. The first layer is the optical image representing the distribution of stars. The distribution of the hot gas has been inferred with X-rays and is represented in pink. The blue shaded part represents the gravitational potential which has been obtained with gravitational lensing. Figure taken from [16].

1.3 Dark Matter Candidates

The three independent observations at different scales described above, point to the existence of an unknown type of matter. While the exact nature of this remains unknown, a few characteristics became evident thanks to these observations. Firstly, this type of matter is **non-luminous**. Secondly, the CMB and N-body simulations favor a **non-relativistic** (cold) DM. Furthermore, dark matter particles should be **stable** or very long-living (in the order of the age of the Universe) [17] since the aforementioned observations show that DM is present today (e.g. from rotational curves) and was already present in the early Universe (e.g. from CMB). Moreover, observations such as the bullet cluster show that the coupling of DM to baryonic matter should be very weak (weaker than the one to the Weak force), if at all existent. From the bullet cluster, it can also be concluded that the self-interaction of DM results to be very weak. Finally, since every observation shows that DM interacts gravitationally, it should be **massive**. The possible mass of DM covers a range from the Planck mass ($\sim 10^{18}$ GeV) down to 10^{-21} eV. Several paradigms have been theorized to describe potential DM candidates. Depending on the model, candidates cover different parts of this total mass range. An overview can be found in figure 1.5. These DM candidates can be categorized depending on their production mechanism and will be described in the following.

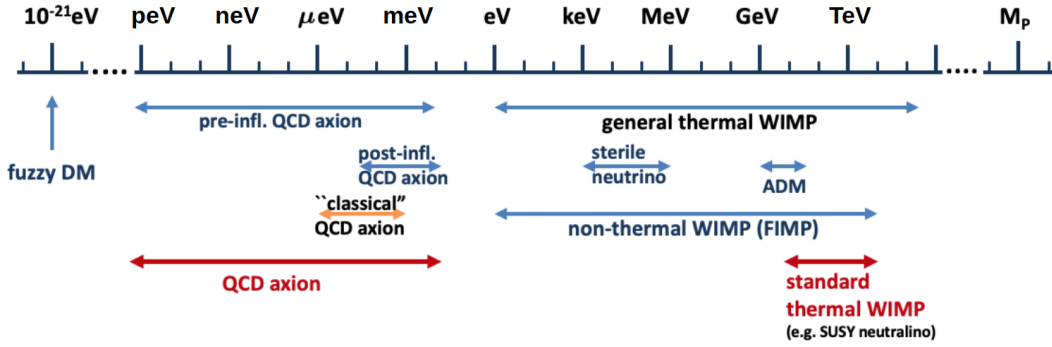


Figure 1.5: Mass range of dark matter with possible candidates. Figure reproduced from [17].

1.3.1 Thermal production

One possibility for the production of the current DM relic is through a thermal process. In this scenario, DM was thermally coupled to the baryonic plasma in the early Universe, having a continuous exchange of particles in both directions

$$DM + DM \longleftrightarrow SM + SM \quad (1.15)$$

Once the Universe cooled down to temperatures T below the dark matter mass m_X , the dark matter production became suppressed, while the annihilation continued. The number density of dark matter would have eventually dropped to zero if it were not for the expansion of the Universe that limited the DM annihilation process. Therefore, DM eventually reached a constant relic density [18] (the Ω_c value measured by the CMB). This mechanism is referred to as **freeze-out**. A sketch of this process can be seen in figure 1.6. It can be seen that the final relic density Ω_c depends on the thermally averaged cross-section of the DM annihilation (the higher the cross-section, the lower the relic density). This concept can be understood, starting from the definition of freeze-out as the moment at which the annihilation rate is equal to the expansion rate. Together with the first Friedmann equation 1.4 and $G = M_{pl}^{-2}$ one can obtain the relation

$$n_f \langle \sigma_A v \rangle = H \propto \frac{T^2}{M_{pl}} \quad (1.16)$$

where n is the number density of the dark matter particle, $\langle \sigma_A v \rangle$ is the thermally averaged annihilation cross-section and H is the Hubble parameter. With equation 1.16, the dependence of the thermal relic density on the annihilation cross-section can be approximated as

$$\Omega_c = \frac{m_X n_0}{\rho_c} = \frac{m_X T_0^3}{\rho_c} \frac{n_0}{T_0^3} \sim \frac{m_X T_0^3}{\rho_c} \frac{n_f}{T_f^3} \sim \frac{x_f T_0^3}{\rho_c M_{Pl}} \langle \sigma_A v \rangle^{-1} \quad (1.17)$$

where it has been assumed that n/T^3 today is equal to the value at the time of freeze-out, x_f is defined as $x_f = m_X/T_f$ and can be considered as constant (see for example [19]).

The type of self-annihilation process that leads to freeze-out relic density Ω_c can vary, and depending on this process different DM candidates are defined.

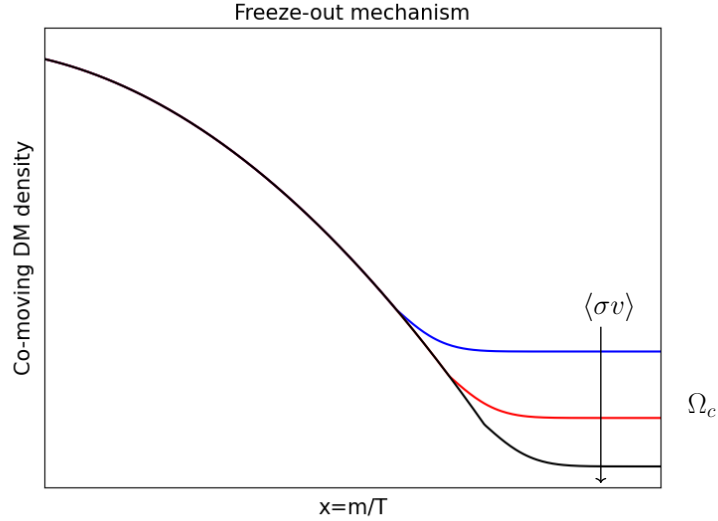


Figure 1.6: Illustration of the freeze-out mechanism. The y-axis shows the particle density (before freeze-out) and the constant relic DM density (after freeze-out). The stronger the annihilation cross-section, the lower is the final DM density. Therefore, in this plot black shows the case of the strongest cross-section and blue the weakest.

Classical WIMPs

For many years, the Weakly Interactive Massive Particle (WIMP) has been considered the DM candidate par excellence. The notoriety of this candidate originates from the suggestive possibility of solving the DM problem with new physics at the electroweak scale. In fact, if we consider the self-annihilation process to be a "two-to-two" DM-SM exchange, then the relation of the annihilation cross-section and the DM mass is:

$$\sigma_A \propto \frac{\alpha^2}{m_\chi^2} \quad (1.18)$$

where α represents the coupling to the SM sector. When considering a coupling of the Weak force, the measured value of Ω_c predicts masses in the Weak range. This coincidence is colloquially known as *the WIMP miracle*. Following equation 1.17, the mass range predicted by the WIMP miracle is constrained by the dark matter density measured by the CMB (see equation 1.14) and by the fixed Weak force coupling. If one assumes that the WIMP is the only component of the dark matter density, then this range is 100 GeV-1 TeV [18].

General WIMPs

The interaction between DM and the SM via the Weak force has been almost completely ruled out. Nonetheless, there is also the possibility that DM communicates with the SM sector via an unknown force carrier. Abandoning the constraint of the Weak coupling, a more general WIMP paradigm is obtained wherein the weaker the coupling via this force carrier is, the lighter are the predicted DM masses. In contrast to the classical WIMP, the general WIMP paradigm does not predict a narrow mass range. Nonetheless, it is important to notice that a general lower and upper bound exists, given the measured thermal relic density. The lower bound arises from the requirement that the thermal relic is non-relativistic at freeze-out [20]. The upper bound, instead, originates from the Unitarity argument ($g^2 < 4\pi$), where g is the coupling from DM to the SM particles [21].

This general WIMP scenario postulates the existence of force carriers beyond the SM, generally referred to as **dark sector** carriers. A special paradigm of the dark sector is the **dark photon**, which can undergo kinetic mixing with the SM photon [17].

SIMPs

The WIMP paradigm assumes that the relic DM particles originate from a 2-body DM-SM interaction. However, this is not the only way in which the DM relic might have arisen. Another possibility would for instance be an n-body self annihilation such as

$$DM + DM + \dots + DM \rightarrow DM + DM \quad (1.19)$$

This self-annihilation, colloquially referred to as **cannibalism**, would significantly alter the predicted mass range of candidates. For instance, if one assumes a $3 \rightarrow 2$ process, the annihilation cross-section would be proportional to

$$\langle \sigma v^2 \rangle_{3 \rightarrow 2} = \frac{\alpha_{eff}^3}{m_\chi^5} \quad (1.20)$$

with the crucial caveat that, in this case, α_{eff} denotes a self-coupling and not a coupling to the SM, as it was for the WIMP candidate [22]. Moreover, it is crucial to note that the calculations of this paradigm are based on a thermal equilibrium between DM and the SM. A strong self-interaction of SIMPs completely decoupled from the baryonic matter would heat up the dark sector significantly. Hence, a form of coupling to the SM has to exist to ensure thermal equilibrium. By all means, such a coupling would also allow for a $DM + DM \rightarrow SM + SM$ annihilation process, as foreseen by the WIMP paradigm. Therefore, the requirement that the DM self-annihilation process is governed by the $3 \rightarrow 2$ DM self-interaction represents an additional constraint to the DM-SM coupling. These limits are visualized in figure 1.7

ADM

An additional hypothesis for the generation of the DM relic could be an initial asymmetry between DM particles and antiparticles. This paradigm is referred to as

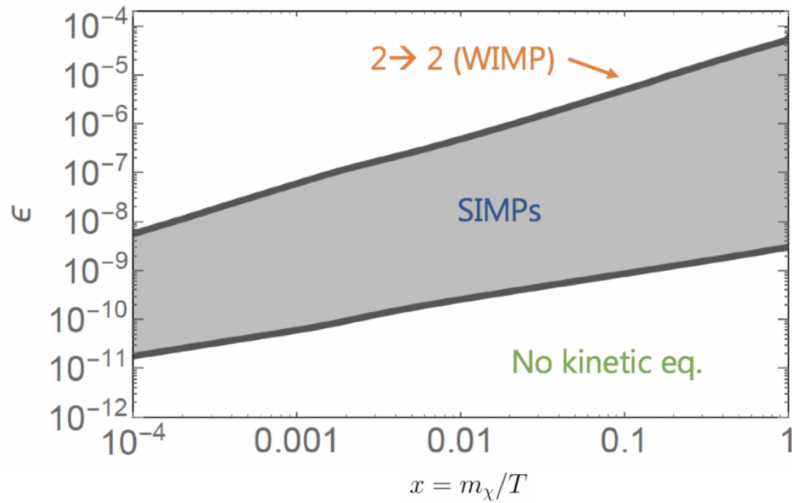


Figure 1.7: Range of DM-SM coupling predicted by the SIMP paradigm as a function of DM mass. The upper bound on the coupling originates from the requirement that the DM relic production is due to DM self-interaction. The lower bound is given by the requirement that thermal equilibrium between the dark and the SM sector exists. Figure reproduced from [22].

Asymmetric Dark Matter (ADM). In such a scenario, DM particles would have a new (dark) charge that distinguishes DM particles and antiparticles. These particles would annihilate until a point in time where this initial asymmetry has grown excessively and antiparticles barely exist anymore.

Since the baryonic relic density is also expected to grow from an initial asymmetry between matter and antimatter, ADM would provide an explanation for the similarity of the matter densities

$$\Omega_{DM} \approx 5\Omega_B \quad (1.21)$$

pointing to a common origin of the cosmological evolution of DM and Baryons [23]. For ADM, particles with a high annihilation rate would be needed, and since the annihilation cross-section is

$$\sigma_A \sim \frac{\alpha^2}{m_\chi^2} \quad (1.22)$$

this would lead to low masses. Many ADM models predict DM masses in the range of 1-15 GeV [23].

1.3.2 Non-thermal production

It is also plausible that the current DM density was generated by a non-thermal mechanism. Several paradigms for DM candidates with different non-thermal production mechanisms have been proposed. A selection of them will be explained in the following.

FIMPs

A first paradigm predicts a coupling with baryonic matter that is so weak that it precludes the possibility of reaching thermal equilibrium. Such candidates are called Feebly Interacting Massive Particles (FIMPs). The mechanism that produces the measured DM density is referred to as **freeze-in**. This mechanism expects the DM particles to originate from decays of baryonic matter or self-annihilation, until these processes become Boltzmann suppressed. Therefore, in contrast to the freeze-out mechanism, with this process the co-moving dark matter density increases in time until at freeze-in it becomes constant. Moreover, while for the freeze-out mechanism a large annihilation cross-section leads to a smaller constant abundance of DM, for the case of freeze-in, a stronger coupling to baryonic matter leads to a larger abundance. [24]

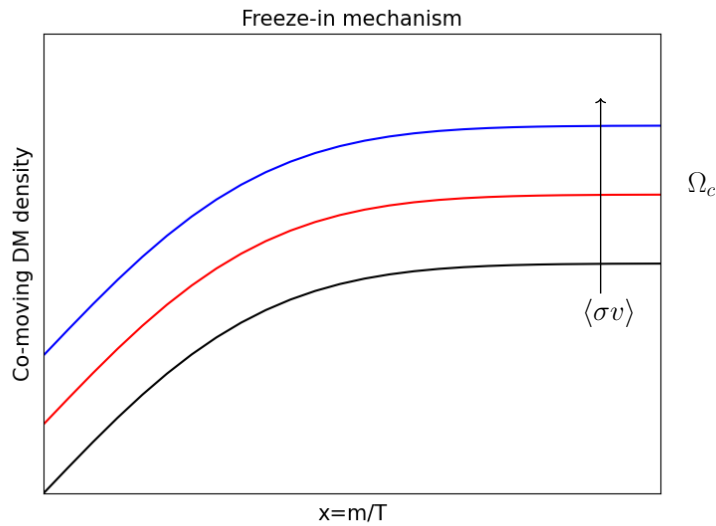


Figure 1.8: Co-moving number density for the freeze-in process. The density grows with time until after freeze-in it remains constant. The stronger the coupling to the SM is, the higher is the final relic density.

Sterile neutrinos

SM neutrinos are not considered as dark matter candidates, since they do not have the characteristics of being cold dark matter candidates. However, the hypothesized sterile neutrino, being significantly more massive, would be a CDM candidate in the mass range of keV-MeV [17]. This type of neutrino is a SM singlet fermion that has only mass-mixing with SM neutrinos. Its production mechanism can vary in different paradigms, but a popular one is predicted to be non-thermal, as the current DM density would arise from oscillations with SM neutrinos [25]. An interesting aspect of these

candidates is that they naturally arise from the see-saw mechanism [26] which can explain the small masses of SM neutrinos.

Axions

Similarly to the sterile neutrino, there exists another candidate that is connected to another theory beyond the SM: the Axion. This candidate naturally arises from the spontaneous breaking of the Peccei-Quinn symmetry, introduced to solve the Strong CP problem [27]. This particle, which arises from the QCD Lagrangian, couples to quarks, allowing for a mixing, for instance with pions. Such information is helpful in predicting the mass range of this particle, since it can be stated [28]:

$$m_A f_A = \frac{\sqrt{m_u m_d}}{m_u + m_d} m_\pi f_\pi \quad (1.23)$$

and with the given values of the SM this can be approximated to [29]:

$$m_A = 5.70(7) \mu eV \left(\frac{10^{12} GeV}{f_A} \right) \quad (1.24)$$

where f_A is the energy scale at which the Peccei-Quinn symmetry is broken. This energy scale is inversely proportional to the QCD coupling of the Axion. This means that the mass of the Axion is proportional to its coupling. Since strong QCD couplings would have become evident at collider experiments, Axions are predicted to have extremely small masses (depending on the exact model, they can cover the range from peV to meV). Such small masses can still coincide with CDM, because of their non-thermal production mechanism via the spontaneous symmetry breaking.

1.3.3 Summary

This section presented a selection of dark matter candidates. These selected paradigms are all based on the same assumption that DM particles interact with the SM particles with at least one force other than gravity. From the presented list, it is evident that there exist many candidates whose mass range extends below the range of the well known WIMP, motivating the search for sub-GeV DM. Furthermore, it is important to acknowledge the existence of non-particle solutions to the DM problem [30] [31]. However, this work focuses on searches for particle-like DM candidates and the way these candidates can be searched for will be explained in the next chapter.

Chapter 2

Dark Matter Detection

The experimental effort to probe the existence of particle dark matter candidates involves three distinct approaches. All of them rely on the assumption that DM interacts with baryonic matter at least via one more force other than the gravitational force. With this assumption, there exist three possible classes of Feynman diagrams to illustrate the interaction of dark matter with standard model particles (see figure 2.1). The first one describes the annihilation of DM particles into SM particles. This type of search is referred to as **indirect**, since only the annihilation and decay products interact with the experimental setup, and not the DM particles themselves. The annihilation process is expected to happen in the Milky Way, while the secondary particles, such as energetic gamma rays, can be detected with Earth-based or space-based telescopes. Experiments that perform these types of searches are e.g. the HESS [32] and MAGIC [33] Earth-based telescopes or the Fermi space telescope [34]. A second detection channel searches for the exact opposite process, the interaction of SM particles that produces DM particles. This method is referred to as **production** and can be probed at accelerator experiments. A signature for dark matter production is searched for in the form of missing transverse momentum in detectors such as ATLAS or CMS [35]. Finally, **direct** searches look for the signature of DM particles coming from the Milky Way and interacting with the SM particles in the experimental setup. Since the work presented in this thesis focuses on direct detection searches, only this detection channel will be considered in this chapter. Important aspects of the signal expected in this detection channel will be pointed out in the first section. The relevant sources of background will be briefly discussed directly after. In the final section, the current status of DM searches will be discussed.

2.1 Signal in Direct Detection

2.1.1 Dark Matter Halo Model

Before looking at the details of the actual signal signature in direct searches, the assumptions that are made regarding the distribution of DM particles in the surrounding of Earth-bound detectors need to be discussed. These assumptions result

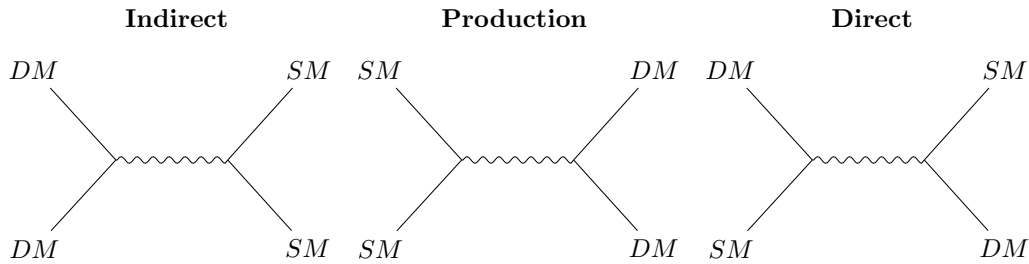


Figure 2.1: Classes of Feynman diagrams of possible interaction channels of dark matter with standard model particles. Time flows from left to right.

in the **standard halo model**.

As mentioned in section 1.2.1, the rotational curves of spiral galaxies suggest that DM is distributed as a spherical halo around the center of the galaxy. Assuming this to be isothermal, the velocity of the DM particles can be described with a Maxwell-Boltzmann distribution

$$f(v) = \frac{N}{\pi^{\frac{3}{2}} v_s^3} e^{-v^2/v_s^2} \quad (2.1)$$

where v is the velocity of the particles, $v_s = 220 \frac{km}{s}$ [36] is the velocity of the observational point in the solar system and N is a normalization factor. To calculate the expected rates of DM-nucleus interactions (see section 2.1.3) $f(v)$ has to be transformed into the frame of the Earth moving through the galaxy with the velocity $v_0 = 232 \frac{km}{s}$ [37]. This velocity distribution is usually cut off at $v_{esc} = 544 \frac{km}{s}$ [38] since particles faster than the escape velocity are not gravitationally bound to the galaxy. To estimate the flux of DM reaching Earth, another relevant factor is the density of DM in the solar system which is estimated to be $\rho_0 = 0.3 \frac{GeV}{c^2 cm^3}$ [39].

2.1.2 Expected Signal

The interaction between DM particles and the target material is assumed to be an elastic coherent scattering. Depending on whether the interaction happens with an electron or a nucleus, these scatterings generate either **electron recoils** (ER) or **nuclear recoils** (NR). While many experiments search for DM interactions in the form of electron recoils, this chapter will mainly concern nuclear recoils since the CRESST experiment (presented in the next chapter) focuses on this type of interaction.

The measurable quantity to detect elastic DM-nucleus scatterings is the energy transfer in the target after the collision. This can be calculated in the center-of-mass frame:

$$E_R = \frac{\mu^2 v^2}{m_N} (1 - \cos\theta_R) \quad (2.2)$$

where $\mu = \frac{m_1 m_2}{m_1 + m_2}$ is the reduced mass of the system DM particle and the target nucleus, v is their relative velocity, θ_R is the scattering angle and m_N is the nucleus mass [40].

This recoil energy is bound by the maximal case of $\theta_R=180^\circ$

$$E_R^{max} = \frac{\mu^2 v^2}{m_N} \quad (2.3)$$

The experimental result of a DM search is obtained by comparing the total measured spectrum of nuclear recoils to the one expected by DM particles of a specific mass and cross-section. How this expected spectrum can be calculated will be explained in the following section.

2.1.3 Differential Rate of Elastic scattering

The number of DM particles interacting in the detector setup depends on several factors. Firstly, it depends on the quantity of DM reaching Earth, in particular on the density of DM particles in the solar system ($n = \frac{\rho_0}{m_\chi}$) and their velocity (v). Secondly, this number also depends on parameters set by the experimental setup, such as the duration of the measurement (t) and the number of particles of the target material with which DM could interact (N_T). Finally, this number also depends on the cross-section of the interaction (σ) [40]. All in all, the number of expected interactions in a direct detection experiment is

$$N = t \frac{\rho_0}{m_\chi} N_T \int_{v_{min}}^{v_{esc}} v f(\vec{v}) \sigma(v, E_R) d\vec{v} \quad (2.4)$$

where v is the velocity of DM particles in the detector reference frame and v_{min} is the minimal velocity (of a DM particle) required to produce a nuclear recoil of energy E_R

$$v_{min} = \sqrt{\frac{m_N E_R}{2\mu^2}} \quad (2.5)$$

Direct detection experiments usually present their result in the form of a rate (R), i.e. the number of events per exposure

$$R = \frac{N}{exposure} = \frac{N}{t M_T} \quad (2.6)$$

where M_T is the total target mass, with the number of target particles

$$N_T = \frac{M_T}{m_N} \quad (2.7)$$

Using equation 2.4, the expected differential rate is given by

$$\frac{dR}{dE_R} = \frac{\rho_0}{m_\chi m_N} \int_{v_{min}}^{v_{esc}} v f(\vec{v}) \frac{d\sigma(v, E_R)}{dE_R} d\vec{v} \quad (2.8)$$

2.1.4 Scattering cross-section

Equation 2.8 shows how the differential rate depends on the differential cross-section of DM scattering off a nucleus. To calculate this cross-section, one has to consider the interaction at the quantum level, where DM particles are typically assumed to interact with quarks via a heavy mediator. The nature of this mediator, and so the type of the coupling, is not predetermined. In fact, one distinguishes two cases: the first includes vector or scalar mediators, and the second considers axial-vector mediators. Due to the dependencies of the final cross-section obtained in the two cases, these types of interactions have been dubbed **spin-independent (SI)** and **spin-dependent (SD)** interactions respectively [41].

Spin-Independent Case

For the spin-independent case, the differential cross-section is [42]:

$$\frac{d\sigma}{dE_R} = \frac{2m_N}{\pi v^2} \langle |\mathcal{M}|^2 \rangle \quad (2.9)$$

where m_N is the mass of the target nucleus, v is the relative velocity between the DM particle and the nucleus, and \mathcal{M} is the scattering amplitude of a DM-nucleus interaction. Since the De Broglie wavelength expected by DM particles reaching Earth exceeds the size of typically employed nuclei, DM particles are assumed to undergo a coherent scattering with the whole nucleus. The total scattering amplitude is therefore calculated as a sum of each individual DM-nucleon amplitude. To account for corrections needed by the substructure of the nucleus, a **nuclear form factor** is used. For the SI case, this factor describes the spatial distribution of the nucleons. For the total scattering amplitude, one can state:

$$\mathcal{M} \propto (Zf_p + (A - Z)f_n)F_{SI}(q) \quad (2.10)$$

where A is the atomic mass number (total number of nucleons) and Z the number of protons in a nucleus. The factors $f_{p/n}$ describe the probability of interaction of the DM particles with protons or neutrons and contain information about the strength of the coupling between DM and quarks. $F_{SI}(q)$ is the nuclear form factor.

There exist several models to estimate a form factor [43]. For SI interactions, the **Helm Form factor** parameterization is commonly used:

$$|F_{SI}(q)|^2 = \left(\frac{3j_1(qR_1)}{qR_1} \right)^2 \exp(-q^2s^2) \quad (2.11)$$

where j_1 is the spherical Bessel function. With equation 2.10, the spin-independent differential cross-section of a DM-nucleus scattering is:

$$\frac{d\sigma}{dE_R} = \frac{2m_N}{\pi v^2} (Zf_p + (A - Z)f_n)^2 |F_{SI}(q)|^2 \quad (2.12)$$

For typical spin-independent cross-sections, the mediator is assumed to be a scalar and the coupling of DM particles to proton and neutrons to be equal ($f_p=f_n$). Therefore,

$$\frac{d\sigma}{dE_R} = \frac{2m_N}{\pi v^2} A^2 f_n^2 |F_{SI}(q)|^2 \quad (2.13)$$

Due to this A^2 dependence, expected rates can be enhanced by employing heavy nuclei materials (see cross-section dependence of the rate in equation 2.8).

Spin-Dependent Case

For the case of an axial-vector interaction, the DM cross-section depends on the spin contributions of the nucleon [44]:

$$\frac{d\sigma}{dE_R} = \frac{16m_N}{\pi v^2} G_F^2 \frac{(J+1)}{J} |a_p \langle \mathbf{S}_p \rangle + a_n \langle \mathbf{S}_n \rangle|^2 |F_{SD}(q)|^2 \quad (2.14)$$

where G_F is the Fermi coupling, J is the nuclear angular momentum, $a_{p/n}$ is the effective coupling of the DM particle to the proton/neutron, and $\langle \mathbf{S}_{p/n} \rangle$ is the average spin contribution of the proton/neutron. From equation 2.14 it is evident that the SD contribution vanishes for nuclei where the nuclear ground state angular momentum is equal to zero ($J=0$). Since at first order corrections $J \neq 0$ is valid only for nuclei with unpaired nucleons, SD searches are usually performed with nuclei with an odd number of protons or neutrons.

The average spin contributions $\langle \mathbf{S}_{p/n} \rangle$ can maximally have the value 1/2. Their exact value depends on the nucleus configuration and can be estimated with various models. One of the first models that was developed is the *Independent Single Particle Shell Model*. This model estimates that the angular momentum can be entirely described by the contribution of the "odd" nucleon. However, this approximation can lead to overestimations of J . This fact was accounted for from other models, such as the *Odd Group Model* [45]. Here, J is corrected by a quenching factor that accounts for the fact that the spins of the "even" nucleons can be polarized by the "odd" nucleons. However, both models assume the effective interaction to be carried out by only the "odd" nucleon. This means that one of $\langle \mathbf{S}_p \rangle$ or $\langle \mathbf{S}_n \rangle$ has to be zero [46]. This fact is also not realistic for every nucleus. In fact, newer, more complex models abandon this assumption and consider also small (but non-vanishing) contributions of the "even" nucleons (see for example the *shell models* of Pacheco and Strottman [47]). Using these newest models, the even-numbered type of nucleons contribute to the total scattering amplitude. Nonetheless, their contribution is much smaller compared to the one originating from the "odd" nucleons.

SD contributions are commonly presented for the case of the DM particle coupling only to the proton or only to the neutron - usually referred to as **proton-only** or **neutron-only** interactions. The rates expected in these two cases depend on the combination of J and $\langle \mathbf{S}_{p/n} \rangle$ values. Since, for the SD case, the differential cross-section does not have an A^2 dependence, expected rates cannot be enhanced by employing heavy materials

as for the SI case. Higher rates are instead expected by nuclei with a high factor $X_{p/n}$ where

$$X_{p/n} = \frac{J+1}{J} \langle \mathbf{S}_{p/n} \rangle^2 \quad (2.15)$$

Nonetheless, it has to be noted that, except for a few cases with very light nuclei, higher rates are expected when probing the SI cases compared to the SD case, thanks to the additional A^2 dependence of the SI cross-section. This makes the sensitivity to SD interactions more challenging compared to the SI case.

2.1.5 Expected Recoil Spectrum

The differential rate as a function of the recoil energy is a quasi exponentially falling spectrum that extends up to the maximal recoil energy. As can be seen in equation 2.8, the differential rate depends on the mass of the DM particle (m_χ), the mass of the target nucleus (m_N) and the total cross-section of the interaction (σ).

The dependence on (m_χ) and (σ) is visualized in figure 2.2. The left plot shows the expected differential rate for three different m_χ values. With increasing m_χ , for a fixed target nucleus, the recoil energy range also increases due to the kinematics of the scattering process. This figure highlights the importance of low energy thresholds when searching for light DM masses, as only DM masses with an expected spectrum extending above threshold can be probed.

The right plot shows the expected differential rate for three values of σ . In contrast to the previous case, a variation in the nuclear recoil cross-section does not affect the kinematics of the scattering. Therefore, increasing the cross-section does not influence the shape of the spectrum but scales the expected rate linearly.

Similarly to the case of the DM mass, the mass of the target nucleus also influences the spectral shape due to kinematics: lighter target nuclei lead to higher end points of the expected recoil spectra. This is visualized in figure 2.3. Figures 2.2 and 2.3 were produced with SI cross-sections but the described qualitative behavior of the differential rate is valid also for SD cross-sections.

2.2 Background in Direct Detection

Every particle interaction (other than DM) that can be detected in the experimental setup represents a source of background for DM direct detection. In this section, the main sources of background will be presented.

2.2.1 Neutrons and Neutrinos

Neutrons and neutrinos are the sources of background which are most similar to DM particles because of their neutral charge. These two particles could mock a dark matter signal in the detector without providing a simple tagging method, as they would induce a nuclear recoil. The neutrino flux is not reduced by the rock overburden. Therefore, neutrinos are an irreducible source of background for direct detection experiments.

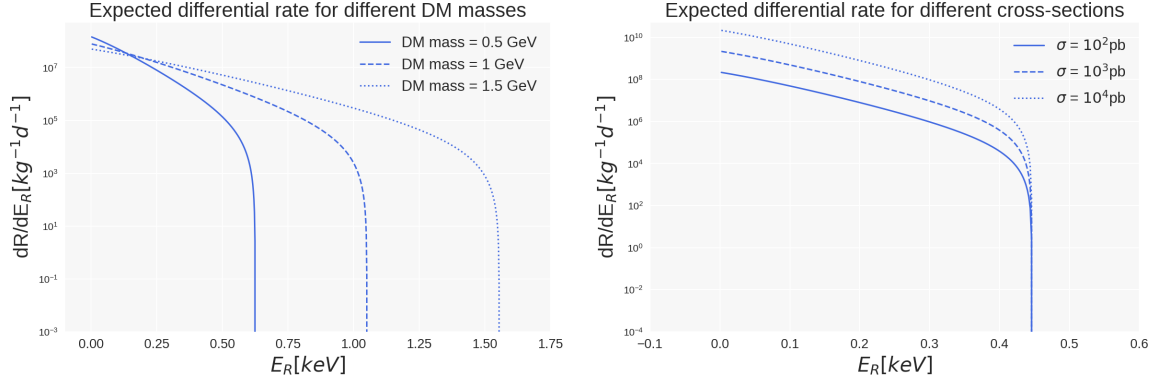


Figure 2.2: Expected differential nuclear recoil energy spectra for the SI case with varying m_χ and σ_{SI} . Both plots represent the expected rate for the same exposure and a ${}^7\text{Li}$ target. On the left $\sigma_{SI} = 10^2 \text{pb}$ and m_χ is $0.5 \frac{\text{GeV}}{c^2}$ (straight), $1 \frac{\text{GeV}}{c^2}$ (dashed) or $1.5 \frac{\text{GeV}}{c^2}$ (dotted). On the right $m_\chi = 1 \frac{\text{GeV}}{c^2}$ and σ_{SI} is 10^2pb (straight), 10^3pb (dashed) or 10^4pb (dotted).

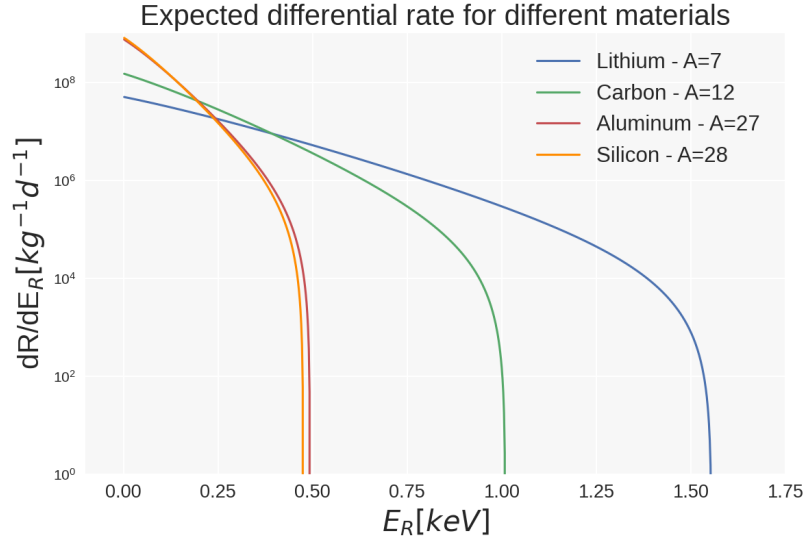


Figure 2.3: Expected differential nuclear recoil energy spectra on different nuclei. For each nucleus, the expected rate is calculated for $m_\chi = 1 \frac{\text{GeV}}{c^2}$, $\sigma_{SI} = 10^2 \text{pb}$.

On the other hand, the background caused by neutrons can be reduced by employing materials that moderate their energy, lowering it below the experimental threshold.

2.2.2 Muons

The Earth's surface is strongly irradiated by cosmic rays. These rays travel in space mainly in the form of protons. Once they reach the Earth's atmosphere, they can

interact producing mainly pions and kaons. These particles then decay into neutrinos and muons. The latter represents an indirect source of background for direct detection experiments, as they can generate secondary neutrons interacting with the material of the experimental setup. Therefore, direct detection experiments are typically located in underground laboratories where the muon flux is strongly reduced by a rock overburden.

2.2.3 Gammas, Electrons, Alphas

Further particles that are a potential source of background are electrons, gammas, and alpha particles. If these particles reach the detectors, they can interact in the detector inducing electron recoils. Typically, these electron recoils can be distinguished from nuclear recoils with an active background discrimination method.

2.2.4 New Backgrounds

In the last decade, direct detection experiments have made enormous improvements in sensitivity, detecting smaller energies and probing smaller interaction cross-sections. Crossing these new frontiers, it is not unexpected to encounter unknown backgrounds. For instance, the sensitivity of sub-GeV dark matter searches at the time of writing is highly suppressed by the presence of an unknown low-energy background. The precise range of this unknown background varies in different experiments. Typically, in CRESST this background shows a rise that starts around 0.2keV and grows exponentially towards the energy threshold of the detector. Figure 2.4 shows this unexpected rise of events as seen from different experiments. Due to the low-energy nature of this excess, this background has been dubbed *Low Energy Excess* (LEE). CRESST has been the first experiment to detect LEE in 2019 down to an energy threshold of 30.1 eV [48]. After CRESST, many experiments started to observe a rise of events at low energies. The community of direct detection experiments is currently studying this effect since the identification or removal of this excess is crucial to improve the sensitivity. A review of the current observations and hypotheses about the origin of the LEE can be found in [49].

2.3 Current Status of Dark Matter Searches

In the absence of a DM signal, direct detection experiments present their sensitivity in terms of the area of the σ - m_χ parameter space that they can exclude with a certain confidence level. These exclusion limits are usually presented either for a spin-independent or a spin-dependent DM-nucleon coupling.

2.3.1 Spin-Independent Searches

The current exclusion limits for the SI case can be seen in figure 2.5. It can be noticed that some experiments are highly sensitive to high dark matter masses (above 1 GeV/ c^2), where cross-sections down to $10^{-46}cm^2$ can be excluded. Such

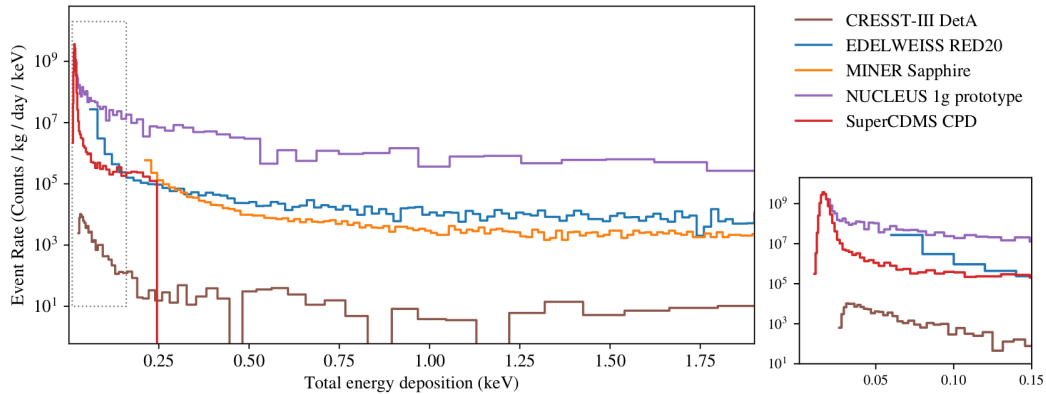


Figure 2.4: The energy spectrum of different experiments containing the LEE. Figure reproduced from [49].

experiments use large Time Projection Chambers (TPCs) filled with noble gas liquids (e.g. Darkside [50], LUX (now LZ) [51], Xenon [52] etc.). With their high exposures, these experiments have been very successful in covering the parameter space above 1 GeV/c^2 , getting close to the so-called *neutrino floor* [53] (shaded gray area), the region in which the first neutrino-nucleus interactions are expected. Other direct detection experiments complement the experimental effort of TPC experiments, covering the sub-GeV parameter space. These are mainly cryogenic experiments (such as CRESST, EDELWEISS [54], or SuperCDMS [55]), which can reach significantly lower thresholds compared to TPC experiments. In this overview plot, the CRESST experiment provides the strongest sensitivity for DM masses in the range 0.16-1.8 GeV/c^2 [17] under standard assumptions.¹

2.3.2 Spin-Dependent Searches

The probed parameter space for the proton-only and neutron-only SD interactions are seen in figure 2.6 for measurements performed before the one that will be presented in this work (chapter 5). Some commonly used nuclei that are highly sensitive to neutron-only interactions are ^{17}O , used by CRESST, ^{73}Ge , used by EDELWEISS [58] and CDMSLite [59], or ^{129}Xe and ^{131}Xe , used by Xenon-filled TPC experiments such as XENON1t [60], LUX(now LZ) [61] and PandaX [62]. Some examples of nuclei highly sensitive to proton-only interactions are ^1H , used by Collar [63], ^7Li by CRESST [64] or ^{19}F by PICO [65].

¹A higher sensitivity is achieved by the XENON1t experiment if they interpret their results under the assumption of the Migdal effect (XENON1T(M) [56]). This effect can be exploited to extend the sensitivity of experiments [57]. However, the existence of this effect has not been experimentally proven yet.

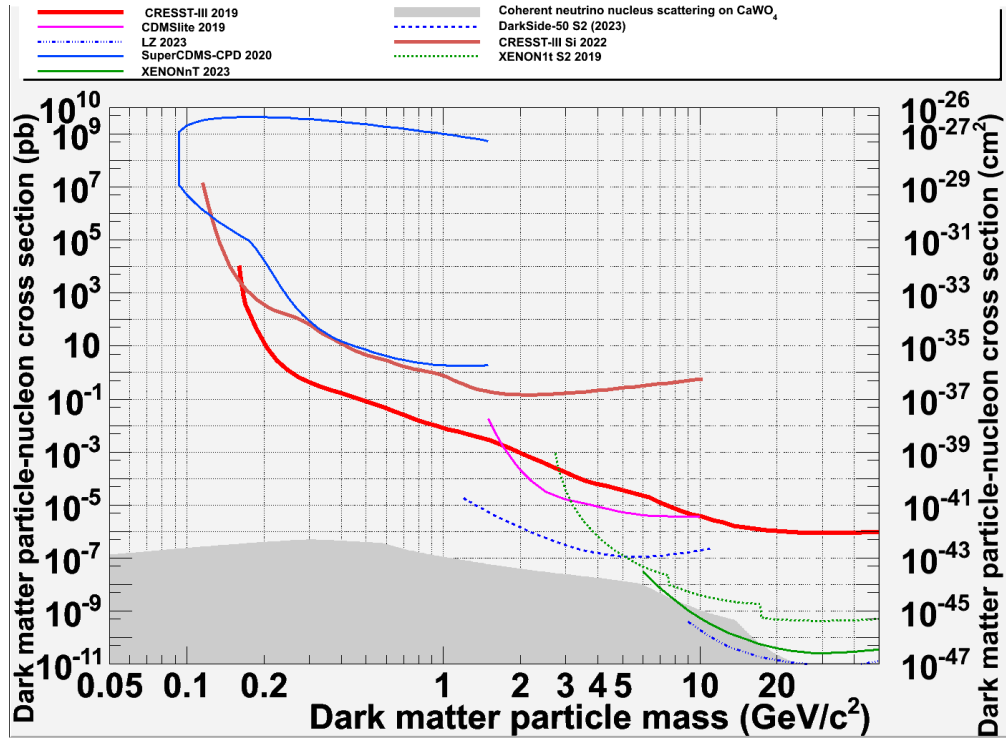


Figure 2.5: Current status of direct detection experiments for SI DM-nucleon coupling. The shaded gray area represents the neutrino floor for the example of scatterings on a CaWO_4 target.

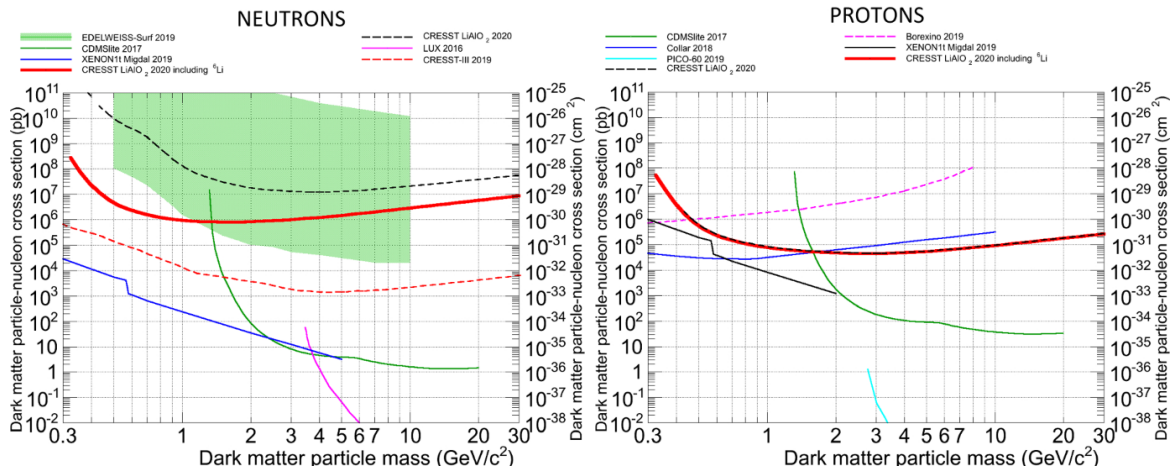


Figure 2.6: Current status of upper limit on elastic scattering SD DM-nucleon cross-section for the neutron-only (left) and proton-only (right) case at 90% CL. The red dashed line shows the exclusion limits obtained with a lithium aluminate crystal. Figure reproduced from [66].

Chapter 3

The CRESST Experiment

CRESST (Cryogenic Rare Event Search with Super Conducting Thermometers) is a dark matter direct detection experiment located in the underground laboratory *Laboratori Nazionali del Gran Sasso* (LNGS), in Italy. Its objective is to detect the elastic scattering of a potential DM particle with the nuclei in the target material. In the case of CRESST, the target material is a crystal operated as a calorimeter at cryogenic temperatures $\mathcal{O}(\text{mK})$. The DM interaction induces a nuclear recoil, whose energy deposit is measured as a temperature increase in the temperature sensor of the calorimeter.

In this chapter, an overview of this experiment will be given. The initial focus of this chapter will be on the signal formation and read-out. For this purpose, the principle of a cryogenic calorimeter and of a Transition Edge Sensor (TES) will be explained. Furthermore, the CRESST facility at LNGS will be described, including a description of the detector modules and their operation. In conclusion, the latest data-taking period will be shortly introduced.

3.1 Principle of Signal Read-out

3.1.1 Cryogenic Calorimeters

The interaction sought by the CRESST experiment is a dark matter particle scattering off an atomic nucleus within the target crystal. The kinetic energy, which is transferred to the nucleus during this interaction, is deposited into the crystal lattice in the form of phonons. A very precise measurement of this energy deposit is provided by cryogenic calorimeters which read out this phonon signal in the form of a temperature rise. Their basic components are a crystal in which an energy ΔE is deposited, a device to measure the temperature variation ΔT , and a thermal bath with which the system is in thermal equilibrium before and after a particle interaction. In a simplified ideal calorimeter, the energy deposit corresponds to a temperature increase given by:

$$\Delta T = \frac{\Delta E}{C} \tag{3.1}$$

with C being the heat capacity of the calorimeter absorber.

The measurement of this temperature variation with a cryogenic calorimeter offers two advantages. Firstly, the reconstruction of the energy deposit is very precise, thanks to the **low thermal noise** present at cryogenic temperatures ($\mathcal{O}(\text{mK})$). Secondly, such low temperatures lead to extremely low heat capacities (e.g. for dielectric materials $C \sim T^3$) which generate a **large temperature signal** for a given energy deposition. To measure such temperature variation, CRESST adopts a Transition Edge Sensor (TES).

3.1.2 The Transition Edge Sensor

The Transition Edge Sensor (TES) used by CRESST is a superconducting tungsten film deposited on the target material and operated at the transition temperature (for tungsten around 15 mK), where the resistance is a step function of the temperature of the sensor. A schematic representation of a transition can be seen in figure 3.1. Thanks to the steepness of the transition curve, a small variation in temperature ($\mathcal{O}(\mu\text{K})$) causes a significant change in the resistance ($\mathcal{O}(m\Omega)$), providing a measurable electric signal.

The resistance-temperature relation is non-linear at temperatures close to the super- and normal-conducting phase. Therefore, the operating point is typically chosen in the linear part of the transition. To allow for a precise adjustment of the operating point, the TES is equipped with a resistive heater, composed of a gold film on which a current can be applied.

An accurate model for the signal formation has been published in [67] and will be briefly summarized next.

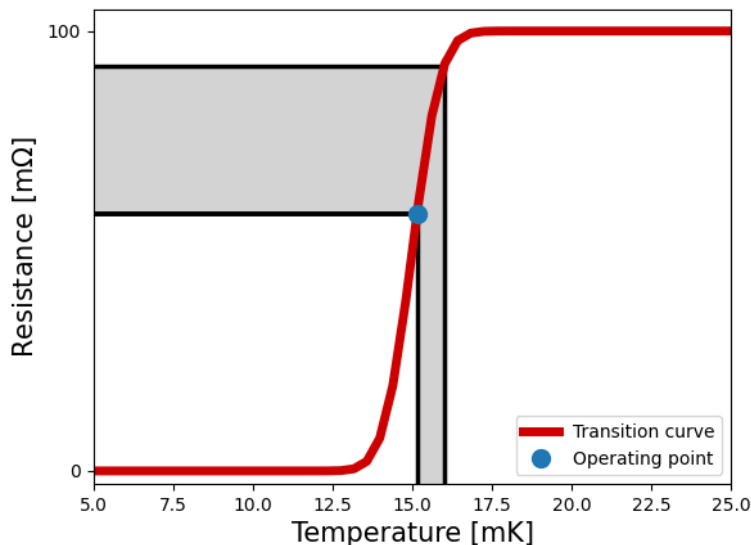


Figure 3.1: Schematic representation of the temperature dependence of the TES's resistance.

3.1.3 Thermal Model

To model the signal of a cryogenic calorimeter, it is useful to separate the calorimeter into three parts: the absorber crystal, the thermal bath, and the TES. The latter can be subdivided further into an electron and a phonon system. An illustration of the thermal sub-components of a calorimeter can be seen in figure 3.2, where the main components are depicted and labeled with their heat capacities C and temperatures T . The thermal connections of these subsystems are indicated by links with conductance G .

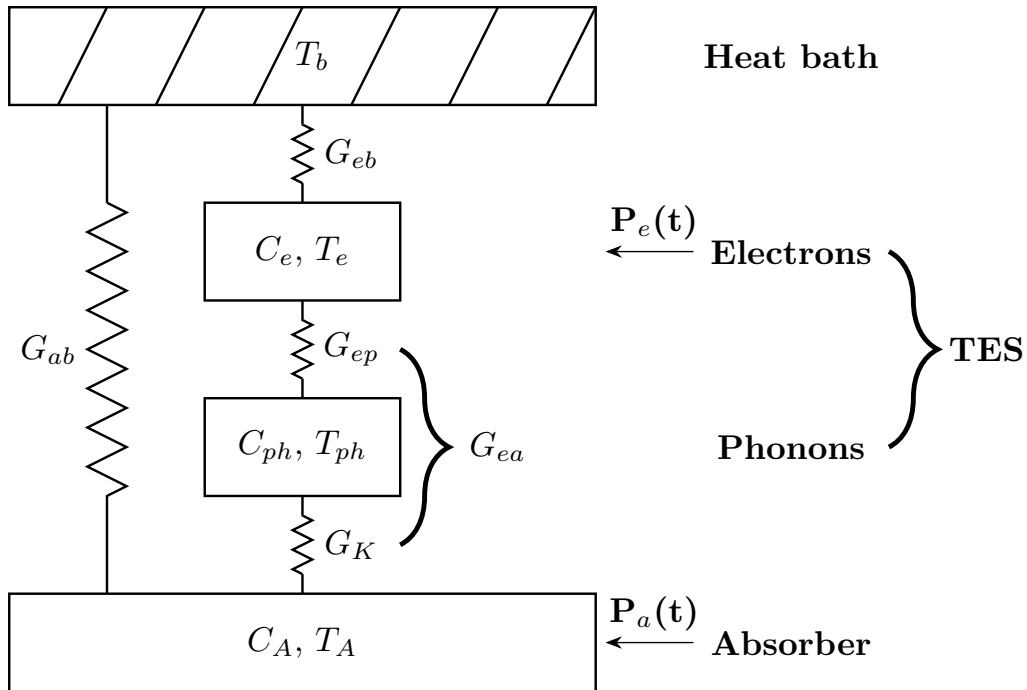


Figure 3.2: Sketch of the three parts of a calorimeter: the crystal, the TES, and the thermal bath. The TES itself is divided into a phonon and an electron part.

Thermal Couplings

To restore the thermal equilibrium after a temperature rise, the thermometer is thermally coupled to the heat bath. This link is created by a gold stripe overlapping with the tungsten film on one end, and connected to the heat bath via a gold bond-wire ($G_{Au} \sim T$) on the other end. This coupling is represented as the link of the electron subsystem of the thermometer to the bath, G_{eb} . Furthermore, the thermometer is thermally coupled to the absorber. Since the heat capacity of the TES phonon subsystem is negligibly small at the operation temperatures ($\mathcal{O}(\text{mK})$), the relevant conductances, namely G_{ep} , which links the two subsystems of the TES ($G_{ep} \sim T^5$), and G_K , which represents the Kapitza boundary conductance of thermal phonons between the absorber and the tungsten film ($G_K \sim T^3$), can be simply assumed to be in series,

and the effective link between the TES electron system and the absorber is given by

$$G_{ea} = \left(\frac{1}{G_{ep}} + \frac{1}{G_K} \right)^{-1} \quad (3.2)$$

Finally, the absorber is also unavoidably thermally coupled to the heat bath due to the mechanical mounting of the crystal in the holding structure. The design of the detector holder aims at minimizing this parasitic link, which reduces the signal in the thermometer.

Phonon Propagation

Once a particle interaction occurs in the absorber, a population of optical phonons is created in the time scale of ~ 10 ps. Around 100 ps after the particle interactions, such phonons have decayed into acoustical phonons with a frequency of half the Debye frequency $\frac{\nu_D}{2}$, defined as

$$\frac{\nu_D}{2} = \frac{k_B \Theta_D}{2h} \quad (3.3)$$

where k_B is the Boltzmann constant, Θ_D is the Debye temperature and h is the Planck constant. Their total energy depends on Θ_D of the target material. To understand the order of magnitude of such energies, one can look at the example of CaWO_4 (a crystal commonly used in CRESST). Its Debye temperature is 250 K [68] and therefore the energy can be estimated as

$$\begin{aligned} E &= k_B \Theta_D \approx 8.6 \times 10^{-5} \frac{\text{eV}}{\text{K}} \cdot 250 \text{K} \\ &\approx 10 \text{meV} \end{aligned} \quad (3.4)$$

while the thermal energies at the operating temperatures are

$$\begin{aligned} E &= k_B T \approx 8.6 \times 10^{-5} \frac{\text{eV}}{\text{K}} \cdot 10 \text{mK} \\ &\approx 1 \mu\text{eV} \end{aligned} \quad (3.5)$$

Since these phonons have energies much higher than the thermal energies, they can be regarded as non-thermal. These non-thermal phonons are in equilibrium and start to down convert towards a thermal distribution, with a very rapid initial decrease of the average phonon energy, followed by a much slower rate of change. As a consequence, the average phonon frequency stays quasi-constant for a few milliseconds, and during this time these phonons spread over the entire absorber. The fraction of the phonons that enter the thermometer interact with its electron system, which as a consequence experiences a time dependent power input $P_e(t)$. The phonons that thermalize directly in the absorber are modeled by a power input directly into its phonon population $P_a(t)$.

Thermal signal

To describe the thermometer response, two components have to be considered: the power input into the electron system and the one in the absorber. Defining ϵ as the fraction of phonons thermalizing in the thermometer and $(1-\epsilon)$ the one thermalizing in the crystal, one can describe these two power inputs as:

$$P_e(t) = \Theta(t)P_0e^{-t/\tau_n} \quad (3.6)$$

$$P_a(t) = \frac{1-\epsilon}{\epsilon}P_e(t) \quad (3.7)$$

where the step function $\Theta(t)$ represents the assumption that a uniform density of non-thermal phonons is immediately present after the particle interaction and P_0 is the initial power input in the TES

$$P_0 = \epsilon \frac{\Delta E}{\tau_n} \quad (3.8)$$

with ΔE being the energy deposited by an incoming particle and τ_n the thermalization time of the initial non-thermal phonons, which is determined by the two competing phenomena of thermalization in the absorber crystal and in the thermometer foil:

$$\tau_n = \left(\frac{1}{\tau_{film}} + \frac{1}{\tau_{crystal}} \right)^{-1}$$

Here τ_{film} and $\tau_{crystal}$ are the time constants for the thermalization in the thermometer film and in the crystal, respectively. With these constants, one can describe the fraction of phonons thermalizing in the TES as

$$\epsilon = \frac{\tau_{film}^{-1}}{\tau_{film}^{-1} + \tau_{crystal}^{-1}} \quad (3.9)$$

$$= \frac{\tau_n}{\tau_{film}} = \frac{\tau_{crystal}}{\tau_{crystal} + \tau_{film}} \quad (3.10)$$

The power inputs in the absorber and in the crystal can be described by two coupled differential equations that depend on the heat links shown in figure 3.2.

$$P_e(t) = C_e \cdot \frac{T_e}{dt} + (T_e - T_a) \cdot G_{ea} + (T_e - T_b) \cdot G_{eb} \quad (3.11)$$

$$P_a(t) = C_e \cdot \frac{T_a}{dt} + (T_a - T_e) \cdot G_{ea} + (T_a - T_b) \cdot G_{ab} \quad (3.12)$$

With the initial conditions $T_a(0) = T_e(0) = T_b$, the solution for the signal as temperature variation is :

$$\Delta T_e = \Theta(t) \cdot \left[\underbrace{A_n(e^{-t/\tau_n} - e^{-t/\tau_{in}})}_{\text{non-thermal}} + \underbrace{A_t(e^{-t/\tau_t} - e^{-t/\tau_n})}_{\text{thermal}} \right] \quad (3.13)$$

This solution can be separated into two parts, a non-thermal component with the amplitude A_n and a thermal component with the amplitude A_t . The non-thermal

component is a fast component that is given by the power input $P_e(t)$ (phonons that reach the TES when still non-thermal), while the thermal component is a slow component that is given by the power input $P_a(t)$. τ_t is the intrinsic thermal relaxation time of the absorber, while τ_{in} describes the intrinsic thermalization constant of the thermometer, which depends on its link to the heat bath.

Regime of Operation

The relation between τ_{in} and τ_n determines the operating regime of the detector. When the thermalization time of the thermometer is much faster than the total thermalization time of the initial phonon population, i.e. when $\tau_{in} \ll \tau_n$, the detector measures the flux of the incoming phonons and it is said to be operated in **bolometric mode**.

For $\tau_{in} \gg \tau_n$ the detector integrates the power input, and therefore it is said to be operated in **calorimetric mode**. In this case the amplitude of the signal non-thermal component is proportional to the energy deposition in the crystal:

$$A_n \propto -\epsilon \frac{\Delta E}{C_e} \quad (3.14)$$

Depending on the mode in which the detector is working, the thermal and non-thermal components have the same (calorimeter) or a different (bolometer) rise time. An example of the pulse shape of each mode can be seen in figure 3.3.

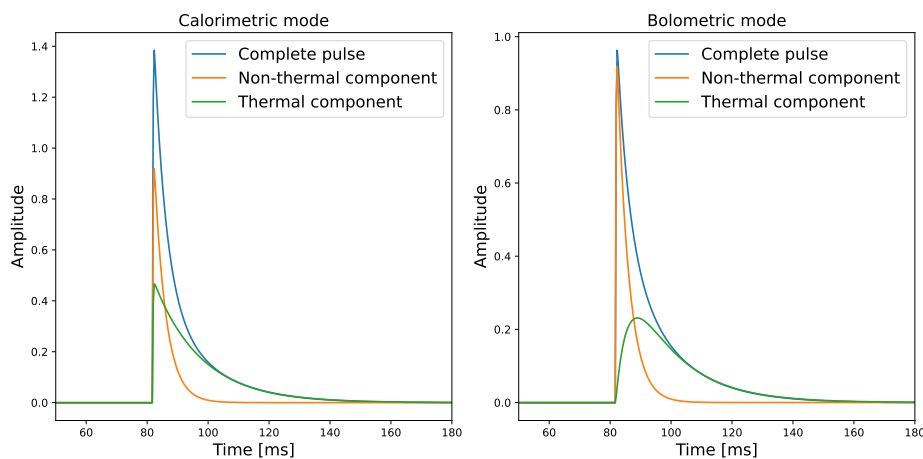


Figure 3.3: Example of a pulse of a detector working in the calorimetric mode (left) and one working in the bolometric mode (right).

3.1.4 Maximization of the Signal

In a calorimeter, the sizes of the crystal and the thermal sensor are tuned aiming at a ΔT_e description with a dominant non-thermal component. By looking at equation 3.14 this could be achieved with a higher ϵ . For a higher ϵ , a smaller τ_{film} is needed, assuming $\tau_{crystal}$ to be constant for a given crystal choice. This could possibly be

achieved by increasing the TES, given that:

$$\tau_{film} \propto \frac{V_{crystal}}{A_{TES}} \quad (3.15)$$

However, this would increase also the heat capacity of the electron system significantly, and therefore reduce the signal.

A possible approach to enlarge the area of the TES while keeping its heat capacity constant is to apply phonon collectors, additional metal films which reach the superconducting phase at higher temperatures compared to tungsten, e.g. aluminum ($T_C = 1.2$ K). Since at temperatures far below T_C the heat capacity of a material behaves as

$$C \propto e^{-\frac{1}{T}} \quad (3.16)$$

the contribution of aluminum to the total heat capacity of the thermometer is negligible at the temperature of the tungsten transition. An illustration of a TES with the phonon collectors, as well as the thermal link can be seen in figure 3.4.

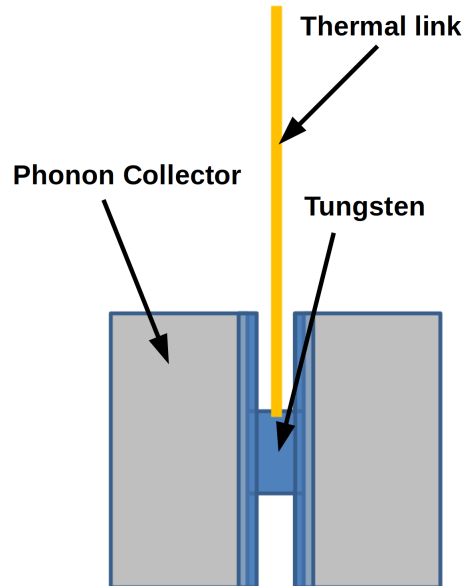


Figure 3.4: Illustration of the design of a TES with phonon collectors and thermal link.

3.2 The CRESST Facility

The cryogenic calorimeters described above require a cryostat to reach temperatures in the order of mK and an electric circuit to read out the TES resistance. Moreover, as mentioned in section 2.2, a good background reduction and discrimination are crucial for the detection of a dark matter interaction with the target material. This section will present all the elements that compose the CRESST experimental setup and its strategy to discriminate backgrounds.

3.2.1 Backgrounds at LNGS

The LNGS laboratory is a facility dedicated mostly to rare event experiments. The necessary low background environment is provided by a rock overburden of 1400 m (3800 m water equivalent), which acts as an efficient shielding against cosmic radiation. Nonetheless, some background particles are not stopped by the rock and reach the CRESST facility. In addition to that, the rock itself and the materials employed for the experimental setup can represent a source of background. In the following, such backgrounds will be shortly discussed.

Muons

Most of the products of cosmic rays are strongly reduced by the Gran Sasso mountain and don't reach the underground laboratory. Muons, however, though strongly attenuated, are still present inside the laboratory with a flux of $3.41 \times 10^{-4} m^{-2} s^{-1}$ [69]. These muons could generate secondary particles that can enter the region of interest (ROI) of CRESST.

Radionuclides

The mountain contains radioactive elements, such as Uranium and Thorium. In their decay chain, among others, Radon is produced. This element is a particularly dangerous background source, as its gaseous state enables it to diffuse through the mountain and reach the experimental setups.

3.2.2 Cryostat and Shielding

To shield the detectors from the backgrounds described in the previous section, a system of several layers, each designed for a specific type of background, surrounds the detectors. A schematic representation of the complete experimental setup of CRESST can be seen in figure 3.5.

The outer layer is composed of 40 cm of polyethylene. This material reduces the energy of neutrons, suppressing their detection in the detectors. This layer is followed by plastic scintillators, equipped with photo-multipliers which measure the light emitted by the interaction of highly energetic charged particles. This layer therefore acts as a muon veto panel. Afterward, there is an airtight box flushed with nitrogen. This is called the *radon box* because it is designed to prevent this element from entering the experimental setup. Inside the radon box, a 20 cm thick layer of lead covers the inner part of the experiment. Gamma particles are shielded by this layer due to the substantial density of lead. However, there are also some radioactive isotopes of lead (e.g. ^{210}Pb) that become an additional form of background. Therefore, the innermost shielding is composed of 14 cm of only high-pure copper to stop this additional radiation. Inside the cryostat, there is an additional polyethylene shield that stops neutrons generated by muons in the lead shield.

The detector modules are connected to a cryostat, a wet dilution refrigerator from Oxford Instruments (Kelvinox 1000), which can reach a base temperature of 6 mK. The modules are connected to the coldest point of the cryostat via a copper connection

(*cold finger*). The displacement of the detectors from the coldest point of the setup is needed to ensure that the detectors are well shielded from the non-radiopure commercial refrigerator.

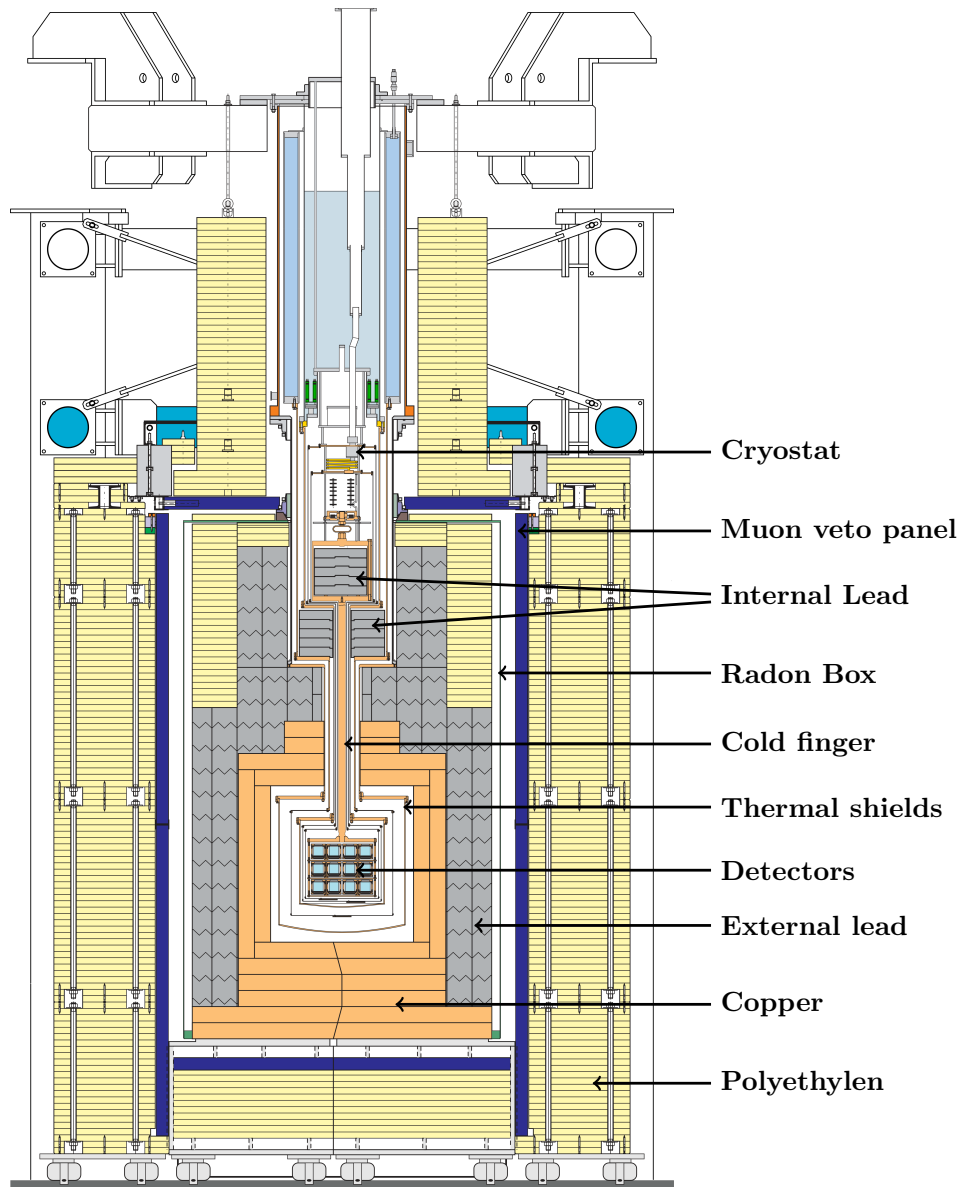


Figure 3.5: Sketch of the setup of the CRESST experiment.

3.2.3 CRESST-III Detector Modules

The rock overburden and the additional shielding layers are very powerful background reduction methods. However, some background particles still make their way into the detector modules. In addition to that, the absorber crystal itself can also contain intrinsic background e.g. due to crystal impurities. Therefore, to actively discriminate

background events from the sought-for signal, CRESST developed an event-by-event discrimination method based on the simultaneous measurement of two signals.

The Phonon-Light Technique

When employing scintillating crystals as absorbers for the cryogenic calorimeters, an energy deposition in the crystal induces both phonons and the emission of scintillation photons. The simultaneous read-out of both heat and scintillation light signals allows for an event-by-event discrimination that relies on lower light emitted by nuclear recoils, which result from DM or neutrons interactions, with respect to electron recoils, resulting from α , β , γ interactions. To quantify the emitted light, one can define the *light yield* (LY), as:

$$LY = \frac{\text{energy of light signal}}{\text{energy of phonon signal}} \quad (3.17)$$

To visualize the different LY generated by various interaction types, the LY can be plotted against the phonon energy. An illustration of this plot for the example of a CaWO_4 absorber is presented in figure 3.6. A LY of 1 at the energy of the calibration peak is assigned for events originating from electron and gamma particles. Compared to it, the light signal generated by nuclear recoils is quenched. The light yield that is expected by the different interactions is known from dedicated calibration campaigns. More details about how the LY plot is used to discriminate events will follow in section 4.3.

To measure the light emitted by scintillating absorbers, CRESST adopts the same technology employed for the phonon channel, namely an additional cryogenic detector optimized for the detection of scintillation light positioned close to the main absorber.

Module design

The combination of the scintillating crystal (main absorber) and the light detector is referred to as a *module*. After the CRESST-II phase, where thresholds of 300-400 eV were reached, some major modifications were applied to the CRESST-III modules with the aim of achieving thresholds below 100 eV. To meet this goal, the target crystals were scaled down to around 20 g (see [70] for more details on the choice of the target size). Regarding the target materials, there exist many that can be used as cryogenic calorimeters. CRESST commonly uses those which are also scintillating materials to enable the employment of the phonon-light technique. The most used material is CaWO_4 , but other ones will be presented at the end of this chapter. The light detector is composed of a thin wafer made of silicon-on-sapphire. This shape has been chosen to maximize the covered area and simultaneously ensure a low energy threshold thanks to the lower mass (for the relation between mass and threshold see for example [71]). Both the crystal and the light detector are equipped with a TES. To maximize the collection of the scintillation light on veto events originating from the surfaces facing the main absorber, the inner part of the holder structure is covered with a scintillating and reflective foil.

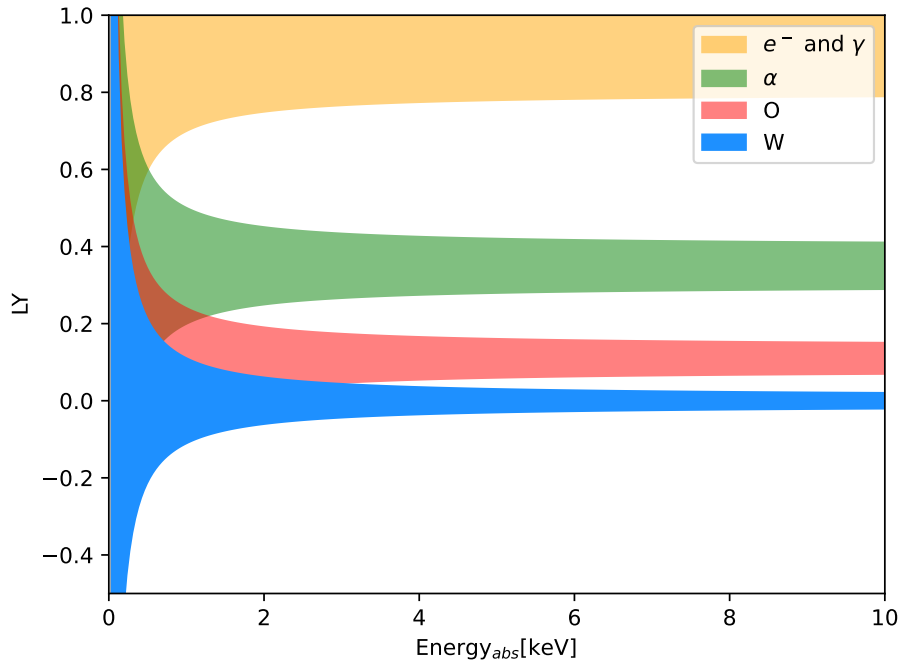


Figure 3.6: Illustration of the light yield plot for the case of CaWO_4 . The different bands separate electron recoils caused by electrons and gammas (yellow), alpha particles (green), and nuclear recoils on oxygen (red) or tungsten (blue) nuclei.

3.2.4 Resistance Read-out

Read-out circuit

As previously described, a temperature variation in the TES of the order of μK translates into a variation of its resistance in the order of $\text{m}\Omega$. To measure such a small variation, CRESST uses a read-out circuit based on SQUIDs (Superconducting QUantum Interference Devices). The read-out circuit containing the SQUIDs can be seen in figure 3.7.

Here, the TES and a shunt resistor (R_S) are placed in parallel. A DC bias current (I_B) splits between the TES (I_T) and the shunt resistor (I_S). A variation in the resistance of the TES causes a change of the branching in the circuit. The shunt resistor branch is positioned in series with the input coil of a SQUID. Variations in the (I_S) current cause a change of the magnetic flux coupled to the SQUID.

SQUID operation

The variations in the induced magnetic field are converted into a voltage signal by the SQUIDs. The SQUID provides an output voltage that is periodic in the applied magnetic flux with the period of one flux quanta ϕ_0 . To overcome the ambiguity due to this periodicity, the SQUIDs in CRESST are operated in flux locked loop, with an additional feedback coil (also depicted in figure 3.7) used to keep the flux through the SQUID loop constant. Therefore, for energy depositions the final output is a pulse

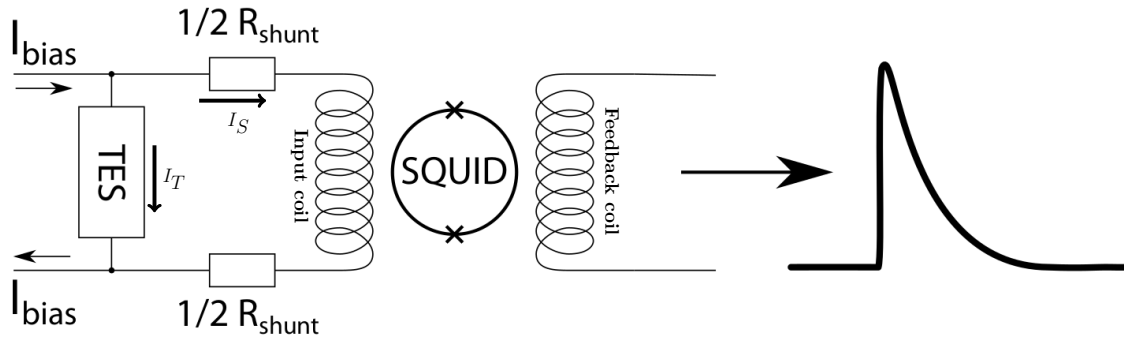


Figure 3.7: Schematic representation of the read-out circuit. Figure modified from [72].

with a fast voltage jump, followed by a longer decay that represents the return to the thermal equilibrium (also visible in figure 3.7). In some cases, the current variation is too fast for the feedback loop to follow, e.g. in cases of a very energetic particle interaction. This leads to a change of the baseline to a different value. This jump to a different baseline is referred to as *flux quantum loss*. The electronics can go through a limited set of baseline offsets. Once the lowest is reached, it returns to the one closest to zero, resulting in what is called a *SQUID reset*. The effect of a flux quantum loss and a SQUID reset on the data will be shown in section 4.2.1.

3.2.5 Temperature Control

Detector optimization

As already described in section 3.1.2, the TES suffers from a limited dynamic range. In choosing the optimal operating temperature, it has to be taken into account that the resistance-temperature relation at transition (i.e. the transition curve) varies with the strength of the bias current due to self heating effects. A careful choice of the bias current is therefore needed.

The choice of current is driven by the need to maximize the signal-to-noise ratio, without inducing excessive self-heating. Once the optimal bias current is found, the temperature can be controlled further with the current sent to the heater and the optimal operating point can be set, as depicted in figure 3.1.

Stabilization of the operating point

To monitor the stability of the TES temperature (operating point), artificial pulses of a fixed height are sent through the heater throughout a complete measurement. The response of the TES to these heat pulses is then monitored over time. These control pulses (CPs) are chosen to be large enough to bring the TES into the normal conducting phase. Therefore, the TES response results in a saturated pulse (shows a plateau at the tip). If the operating point is drifting, the height of the CP plateau will

vary. To maintain a stable temperature, an automated control loop is set up to adjust the heater current, keeping the pulse height of the CP constant over time.

Monitoring of the detector response

In addition to the CP, also so-called Test Pulses (TP) are sent to monitor the detector response over time. These pulses, unlike the CPs, are sent in different heights repeatedly over time. The goal is to get a value for the detector response, from low energies up to high energies, needed to interpolate the energy calibration throughout the measurement. In addition to this, despite the previously described control system, small fluctuations can still appear. TPs help also to monitor and compensate for these fluctuations over time. How these pulses can be used during analysis will be described in section 4.2.2.

3.2.6 Data Acquisition

Hardware Triggered Data

The voltage signal of the SQUIDS is digitized with a chosen sample frequency and written to disk. One option to store these data is to apply an online-triggering method and save only the parts of the stream that follow a sample exceeding a chosen threshold. This value should be high enough to avoid noise triggers, but low enough to reconstruct the smallest possible energies. In older CRESST runs this was the only adopted data acquisition type. Nowadays, hardware triggered data is used only for data quality monitoring and fast analysis.

Stream Data

For a dark matter analysis, an offline triggering method is more advantageous. For this purpose the complete stream of data is stored to disk. To perform a continuous sampling of the data stream, the output is split into two digitizers which are operated in alternate mode, i.e. when one is sampling, the other is being read out. A more in depth description of the continuous data taking can be found in [73]. Saving the complete stream allows for the application of a software trigger that leads to lower energy thresholds. This is possible because a filter that maximizes the signal to noise ratio can be employed for triggering (more details will follow in section 4.1.1).

Muon Veto

Apart from the data recorded by the detectors, there is also data collected from the muon panels. In this set of data, the timestamps of events occurring in the muon panels are written. These timestamps are then used during analysis to apply a muon veto cut. See section 4.2.1 for more details.

3.3 Latest Run - Run36

Run 36 is the fourth data-taking period of the third phase of CRESST (CRESST-III), whose detectors are designed to reach energy thresholds below 100 eV. The data taking started in November 2020 and was concluded at the time of writing.

3.3.1 Goal of the Run

The main goal of Run36 was the study of possible origins of the LEE (see section 2.2.4). For this purpose, some characteristics of the CRESST-III modules (as described in 3.2.3) were modified in different modules to test specific hypotheses on the origin of the LEE, in particular related to the holding system, the presence of the scintillating foil and the material of the absorber crystal. Even though the main goal of the run was to gain a better insight into the origin of the LEE, the data have been used also to perform a DM analysis.

3.3.2 Run36 Detector Modules

During this run, CRESST had nine fully operating modules. Their characteristics will be summarized in the following.

- **Commercial CaWO₄** : Two modules employed commercially available CaWO₄ crystals as target material. The inner part of both modules' housing was not covered with the reflective foil. In addition, they were held with two bronze clamps instead of sticks. A possible connection of the excess with the scintillating foil or the holding method of the crystal could be tested with these modules.
- **In-house grown CaWO₄**: Three modules used CaWO₄ crystals that were grown at the *Technische Universität München* (TUM). These crystals were produced with a method that ensures less intrinsic stress compared to other CaWO₄ crystals previously produced at TUM and operated in the CRESST setup [74]. When compared to those previous measurements, these modules could be used to verify if intrinsic stress is a possible origin of the LEE. The inner part of these modules' housings were all covered with a reflective foil and the crystals were held by CaWO₄ sticks.
- **Silicon**: One module had silicon as a target material, not only for the crystal but also for the light detector wafer. Since silicon does not scintillate, the light detector was operated as an independent absorber so that the LEE could also be studied in a wafer detector.
- **Sapphire**: Two modules made use of sapphire crystals. This is a material that has been commonly used in previous CRESST measurements. In one of the two sapphires the scintillating foil was also removed.
- **Lithium aluminate**: Two modules used lithium aluminate as absorber material, marking the first time a lithium-based crystal is operated in the CRESST

underground facility. Besides testing the material dependence of the excess, this material allowed for probing spin-dependent elastic DM nucleon interactions. The analysis of one of these modules will be presented in chapter 5.

Chapter 4

Data Acquisition and Analysis

The raw data acquired with the procedure described in section 3.2.6 needs to be first processed to be suitable for the analysis steps. This process will be described in the first section of this chapter (the focus will be only on the continuous data stream, as it is the only one relevant to the analysis presented in this work). The second section presents the *low level analysis*, where a calibrated energy spectrum is obtained. The third section presents the *high level analysis*, where the dark matter results are derived, e.g. in the form of an exclusion limit.

4.1 Raw Data Processing

The goal of the raw data processing is to extract event windows of limited size (usually 655 ms) from the continuous stream. Such events are classified in three categories:

- **particle pulses**, which contain potential signal events
- **test pulses**, which contain artificial pulses
- **empty baselines**, which contain empty traces of noise

An example of each type of event can be seen in figure 4.1.

Pulses are extracted from the data stream by an offline triggering algorithm that scans the stream and identifies the timestamps of samples that are above a defined threshold value. The algorithm is not applied directly to the raw data stream, but to the stream filtered by an Optimum Filter (OF) that maximizes the signal to noise ratio and, as a consequence, allows to achieve lower trigger thresholds (see subsections 4.1.1 and 4.1.2). After triggering, event windows are extracted from the data stream during the event building step (see subsection 4.1.3). Finally, for each event several parameters are calculated that are used for analysis (see subsection 4.1.4).

The data processing is an iterative process that requires at least two iterations but for a better understanding, it will be presented in a conceptual way instead of chronologically.

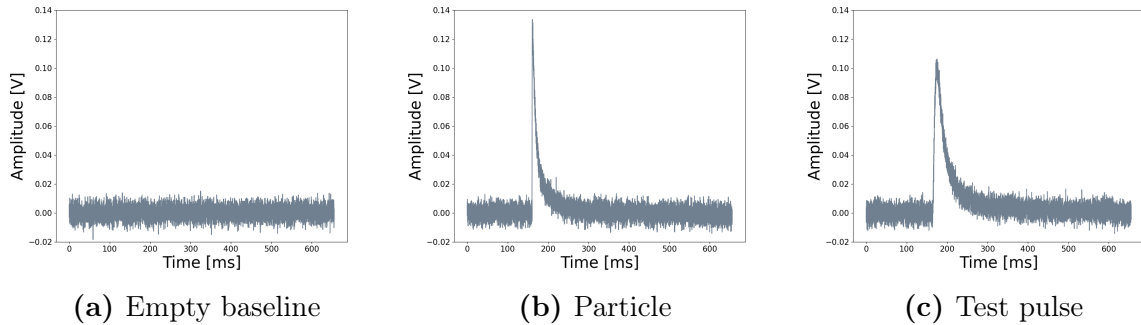


Figure 4.1: Example of (a) an empty baseline (b) a particle pulse (c) a test pulse.

4.1.1 The Optimum Filter

The Optimum Filter (OF) is defined by an optimization problem, namely the maximization of the signal-to-noise ratio (SNR) [75]. The key element of the OF is that it is tailored to the specific signal shape and the specific noise condition of the analyzed data. The information of these two elements is stored in a transfer function $H(\omega)$ that maximizes the SNR at the position of the signal maximum, τ_M . This transfer function is defined as

$$H(\omega) = K \frac{\mathcal{S}^*(\omega)}{\mathcal{N}(\omega)} e^{-i\omega\tau_M} \quad (4.1)$$

where $\mathcal{S}^*(\omega)$ is the complex conjugate of the Fourier transformed function $s(t)$ which describes the signal shape, K is a normalization factor and $\mathcal{N}(\omega)$ is the Noise Power Spectrum (NPS). Therefore, to build this transfer function two things are necessary: the noise power spectrum of the noise on the data stream and a description of the pulse shape $s(t)$ of the sought-for signal. The latter is obtained by creating a particle template (also called Standard Event - SEV).

The concept of filtering can be understood as the following: the continuous stream $c(t)$ is first Fourier transformed into the frequency space $\hat{c}(\omega)$ and subsequently transformed back into the time space, adding $H(\omega)$ as a weight factor

$$c(t) = \frac{1}{\sqrt{2\pi}} \int_{-\infty}^{\infty} H(\omega) \hat{c}(\omega) e^{-i\omega t} d\omega \quad (4.2)$$

Figure 4.2 compares raw data (gray) with filtered data (black) in the case of a small pulse close to threshold (left) and in the case of a higher pulse (right). The horizontal red line shows the trigger threshold for the data. From these figures it is evident that the filtered noise level is far below the trigger threshold. Instead, the same threshold would be too low for the unfiltered data, as it would generate a significant amount of noise triggers.

Standard event Creation

The goal of the SEV creation is to derive a function $s(t)$ that describes the signal shape without the underlying noise. For this purpose, a set of events which are identified as

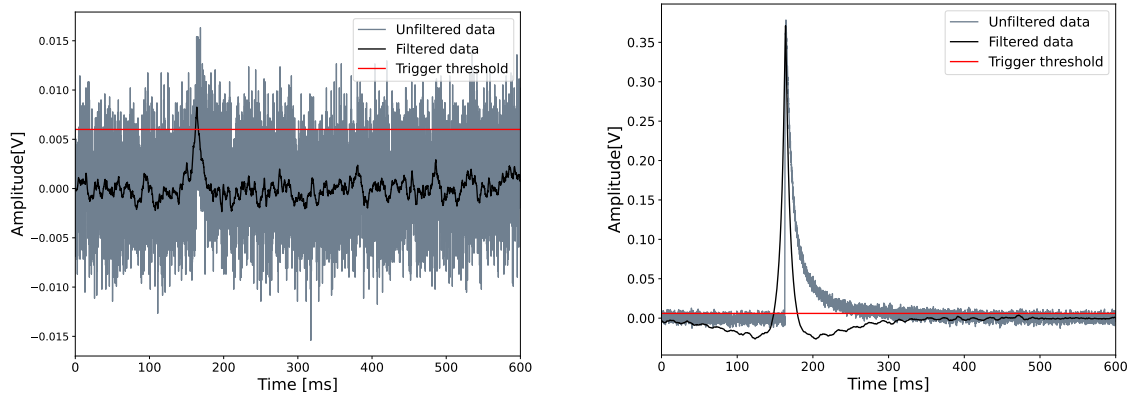


Figure 4.2: *Left:* Example of a pulse with an amplitude close to the trigger threshold. The raw data is depicted in gray, while the data filtered with the optimum filter is represented in black. The horizontal line in red is the trigger threshold that can be achieved thanks to the OF. *Right:* Analogous to left, unfiltered versus filtered data, for the case of a pulse with an amplitude well above the threshold level.

particle pulses are selected and averaged. In order not to alter the particle shape, events used to create the SEV should not contain any distortion, should all have the same onset and should have a similar amplitude in the linear regime of the detector response. Thanks to the averaging of the pulses the underlying noise cancels out, leaving the particle shape preserved. Typically, the SEV is averaged from events induced by a calibration source (^{55}Fe in this case).

Such events are useful as they produce a set of pulses with the same amplitude and with a high occurrence rate, which is important to cancel out the underlying noise.¹ The possibility to use events from the calibration source for the SEV relies on the caveat that the shape of a pulse generated by a nuclear recoil is equivalent to the one generated by electron or gamma events.

Once $s(t)$ is obtained, it is Fourier transformed to calculate the transfer function $H(\omega)$ (see figure 4.4 (a)). This transfer function is then used to filter the SEV

$$s_{OF}(t) = \frac{1}{\sqrt{2\pi}} \int_{-\infty}^{\infty} H(\omega) \hat{s}(\omega) e^{-i\omega t} d\omega \quad (4.3)$$

obtaining a filtered SEV that does not preserve the shape of the pulse but only its amplitude, which is the relevant information for the energy estimation. Figure 4.3 shows an example of a SEV before filtering (left) and after filtering (right). The aforementioned procedure can be applied to calculate a SEV for test pulses as well. In this case, only test pulses with the same amplitude are selected.

¹If the available statistic is not enough to cancel out the baseline noise, an additional step that can be performed is a **parametric fit** of the SEV, adjusting the parameters of the mathematical description presented in section 3.1.3. This parametric fit preserves the signal shape, removing the underlying noise completely.

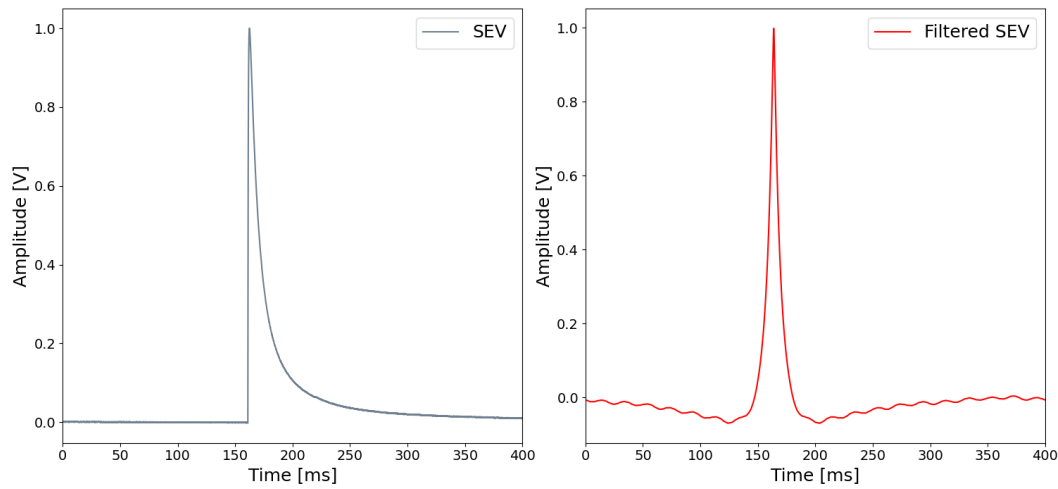


Figure 4.3: Example of a particle standard event before (left) and after filtering (right).

Noise Power Spectrum Creation

The noise power spectrum (NPS) is obtained as an average of the spectral distributions of a selection of empty baselines. Each empty baseline window $n_i(t)$ is Fourier transformed and used to calculate $\mathcal{N}(\omega)$, i.e. the average $\langle \hat{n}_i(\omega_k) \hat{n}_i^*(\omega_k) \rangle_i$ of all empty baselines. The selection of empty baselines should be representative of the noise conditions throughout the whole data set and should contain neither signals nor artifacts. An example of NPS can be seen in figure 4.4 (b). In typical noise power spectra, the low frequencies are populated by slow baselines fluctuations while the high frequency mostly originate from electronic interference. Some spikes are present, for instance the 50 Hz spike which comes from the power network. Figure 4.4 shows the two components used to create the filter (SEV and NPS) close to the resulting transfer function $|H(\omega)|^2$ (c). Comparing the three plots it becomes evident that in the filter transfer function the frequencies of the SEV are present, while those which are prominent in the NPS are reduced.

4.1.2 Triggering Process

Once the OF is created, it can be used to filter the raw data for the triggering process. Before triggering, a trigger threshold is chosen, based either on the baseline resolution of the filtered data or on the number of accepted noise triggers. Both methods will be described in this section, followed by a description of the triggering algorithm.

Baseline Resolution Determination

The baseline resolution quantifies the noise level in a detector and therefore it is an important parameter that, among others, can be used to quantify the performance of a detector. Its value is useful to determine the order of magnitude of the trigger

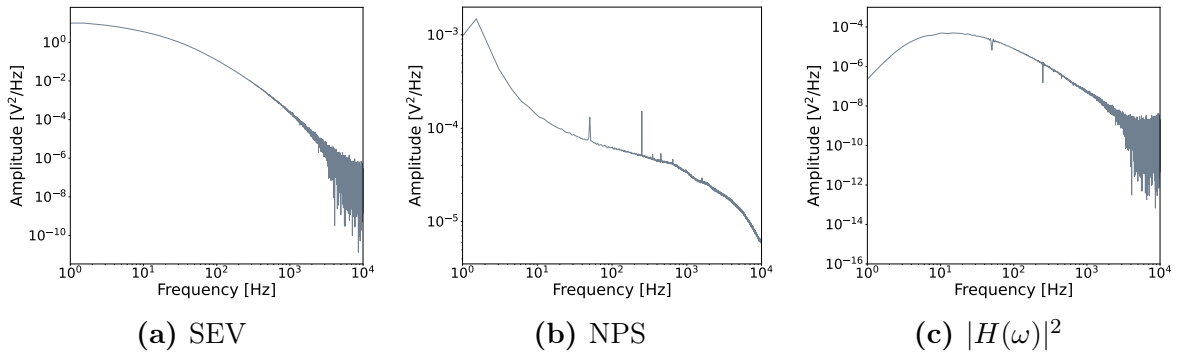


Figure 4.4: (a) Example of a standard event (SEV) in Fourier space. (b) Example of a noise power spectrum. (c) Spectral shape of the filter resulting from (a) and (b), used for the optimum filter.

threshold. In the past, the CRESST collaboration chose the trigger threshold to be 5σ of the baseline resolution. Nowadays, it adopts the method described in the following section.

The method to determine the baseline resolution is to superimpose a SEV of a fixed height on a set of clean empty baselines. Usually, the same baselines selection used to create the NPS is used. Then, the amplitude of each event is evaluated with the filter. The resulting amplitude distribution can be seen in figure 4.5. Since the SEV is a noiseless pulse of a fixed amplitude, the width of the distribution is a measure of the noise present on the empty baselines. This distribution is then fitted with a Gaussian function and its width σ represents the baseline resolution.

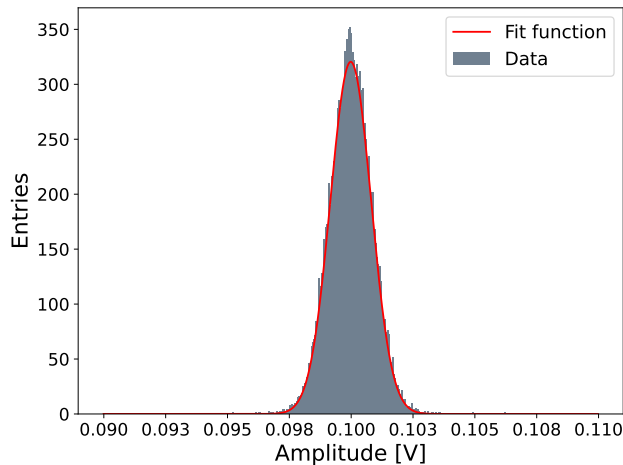


Figure 4.5: Example of the filter amplitude distribution for a SEV of fixed height, superimposed on empty baselines. In red, the result of the fit with a Gaussian distribution can be seen. The width σ represents the baseline resolution.

Threshold Determination with Noise Triggers

For the determination of the trigger threshold, CRESST adopts the method described in [76]. The basic concept of this threshold estimation is to evaluate the amplitude at which a specific number of noise triggers is accepted in the data set. In CRESST analyses, a noise trigger rate of 1 count per kg d of exposure is usually accepted.²

To describe the noise trigger rate one has to define the probability that a sample, contained in a window of size d (which contains only noise), exceeds the trigger threshold x_{max} . This probability depends on the distribution of the noise samples $P(x)$, as well as on the size of this window d . Assuming that each sample is statistically independent, this probability is:

$$P_d(x_{max}) = \frac{d!}{1!(d-1)!} \cdot P(x_{max}) \cdot \left(\int_{-\infty}^{x_{max}} P(x) dx \right)^{d-1} \quad (4.4)$$

Since noise is expected to be white, the distribution of the noise samples $P(x)$ is assumed to be Gaussian, and $P_d(x_{max})$ becomes

$$P_d(x_{max}) = \frac{d}{\sqrt{2\pi}\sigma} \left(e^{-\left(\frac{x_{max}}{\sqrt{2}\sigma}\right)^2} \right) \left(\frac{1}{2} + \frac{\text{erf}(x_{max}/\sqrt{2}\sigma)}{2} \right)^{d-1} \quad (4.5)$$

With this distribution, the noise trigger rate (NTR) per kg d of exposure can be calculated as a function of the trigger threshold x_{thr} :

$$NTR(x_{thr}) = \frac{1}{t_{win} \cdot m_{det}} \int_{x_{thr}}^{\infty} P_d(x_{max}) dx_{max} \quad (4.6)$$

where t_{win} is the time length of the trigger window and m_{det} is the detector mass. In light of this, the first step of the threshold determination is to obtain a distribution of maxima for the noise of the specific data set. This distribution can be obtained from the same selection of empty baselines used for the NPS creation. The maximum value of each empty baseline window is then evaluated with the filter. An example of this distribution can be seen in figure 4.6 (left). The red line represents the fit result, using equation 4.5. For this case, the assumption of Gaussian distributed noise samples (i.e. white noise) represents the data well. In cases of a non-Gaussian distribution, which typically originates from artifacts causing upward fluctuations, equation 4.5 should be modified with the correct distribution.

In a second step, the fit parameterization can be adopted to calculate the NTR as a function of the threshold. An example of this function can be seen in figure 4.6 (right). From the distribution in the right plot of figure 4.6 one can extract that a trigger threshold of 5.5 mV corresponds to one noise trigger per kg d exposure.

²The number of noise triggers that can be accepted without polluting the spectrum depends on the specific conditions of the experiment, i.e. the event rate close to threshold.

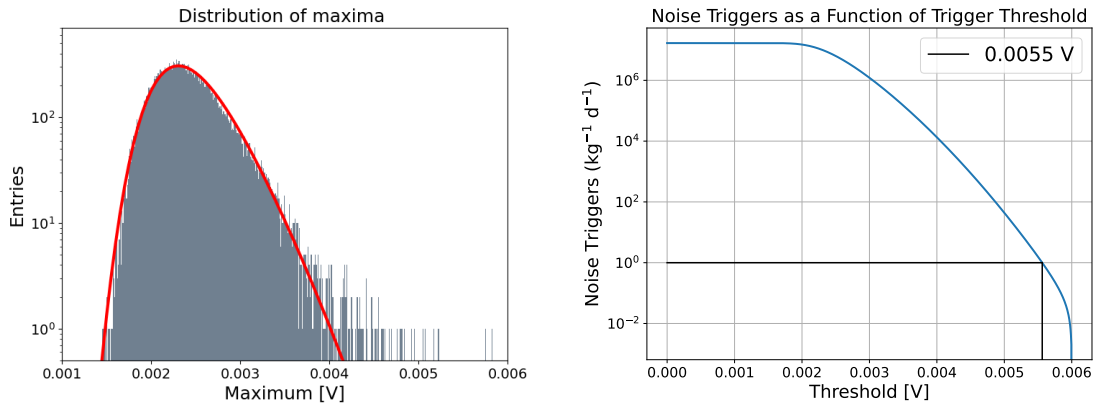


Figure 4.6: *Left:* Example of a distribution of maxima. The red line represents the fit result, using equation 4.5. *Right:* Example of the noise trigger rate as a function of the trigger threshold.

Triggering Algorithm

After filtering the data stream, and choosing the trigger threshold, the triggering process consists of scanning the filtered stream with the goal of recognizing pulses. The trigger is fired once a sample in the stream exceeds the chosen threshold. However, the sample firing the trigger does not always coincide with the onset position of a pulse. In fact, the filtered stream directly before and after a pulse presents a wave-like shape, as can be seen e.g. in figure 4.2 (right). The height of such "wiggles", which depends on the pulse amplitude and the noise conditions, might fire the trigger in some cases. Due to this possible scenario, the trigger algorithm is optimized to identify the timestamp of the *real* pulse. This is visualized in figure 4.7.

In short, this algorithm searches the highest sample within a short window after the first sample firing the trigger. An important consequence of this trigger algorithm is that in the case where two signal pulses are contained in one search window, only the highest is considered as triggered. The final output of the trigger algorithm is a list of timestamp values. This output is then used in the next data processing step, the *event building*.

4.1.3 Event Building

The following step of the data processing consists of extracting signal events from the continuous stream by creating time windows referred to as *events*. The size of these windows is chosen to be long enough to exceed the relaxation time of sought-for pulses, in order to ensure a complete pulse description. Commonly, for CRESST-III data, these windows have a size of 655 ms. The window is built by adjusting the timestamp of the triggered amplitude at 1/4 of the total window size, as can be seen e.g. in figure 4.2. Pulses that are present in an event window because they directly precede (having a smaller amplitude) or follow an event tagged as triggered are referred to as *pile-up*. During the event building step, also some events without any triggered pulse are

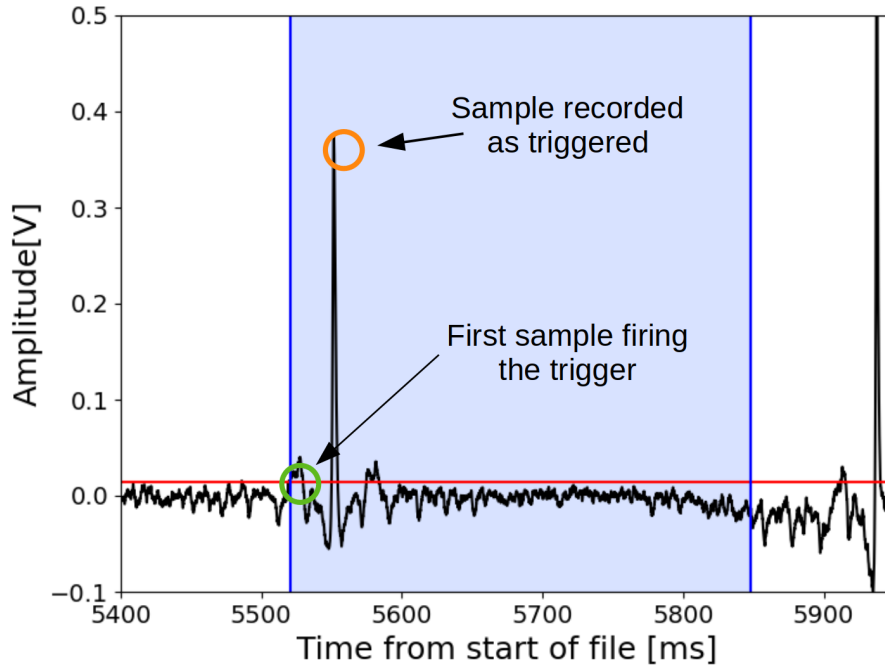


Figure 4.7: Visualization of the triggering of the filtered stream. The red line represents the trigger threshold. The green circle shows the first sample firing the trigger. The blue region delimits the window where the highest sample is searched for. The orange circle represents the highest sample (within this window) which is then recorded as the triggered one.

created, the **empty baselines** that contain only empty traces of noise. These events are crucial for the determination of the noise conditions of a measurement and therefore for the filter creation and for the threshold estimation.

Since the time at which test pulses are sent and the value of the injected voltage are known, these pulses can be tagged during the event building step. To do this, a parameter called TPA (Test Pulse Amplitude) is written. For every window containing the timestamp of a TP, the assigned TPA contains the voltage value injected by the heater.³ Every other event is assigned a TPA equal to 0. The empty baselines have instead a negative TPA value. Thanks to this parameter three categories of events can be defined during analysis:

- $\text{TPA} > 0 \rightarrow$ Test pulses
- $\text{TPA} = 0 \rightarrow$ Particles
- $\text{TPA} < 0 \rightarrow$ Empty baselines

As a consequence of this classification, events containing a particle event at the trigger onset and followed or preceded by a smaller TP, are tagged as test pulses.

³The timestamp of the TP does not necessarily coincide with the timestamp of the pulse triggering the event, e.g. a TP injected in the detection in close vicinity to a large particle pulse.

Finally, during the event building step the response of the two detectors of a module (phonon and light) are combined, namely events in the individual channels with the same timestamp are combined to one single event in coincidence.

4.1.4 Calculation of Main Parameters

In order to describe the characteristics of each signal event, some parameters are defined. In this section, the most important ones will be presented.

Baseline Parameters

- **Baseline difference:** This parameter describes the difference of the baseline height at the beginning and at the end of a window. It is calculated as the difference of the averaged first and last 50 samples of a window.
- **Baseline RMS:** This parameter is the RMS deviation of the first quarter of the window (pre-trigger region) from a linear fit. It is useful to recognize the momentary noise condition of an event or to identify pile-up preceding the onset.
- **Baseline offset:** This parameter describes the voltage value at which the baseline is positioned. After a flux quantum loss (described in section 3.2.4), the baseline offset value jumps to a different one, where it remains until the next flux quantum loss occurs.

Amplitude Parameters

- **Pulse Height:** This parameter is a very simple amplitude estimator. It is calculated by performing a moving average over 50 samples. The difference between the highest point and the baseline is then recorded as pulse height. This amplitude estimator is useful in cases where a fast pulse height estimation is needed (e.g. monitoring during the data taking).
- **Filter amplitude:** The OF can be applied as an amplitude estimator of an event. For this purpose, the difference between the highest point and the baseline in a filtered event window is saved as *filter amplitude*. The maximal value can be either searched in the complete window, or at a fixed position. For particle events, the filter amplitude is evaluated at the trigger timestamp. This amplitude estimator provides an excellent resolution thanks to the filtering of the noise. However, its estimation is only valid in the linear range of the detector and leads to erroneous amplitudes for saturated pulses.
- **SEV fit amplitude:** A pulse amplitude can be also estimated with a standard event fit. Here, the pulse amplitude is estimated by superimposing and scaling the standard event on the event under consideration. The scaled amplitude of the SEV that ensures the lowest RMS between the samples of the real data and the template is stored as amplitude value.

- **Truncated SEV fit amplitude:** The SEV also allows for the possibility of reconstructing the amplitude that saturated events would have had in the case of a larger linear regime. This feature is called **truncated fit**. This fit consists of the same scaling procedure described before, but in this case only the samples within the linear regime are actually considered for the RMS minimization. An example of this fit can be seen in figure 4.8 (right plot). In this figure it can be noticed that the fit amplitude (black line) is higher than the real pulse height (gray).

The value of the highest sample that should be fitted is called the **truncation limit** and it corresponds to the end of the linear regime of the detector. This limit can be estimated by performing an un-truncated fit (fit without truncation limit) and then analyzing the behavior of the fit RMS over the fit amplitude (see figure 4.8 - left). The value at which the RMS value starts to increase represents the value at which the shape of the pulse begins deviating from the SEV, due to the transition into a non-linear region of the transition curve. This value is imposed as truncation limit (red line in figure 4.8).

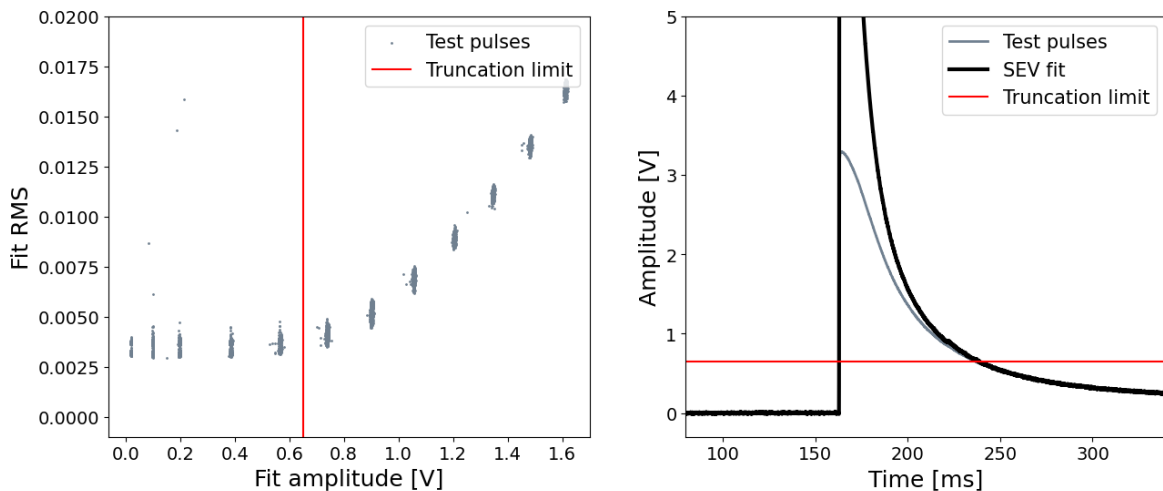


Figure 4.8: *Left:* Fit RMS plotted against fit amplitude. This plot is used to determine the truncation limit. In this example the truncation limit is at 0.65 V (red line). *Right:* Example of a truncated fit. The truncation limit is shown with the red horizontal line.

Shape Parameters

- **Filter RMS:** This parameter is the root mean square (RMS) deviation of the filtered SEV and the event under consideration. It is a powerful parameter to distinguish pulses with a shape differing from the SEV.
- **SEV Fit RMS:** This parameter describes the RMS deviation of the SEV and the real event. Also this parameter is useful to identify pulses with the correct pulse shape.

- **Onset:** This parameter describes the position of the rise of a pulse. It is calculated by scanning the samples before the highest one (used for the pulse height) - the position of the first of these samples that is lower than three times the baseline RMS is the *onset*.
- **Maximum and Minimum Derivative:** To calculate these parameters the derivative of a raw pulse is calculated. These parameters give the steepest rise and steepest decay between two samples. This parameter is useful to recognize sudden jumps in the stream that might originate from electronic artifacts.

4.2 Low Level Analysis

The goal of the *low level analysis* is to obtain the energy spectrum of the recorded data. An important step to get this spectrum is the data cleaning, where the aforementioned parameters are used to select only events whose amplitude estimation is reliable. It is important that this step is performed without any bias, meaning that the choices of the analysts should not be influenced by the final result. Such bias is avoided by performing a **blind analysis**. For a blind analysis, the analyst does not look at the complete data set but only at a portion of it, not statistically significant, called the **training set**. The single files that compose the training set are chosen within a distance of a few weeks, to sample possible changes of the operating condition, and avoid performing an analysis which is valid in a limited time of the data taking.

After the data selection, the calculated amplitudes of each event have to be converted into an energy value and then the efficiency of the applied cuts is estimated with a simulation. The outcome of these steps performed on the blind data set is then used for high level analysis.

The plots shown in this section are produced using the data of the training set for one of the lithium aluminate modules of Run36 (Li1 module).

4.2.1 Data Selection

After the triggering process, the following analysis step is the data selection. The goal of this step is to select only those events whose correct energy estimation can be ensured. To achieve this, four types of cuts are performed on the data set: the *stability cut*, the *rate cut*, the *quality cuts* and finally the *coincidence cuts*. While the first two aim at removing specific time periods from the data sets, for the last two the discrimination is done on an event-by-event basis.

Stability Cut

The objective of the stability cut is to remove the sections of the data stream where the operating point of the detector being analyzed deviates significantly from the average condition. As mentioned in section 3.2.5, the height of the control pulse (CP) is used to determine the operating point. A deviation from the mean height of the CP is a

sign of a deviation of the operating point. Therefore, for the stability cut, the data stream is divided into sections limited by two consecutive CP. The unstable periods are defined by a CP with a pulse height that deviates more than 3σ from the mean pulse height (see figure 4.9). Every stream section limited by an anomalous CP is considered unstable, and removed from the data.

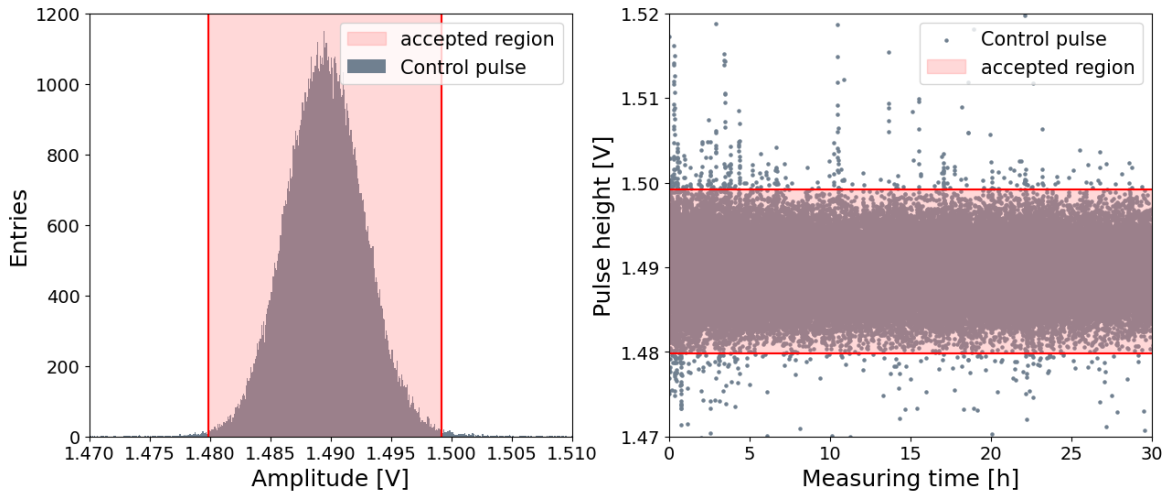


Figure 4.9: *Left:* Distribution of the control pulse height. *Right:* Distribution of CP height (y-axis) over time (x-axis). In both plots, the shaded red area represents the 3σ deviation from the mean value, which is accepted by the stability cut.

Rate Cut

With the rate cut, time periods with an anomalously high trigger rate are removed. The known background expected in the detector, as well as dark matter, are expected to produce an almost constant rate. Therefore, occasional rapid successions of events are assumed to originate from disturbances. For the rate cut, the data stream is divided in bins of 10 minutes. The bins with a rate 3σ higher than the mean rate (as well as the one before and after) are removed from the data.

Quality Cuts

For the quality cut, the parameters described in section 4.1.4 are used. Usually only a few of them are required and will be described in this section. It is important that the quality cuts do not remove a specific population of events to obtain a realistic energy spectrum. Slight energy dependencies of cuts are acceptable, as they will be accounted for when correcting the spectrum with the energy dependent cut-efficiency.

Baseline difference cut: This cut is very useful to remove two types of events: baseline changes (caused by flux quantum losses or SQUID resets) and decaying baselines. The former are described in section 3.2.4. The latter occur when the detector returns to thermal equilibrium in a time longer than the event window. For

instance, a very energetic interaction might cause a pulse whose tail will exceed the event window and trigger the next one, whose resulting event window contains only a decaying baseline. Figure 4.10 shows an example of baseline difference distribution as well as the three classes of pulses that were described: a decaying baseline, a flux quantum loss and a SQUID reset.

Baseline RMS: The baseline RMS cut is effective in removing events with irregularities in the pre-trigger region, for example a pile-up pulse.

Delta Voltage cut: The delta voltage parameter is composed of two parameters described in section 4.1.4. It can be calculated as

$$\Delta V = \frac{\text{Minimum derivative}}{\text{Baseline RMS}} \quad (4.7)$$

This parameter quantifies the change between two consecutive samples with respect to the noise level. Electronic artifacts, such as delta spikes, can be discriminated with this parameter. Figure 4.11 shows an example of a delta voltage distribution and of a delta spike. Since the *minimum* derivative is used (and not the *maximum* derivative) downwards fluctuations are typically removed, and pulses with very fast rise times are not affected by this cut.

Filter RMS cut: The filter RMS parameter is used to discriminate pulses based on their shape. With this cut, pulses with a shape different than the SEV can be recognized. This cut can remove every event that does not originate from a particle interaction or whose amplitude cannot be correctly estimated (e.g due to pile-up, or because it exceeds the linear regime).

Coincidence Cuts

Dark matter interactions with the target nuclei are expected to be rare and generate a nuclear recoil in maximally one detector at a time. Therefore, particle events which triggered a few nanoseconds before or after a trigger in other detectors, are most likely not originating from dark matter and are discarded.

Furthermore, events occurring in temporal proximity to a muon-panel trigger might contain a muon-induced neutron event in the absorber (see section 3.2.1) and are therefore also discarded. However, most of the events recorded in the muon panels are caused by gamma particles and are not correlated to the coincident events in the detectors. Therefore, a time-window is excluded, which is just long enough to remove causal coincidences with the muon-panel, without introducing an excessive reduction of the exposure. Typically, particle events that have been recorded less than 5 ms before or after a muon-panel event are rejected. A muon-induced neutron event would generate a muon-trigger before a detector trigger. Nonetheless, also particle events that trigger before a muon event are removed, to account for the worse time resolution of detectors compared to the muon panels. An example of the distribution of the time differences between events and triggers in the muon panel can be seen in figure 4.12.

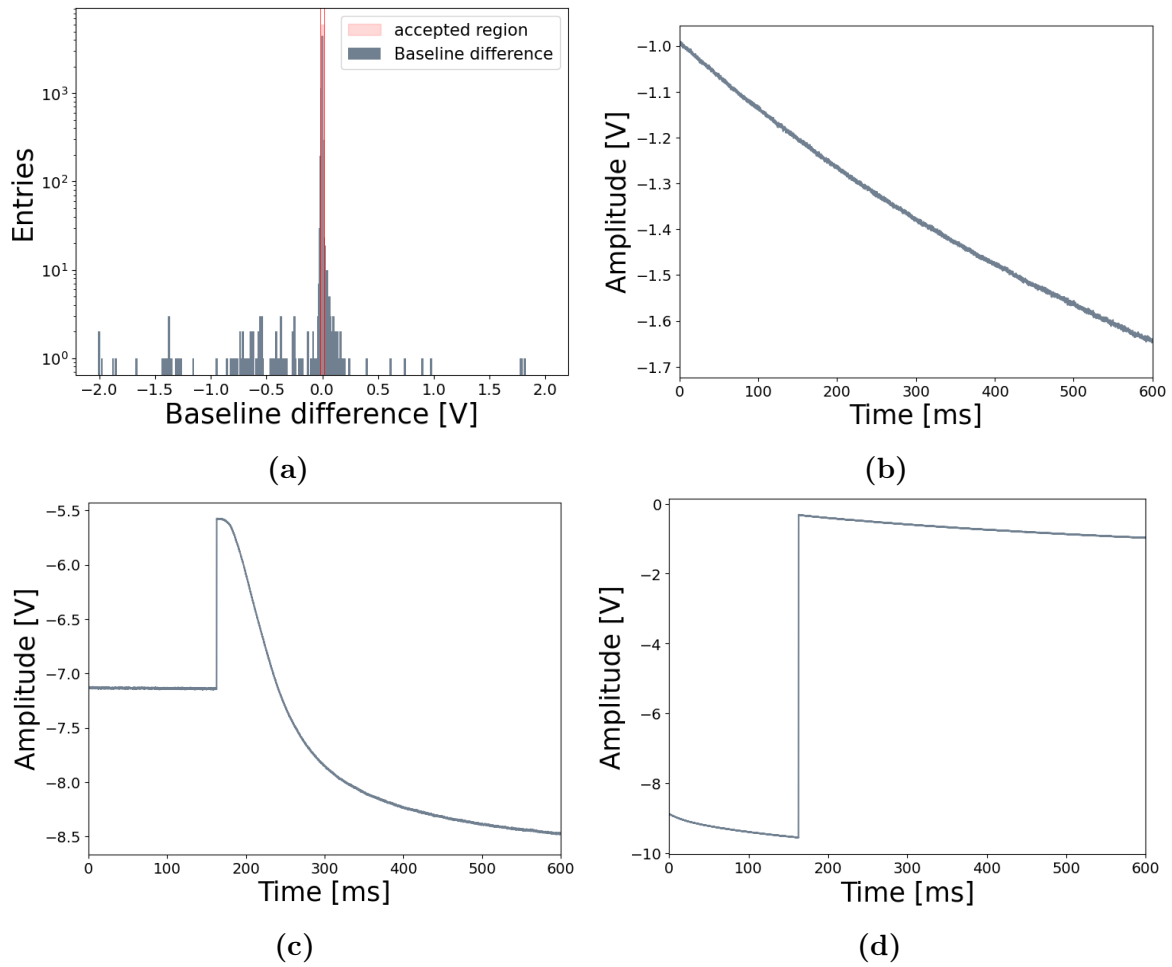


Figure 4.10: (a) Example of a distribution of the baseline difference. In red a typically accepted region is marked. (b) Example of a decaying baseline. (c) Example of a flux quantum loss. (d) Example of a SQUID reset.

Positive values represent events triggering after a muon-veto trigger, while events with a negative value triggered before. The exponential behavior on both sides coincides with the distribution expected from random coincidences.

4.2.2 Energy Determination

After the data cleaning step, the energy of the selected clean events needs to be determined. This process requires two steps. First, the amplitude of each event is corrected with respect to the small variations of the operating point over time. Then the corrected amplitude is converted into an energy value.

Before looking at the details of these two steps it is important to remember that the amplitude that is calibrated can be estimated with one of the methods described in section 4.1.4. The filter amplitude estimator provides the best resolution and therefore is used for dark matter analysis. Since the amplitude estimation of this parameter is

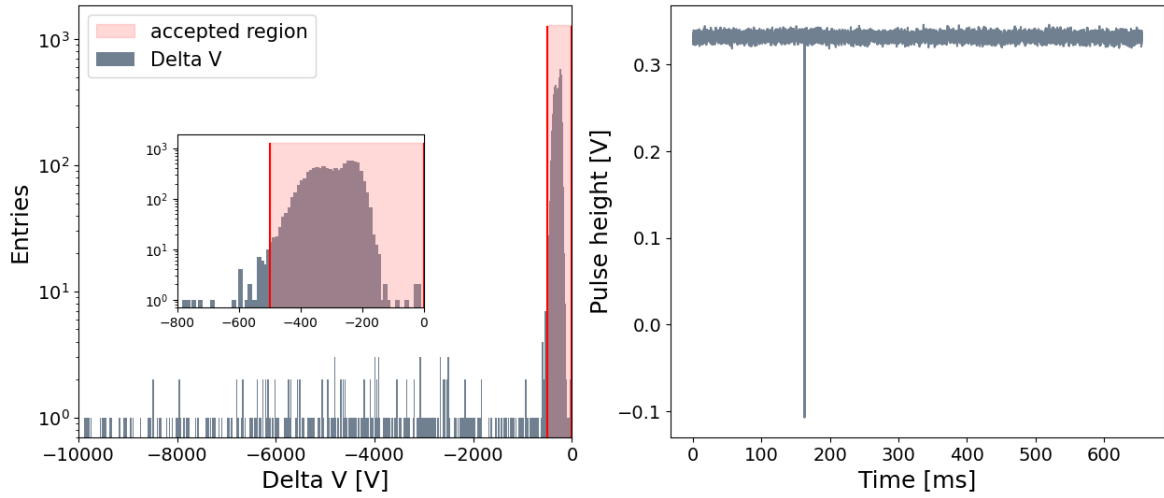


Figure 4.11: *Left:* Example of a delta voltage distribution with a typical accepted region in red. *Right:* Example of a delta spike.

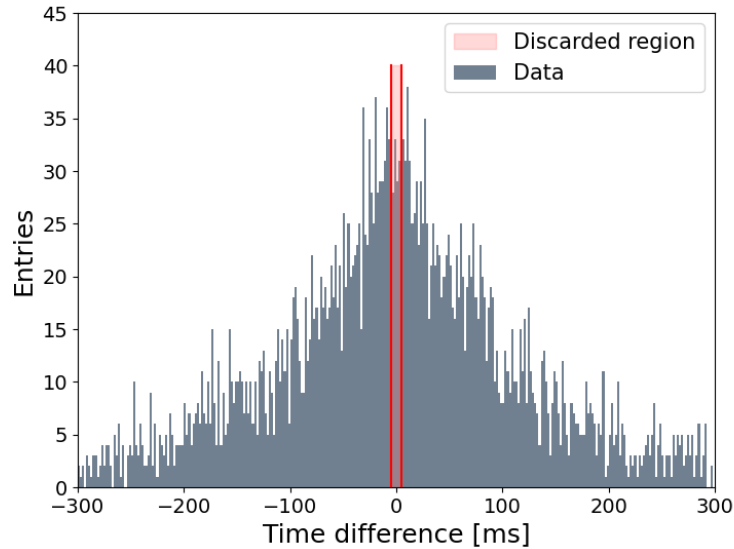


Figure 4.12: Distribution of time differences of events from triggers in the muon panels. The red shaded area shows the typically removed region.

valid only in the linear regime of the detector response, the energy spectrum obtained is valid until the truncation limit (see section 4.1.4).

Amplitude Conversion into Injected Voltage

Although unstable data taking periods are removed with the stability cut, small variations (within 3σ of the CP pulse height) in the detector response can still be present in the data set. Because of these small variations, a given deposited energy

might translate into different reconstructed amplitudes at different moments in time. Small variations can be accounted for thanks to the presence of test pulses of different values constantly injected in the detectors (see section 3.2.5) that are used to monitor the detector response over time and can be used to correct for it. For this purpose, a specific filter for the test pulses is created and used to determine their amplitude. For each TP value the measured amplitudes over time are smoothed with a Gaussian kernel (width of 0.5 h). The result is finally stored in an object called **Test Pulse Response** (TPR). The TPR provides a description of the detector response over time (it can be seen in figure 4.13). The left plot shows the pulse height of different test pulses over time and the smoothing result in red. The right plot shows a zoom into only one TPA. From this second plot it is clearly visible that besides the normal spread of the amplitude estimation, given by the energy resolution of the detector, the reconstructed amplitude of one TPA shows small and slow fluctuations caused by variations of the operating point.

Assuming that the reconstructed amplitudes have the same time dependence for test pulses and particles pulses, the TPR can be used to correct the small fluctuations of the reconstructed pulse amplitude for particle pulses. This is done in several steps, where the final goal is to convert the amplitude of each particle event into an injected voltage equivalent value, that is time independent (analogously to the injected voltage of test pulses). First, the TPR is evaluated at the timestamp of the particle event. Secondly, these values are interpolated with a cubic spline to create an amplitude transfer function. This function maps the reconstructed amplitude of TP to the corresponding injected voltage at the time of the particle event and can be used to convert the reconstructed amplitude of the pulse into an injected voltage equivalent value, that is stored in a new parameter, the Test Pulse Equivalent (TPE). An example of this transfer function can be seen in figure 4.14.

Amplitude Calibration

The last step of the energy determination is the calibration of the converted amplitudes. For this purpose, the detector response to a gamma source of known energy is used. The adopted source is an iron source (^{55}Fe) with an activity of $\sim 1\text{mBq}$. This iron isotope decays into ^{55}Mn via electron capture. The vacancy generated in the K-shell of the ^{55}Mn atom is then filled by an electron of higher shells. During this process X-rays at 5.89 keV (K_α) and 6.49 keV (K_β) are emitted. The X-ray emission at 5.89 keV is used to calculate a conversion factor from injected voltage to energy units, called **CPE factor** (Convert Pulse height to Energy). This factor is determined by fitting the TPE distribution in the region of the peaks originating by the two K-lines using a double Gaussian function. The mean value of the first Gaussian (K_α) is then used to determine the CPE factor. An example can be seen in figure 4.15. Following this example, the CPE factor is calculated as

$$CPE = \frac{5.89 \text{ keV}}{1.89 \text{ injV}} = 3.11 \frac{\text{keV}}{\text{injV}} \quad (4.8)$$

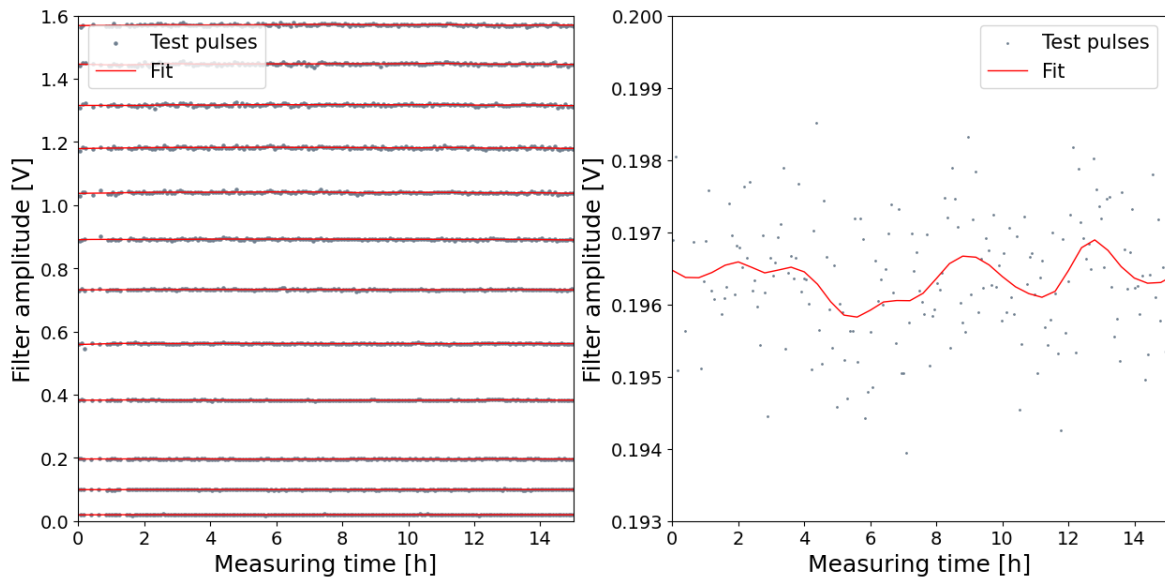


Figure 4.13: *Left:* Distribution of test pulse height over 15 hours (gray). In red the Gaussian smoothing fit can be seen, which is referred to as TPR. *Right:* Zoom of only one TP.

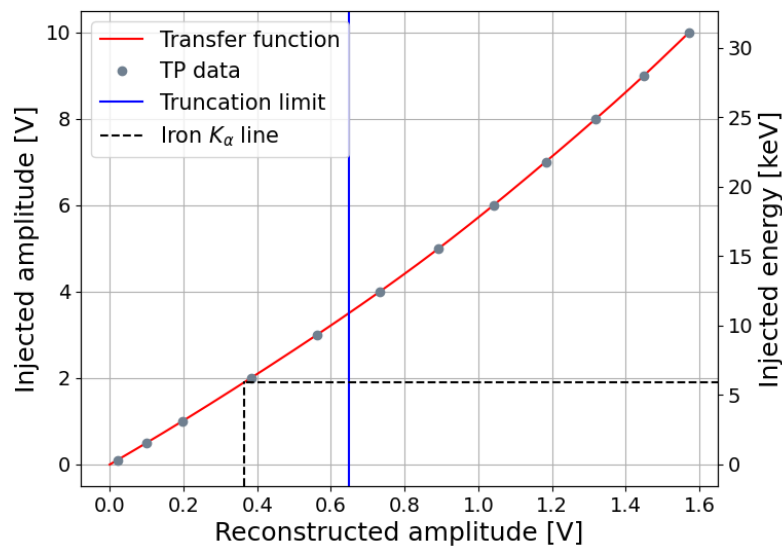


Figure 4.14: Example of a transfer function from reconstructed voltage to injected voltage. The reconstructed amplitude (x-axis) is mapped to a TPA value, or injected amplitude value (left y-axis). The right axis represents the injected energy value, which is the left y-axis multiplied by the CPE factor. The blue line shows the end of the region where the detector response is linear.

Once the CPE factor is calculated, the TPE of each particle event is multiplied by it, resulting in the final energy spectrum. While in figure 4.15 only the range of the

iron events has been shown, this procedure is done for the complete energy spectrum. However, since the filter amplitude estimation is valid only in the linear regime, the final energy spectrum is only valid for reconstructed values below the truncation limit. For the CPE factor of the light channel, the scintillation light emitted by iron hits in the crystal is used. Therefore, the energy of the light channel is calibrated in electron equivalent energy units (keVee). Once the final energy spectra of the phonon and the light channel are obtained, the light yield plot can be created. How this plot can be used in the analysis, will be described in the high level analysis section.

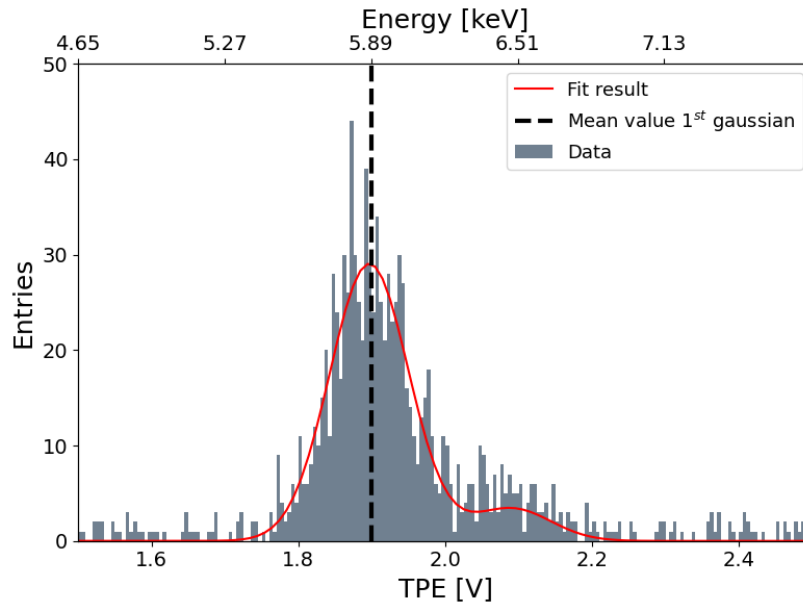


Figure 4.15: TPE distribution of events originating from the calibration source. The lower x-axis shows the voltage values, while the upper x-axis shows the calibrated values. The red line shows the fit results of two Gaussian functions which describe the K_{α} and K_{β} lines of ^{55}Mn originating from the ^{55}Fe decay. The black vertical line is the mean value of the first Gaussian which is used to calculate the CPE factor.

Calibration Factor

A calibration factor is needed to translate the measured voltage values into energy (e.g. for the energy threshold and baseline resolution). This factor is obtained by combining the CPE factor (previously described) and the ratio between the lowest measurable TP amplitude and its corresponding TPA:

$$\text{Conversion factor} = CPE \left[\frac{\text{keV}}{\text{injV}} \right] \cdot \frac{TPA}{TP_{Amp}} \left[\frac{\text{injV}}{\text{V}} \right] \quad (4.9)$$

The latter represents the conversion factor between injected and measured voltage and is evaluated at the lowest measurable TP amplitude to ensure that the calibration of

the detector response is valid for values close to threshold. For the example presented in the figures 4.13 - 4.15, the calibration factor is

$$\text{Calibration factor} = \frac{5.89}{1.9} \left[\frac{\text{keV}}{\text{injV}} \right] \cdot \frac{0.1}{0.02} \left[\frac{\text{injV}}{\text{V}} \right] = 15.5 \frac{\text{keV}}{\text{V}} \quad (4.10)$$

With this factor the threshold value of 0.0055 V corresponds to 0.085 keV.

4.2.3 Efficiency Estimation

The last step of the low level analysis is to determine the probability with which an event survives first the trigger (**trigger efficiency**) and afterwards the data selection process (**survival probability**). The survival probability, which quantifies the cumulative effect of triggering and data selection, is needed to correct the energy spectra that are the experimental input to the high level analysis. To calculate this survival probability, a stream filled with artificial events in a given energy range is passed through the same analysis pipeline of the real events.

Simulation Creation

The simulation data set is used to calculate the probability with which events of each given energy survive the analysis chain steps. The simulation data set is created by superimposing a particle template (that represents signal events) on the real data stream. For this purpose, the signal shape should not present any underlying noise.⁴ Events are simulated on the real data stream at random moments in time with a rate that can be chosen by the analyst. To reproduce the conditions of a rare event search, the aim is to have simulated events containing single pulses, therefore the rate is chosen such as to result in an average of one simulated pulse per event window.

The goal is to simulate a flat energy spectrum from 0 energy to a value that corresponds to the end of the energy spectrum of the real data (if the filter amplitude is used as an energy estimator, it should not exceed the linear range).

Simulated Spectrum

Since the detector response varies in time, a given energy value does not translate into the same amplitude value at each moment in time. The generation of a spectrum of amplitudes that represents a flat energy spectrum requires the following steps. First, a set of flat distributed energy values is created within the desired energy range (from 0 to the end of the linear regime). These values are stored in the **simulated energy** parameter. Second, a random position of the data stream (in the form of a timestamp) is assigned to each energy value. Third, the amplitude that translates to that energy in that specific moment is derived. This last step is done with the reversed step adopted during the calibration: the energy value is divided by the CPE factor (to derive the injected voltage equivalent value) and then the corresponding amplitude value is

⁴In this case a parametric fit is more suitable than a SEV.

inferred with the transfer function at the required timestamp. Finally, a template pulse of the amplitude so derived is added to the stream at the corresponding timestamp. As a final result of this procedure, a simulated energy spectrum as well as a simulated amplitude spectrum are created.

Trigger Efficiency

The simulated spectrum allows for the estimation of the probability with which events survive the trigger algorithm. This is done by passing the stream containing the simulated events through the triggering process. Events that contain exactly one simulated pulse are defined as *simulated data*. The subset of this data set that survives the trigger algorithm is defined as *triggered events*. The trigger efficiency is then given by the ratio of the simulated energy per each bin (with the typical size of 1 eV) in the two data sets, as can be seen in figure 4.16. The distribution presents a smearing close to threshold, which is caused by the finite energy resolution of the detector. The energy dependence of the trigger efficiency can be described with a step function convoluted with a Gaussian distribution given by the detector energy resolution:

$$y(E) = \frac{y_{eff}}{2} \left(1 + erf \left(\frac{E - E_{thr}}{\sqrt{2}\sigma} \right) \right) \quad (4.11)$$

where y_{eff} is the constant part of the **trigger efficiency**, E_{thr} is the **energy threshold** and σ the resolution at threshold. With this description, the energy threshold corresponds to the simulated energy value where the error function drops below half of its constant value (red line in figure 4.16). This threshold value should correspond to the trigger threshold (in Volt) expressed in energy units. The value y_{eff} does not correspond to a 100% efficiency, even at energies well above threshold, since not every simulated particle (present in the reference data set) is finally tagged as triggered particle pulse. This energy independent reduction of the trigger efficiency is an effect equivalent to a trigger dead time, caused by two types of pile-up. The first type is represented by simulated pulses that come directly before or after a higher real pulse or artifact. Since the trigger algorithm selects only the highest pulse, such simulated pulses are not reconstructed at 1/4 of the window and are considered pile-up events and removed from the triggered events. The second category concerns pulses that contain a TP in the same window. Such events, which have a positive TPA value, are subtracted from the trigger efficiency as they are considered as test pulses.

Survival Probability

A similar procedure is adopted to obtain the survival probability. For this purpose, the same reference set of *simulated data* of the trigger efficiency is used. The *survived events* are then obtained by applying the data selection steps to the *triggered events*. Additionally, simulated events where the simulated amplitude and the one reconstructed by the filter differ by more than three times the baseline resolution are removed. The scope of this additional requirement is to discard simulated events below threshold that coincided with strong upward fluctuations of the noise in order to avoid

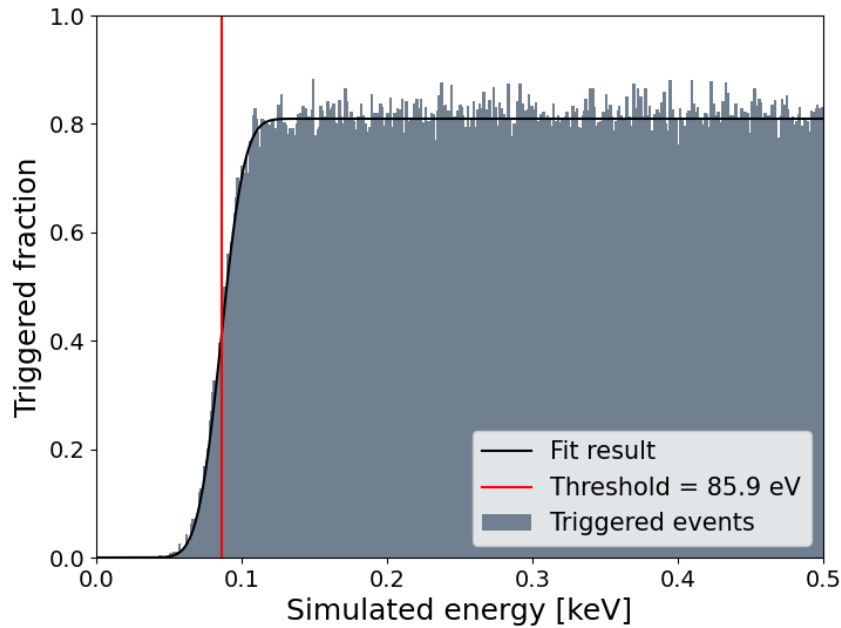


Figure 4.16: Trigger efficiency with respect to simulated energy in the energy region close to threshold. In black the fit result of equation 4.11 is presented. This fit yields an energy threshold of 85.9 eV.

an over estimation of the survival probability. In figure 4.17 the survival probability (red) can be seen compared to the trigger efficiency (gray). The distribution over energy is constant for energies well above threshold, with a plateau around 68% in this case. This shows how the analysis cuts remove around 10% of events in addition to the trigger efficiency over the whole energy spectrum above threshold.

4.3 High Level Analysis

Once the final energy spectrum and the survival probability are obtained, these objects can be used to perform a dark matter analysis. If the shape of the measured energy spectrum is compatible with a DM signal (as described in section 2.1), a **positive analysis** is performed. In such a case, the statistical significance of the signal is calculated and the dark matter mass and the interaction cross-section of dark matter particles with nucleons are evaluated. Otherwise, **exclusion limits** for the aforementioned parameters can be set.

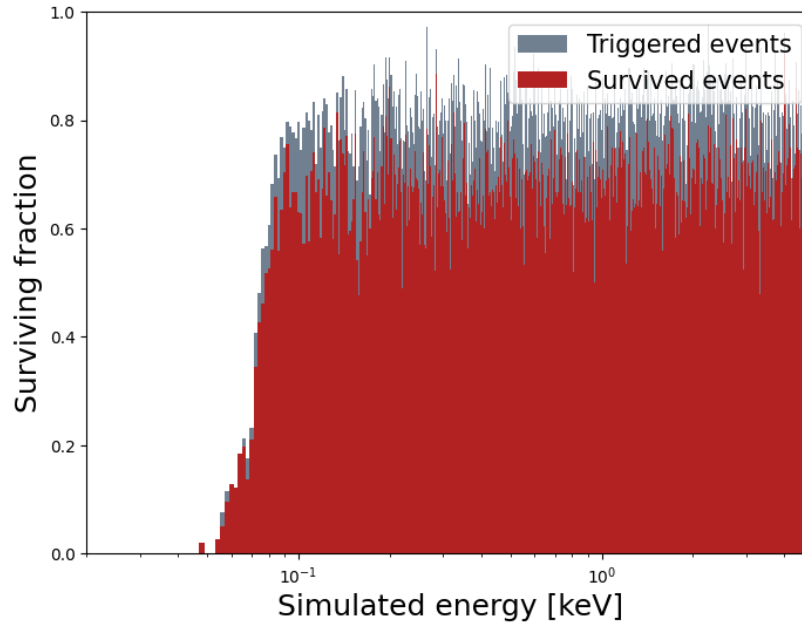


Figure 4.17: Trigger efficiency (gray) and survival probability (red) as a function of the simulated energy.

4.3.1 Definition of ROI

Bands Definition

Once all the steps of the low level analysis have been performed for both the phonon and the light channel, their output can be combined to calculate the light yield (LY). The LY can then be used to discriminate nuclear recoil events from events originating from e^-/γ particles. The region of the LY plot where nuclear recoils are expected is defined on a separate data set recorded with a **neutron source** (AmBe). Thanks to the numerous events generated by the impinging neutrons, it is possible to calculate the quenching factors of the nuclear recoil bands. A detailed description of the recoil bands can be found in [72]. This analytical description is used to fit the neutron calibration data and define the separate regions of the LY plot. The fit result for the example of a CaWO_4 target can be seen in figure 4.18 (left), where the blue band defines the region of e^-/γ events, and red and green delimit the regions where nuclear recoils of two different elements are expected.

Definition of Region of Interest

After the band calculation, the region of interest (ROI) can be defined. This is the region of the LY plot that will be used for the limit calculation. In this region, only the nuclear recoil bands are accepted. Since in many cases the e^-/γ band shows an overlap with the nuclear recoil bands, parts of the nuclear recoil bands are removed as well to minimize the electromagnetic background. The consequent loss of expected signal is accounted for in the limit calculation. The definition of the ROI is visualized

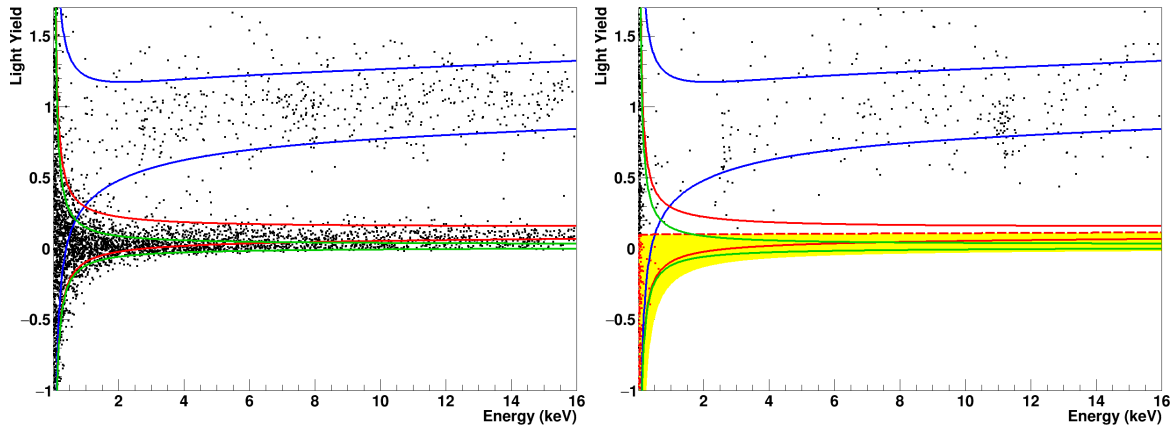


Figure 4.18: *Left:* Light yield plot of the neutron calibration data. *Right:* Light yield plot of a data set for a dark matter search. In both plots the blue bands define the region where electromagnetic background is expected, while the green and red bands represent the region where nuclear recoils off oxygen or tungsten are expected. The yellow area in the right plot represents the ROI used for the limit calculation. Figure taken from [48].

as the yellow area in figure 4.18 (right).

4.3.2 Exclusion Limits Calculation

The CRESST exclusion limits presented in this work are all calculated with the Yellin Optimum Interval Method [77] and with a confidence level of 90%. For the exclusion limit calculation, a DM mass range has to be defined. The lower mass limit is defined by calculating which m_χ would lead to a maximal recoil energy (see equation 2.3) just above the detector energy threshold. The upper bound is naturally set by the maximal reconstructed energy. However, CRESST is an experiment optimized for low mass sensitivity, therefore the limits are typically calculated only up to a DM mass of $10 \text{ GeV}/c^2$. This mass range is then subdivided into a selected number of mass points, for which the lowest cross-section is calculated that can be excluded with a 90% confidence level. Each calculated m_χ - σ point is then interpolated to define the final exclusion limit.

The lowest cross-section that can be excluded with a certain confidence level is calculated with a method elaborated by Yellin aiming at evaluating exclusion limits for data sets that include unknown backgrounds. A particular aspect of this method is that every event is treated as a potential signal event. Therefore, in cases of data sets with well understood backgrounds, the Yellin method might lead to too conservative exclusion limits. In such cases, other methods, like the likelihood formalism [78], can be employed.

The Yellin method will be summarized in the following, and an accurate description can be found in [77].

Yellin Maximum Gap Method

Since the method is developed to calculate exclusion limits in presence of unknown backgrounds, the basic idea is to extract the sensitivity by the absence of events. To this scope it is necessary to identify the gap with the biggest size x_{max} in the spectrum, where x_i is defined as the integral of the expected spectrum, over the energy range between two consecutive events.

$$x_i(\sigma, m) = \int_{E_i}^{E_{i+1}} \frac{dN(\sigma, m, E)}{dE} dE \quad (4.12)$$

An illustration of this concept can be seen in figure 4.19. The basic principle of this method is to identify for each DM mass value the cross-section σ that would lead to an expected x_i that is incompatible with the observed x_{max} , at a certain confidence level. To define when a cross-section is incompatible, one assumes that the dark matter cross-section truly corresponds to the currently tested one and a set of identical experiments is performed to measure the DM rate. Then, for a cross-section to be incompatible the probability that one of these experiments measures $x < x_{max}$ in the same energy interval must be C_0 . This probability C_0 represents the confidence level of the exclusion limits (typically chosen as 90%) and can be calculated fully analytically, as described in [77]. The process of identifying the cross-section that can be excluded with the confidence level C_0 is then repeated for each DM mass in the mass range of interest.

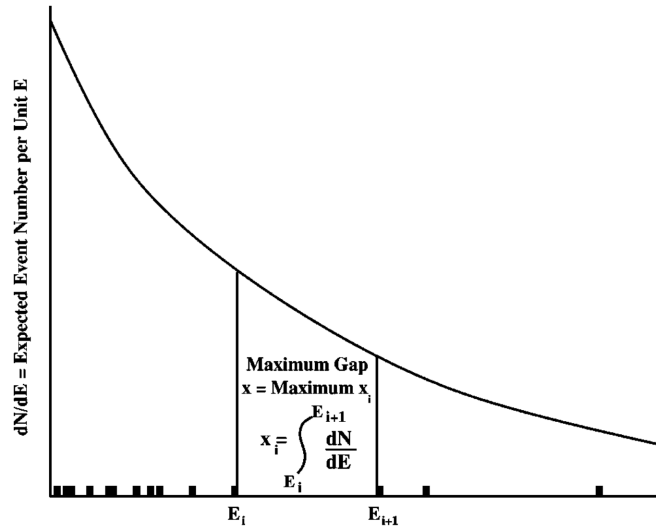


Figure 4.19: Illustration of the Yellin maximum gap method. Picture reproduced from [77].

Yellin Optimum Interval Method

The maximum gap method is mostly appropriate for data sets with a low density of events. For data sets with a high density of events, an extension of it can be used:

the *optimum interval method*. This is the method used for the limit calculation in CRESST, due to the relatively high density of events. In this case, the approach is very similar to the maximum gap method, with the difference that for the measured data, x does not represent an empty gap but contains n events.

For each tested cross-section, the probability C_n is calculated by scanning each possible energy interval containing n events. The process is repeated for different values of n . In contrast to the maximum gap method, where C_0 can be calculated analytically, for the optimum interval method the probability C_n is tabulated with a Monte Carlo program. Considering all the scanned intervals, the *optimum interval* is the one that gives the maximal C (C_{max}). Once this interval is identified, the lowest incompatible cross-section is identified with a criterion similar to the maximum gap method: the σ whose C_{max} is higher than the one expected by 90% of identical dark matter experiments is excluded.

Chapter 5

Lithium-Based Detectors

The results presented in this chapter have been published in the paper "Testing spin-dependent dark matter interactions with lithium aluminate targets in CRESST-III" [79] included in appendix A, of which I am a corresponding author, together with Dr. Shubham Gupta and Dr. Felix Wagner. In this paper, the results obtained with two lithium aluminate modules, referred to as Li1 and Li2, measured in Run36 of the CRESST experiment, are presented. I have performed the analysis on the training set of the Li1 module and on the training set and blind data set of the Li2 module. In the paper, the focus is on the results obtained with the Li1 module, as they set more stringent exclusion limits on the spin-dependent elastic DM-nucleon cross-section than the ones of Li2. The results of the Li2 module have been included as a control measurement. In this work, the focus will be instead on the original results of Li2.

Lithium is an element well-suited for low-mass dark matter searches, thanks to its light nucleus ($A=7$). To the CRESST experiment it is particularly interesting, as it is the lightest element that can be embedded in a crystalline lattice and therefore can be employed with the CRESST technology. Additionally, with a nuclear ground state angular momentum different from zero $J_N \neq 0$, lithium can be also used to probe spin-dependent (SD) DM-nucleon interactions. Among other light elements typically used within SD searches, lithium stands out with its high $X_{p/n}$ values that ensure high expected DM-nucleon scattering rates (see section 2.1.4). These values and the natural abundance of lithium isotopes can be seen in table 5.1, compared to other elements commonly used for SD searches.

Besides ${}^7\text{Li}$ with a natural abundance of 92.41%, ${}^6\text{Li}$ occurs with a natural abundance of 7.49% [80]. This second isotope, provides a third interesting advantage for using lithium in dark matter searches. Since it undergoes the neutron capture reaction



it is possible to use ${}^6\text{Li}$ as a neutron flux monitor, by identifying the 4.78 MeV line [81]. However, it is important to notice that this reaction is also a source of tritium that represents an intrinsic background of lithium-based crystals.

Various lithium-based crystals are known: e.g. Li_2MoO_4 , $\text{Li}_2\text{Mg}_2(\text{MoO}_4)_3$, Li_2WO_4 ,

LiF or LiAlO₂. Out of these, the CRESST collaboration has tested Li₂MoO₄, LiAlO₂ and LiF. The first measurements, done for detector characterization purposes, will be presented in the first section. LiAlO₂ has then been adopted for Run36 (see section 3.3). In section 2, the analysis of one of these detectors will be presented. The final dark matter results, in the form of exclusion limits on the SD elastic DM-nucleon interaction, will be discussed in section 3. Finally, conclusions on this measurement will be drawn in section 4.

	J_N	$\langle S_p \rangle$	$\langle S_n \rangle$	$X_p = \frac{J+1}{J} \langle \mathbf{S}_p \rangle^2$	$X_n = \frac{J+1}{J} \langle \mathbf{S}_n \rangle^2$	nat. ab.
⁶ Li	1	0.472 [82]	0.472 [82]	0.446	0.446	7.49%
⁷ Li	3/2	0.497 [83]	0.0040 [83]	0.412	~ 0	92.41%
⁹ Be	3/2	0.007 [84]	0.415 [84]	~ 0	0.287	100%
¹⁷ O	5/2	0 [83]	0.5 [83]	0	0.35	0.0367%
¹⁹ F	1/2	0.441 [83]	0.109 [83]	0.583	0.036	100%
²⁷ Al	5/2	0.343 [85]	0.0296 [85]	0.165	0.001	100%
²⁹ Si	1/2	-0.002 [84]	0.13 [84]	~ 0	0.051	4.6%

Table 5.1: A selection of isotopes with $J_N \neq 0$ commonly used for spin-dependent searches with their relative J_N , $\langle S_{p/n} \rangle$ and $X_{p/n}$ values and natural abundances. The $X_{p/n}$ values can be used to compare which isotope leads to the highest expected rates of SD DM-nucleon interaction.

5.1 Tested Lithium-Based Crystals

To fully exploit the potential of the CRESST technology, one should employ a scintillating lithium-based crystal, which allows for the application of the phonon-light technique. The CRESST collaboration has already tested three lithium-based scintillating crystals, which will be presented in the following. It is noteworthy that not all measurements were aimed at detecting SD interactions of light DM. The neutron monitoring is, in fact, also a very interesting aspect for the CRESST experiment. When employed as detectors, lithium-based crystals can be used to monitor the neutron flux inside the experimental set-up. Unfortunately, a light dark matter search and neutron monitoring cannot be easily performed with the same detector. The light dark matter search requires a low energy threshold, while the neutron monitoring requires the reconstruction of energies up to 4.78 MeV. The simultaneous fulfillment of these two requirements is very challenging with the CRESST technology. Transition edge sensors (described in section 3.1.2) can lead to very low energy thresholds. However, when optimized to maximize the sensitivity, they have a limited dynamic range, which in CRESST measurements usually ends at energies well below the capture peak.

5.1.1 Lithium Molybdate

The first lithium-based crystal the CRESST collaboration has tested is lithium molybdate (Li₂MoO₄). This test has been performed in the above-ground facility of the

Max-Planck-Institut für Physik, as described in [86]. The advantage of this material is the high intrinsic radio-purity that can be obtained with a dedicated production. One drawback, however, is its solubility in water. The methods used to apply sensors directly on the crystal surface cannot include wet processes, which are foreseen in the standard production of CRESST sensors. Given this limitation, this first measurement was performed using an NTD Neutron Transmutation Doped (NTD) that can be glued on the absorber, and thanks to its large dynamic range ensured the reconstruction of the capture line (for more details on the working principle, see e.g. [87]). Besides the demonstration of the possible neutron monitoring with lithium molybdate, an exclusion limit on the spin-dependent DM-nucleon cross-section has been calculated.

The spectrum used to calculate such limits covered the energy range 0.932 keV-50 keV. The resulting exclusion limits can be seen in figure 5.1. It can be noticed, how despite the high threshold of 0.932 keV, the light lithium nucleus allowed for a better sensitivity to low DM masses in the proton-only case, compared to experiments using e.g. ^{73}Ge , used by the EDELWEISS and CDMSlite experiment. This proved the advantage of using lithium-based crystals for SD searches, motivating the search for a crystal configuration that allows for a direct application of the TES on the crystal.

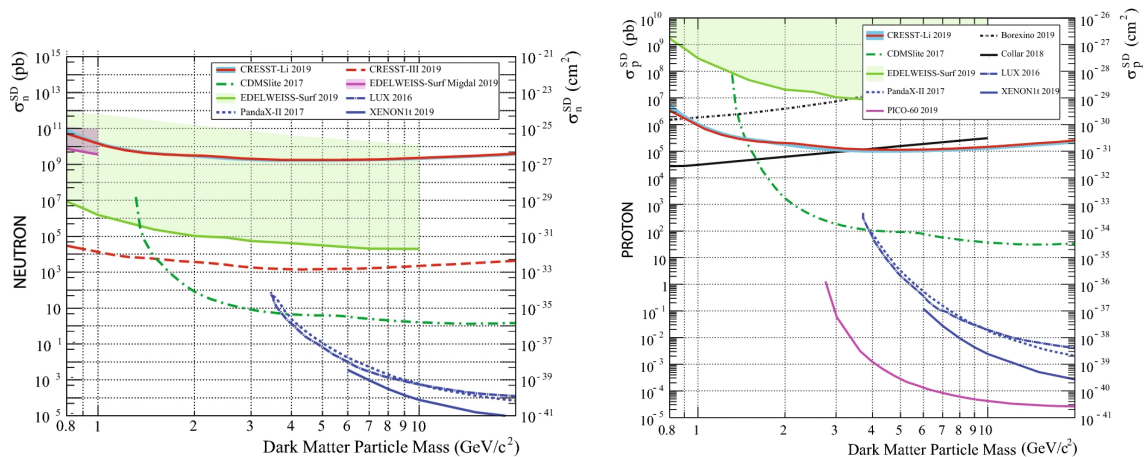


Figure 5.1: Upper limit on elastic scattering SD DM-nucleon cross-section for the neutron-only (left) and proton-only (right) case at 90% CL. The red dashed line shows the exclusion limits obtained with a lithium molybdate crystal. Figure reproduced from [86]

5.1.2 Lithium Aluminate

A lithium-based crystal on which a TES can be directly evaporated, is lithium aluminate (LiAlO_2). Besides the direct application of the sensor, there are other advantages of using this material. Firstly, LiAlO_2 is a scintillator that emits light with a wavelength of about 300 nm, which can be collected efficiently by the silicon-on-sapphire light detectors of CRESST. Secondly, lithium aluminate contains the ^{27}Al isotope that has a nuclear spin factor of $J=5/2$. This isotope further enhances the

sensitivity to SD interaction, both for the proton-only and for the neutron-only case. The LiAlO_2 crystal has been tested in the above-ground facility of the *Max-Planck-Institut für Physik*, as described in [88]. With this measurement, a threshold of 0.213 keV could be achieved, which is a factor 4 better than the one obtained with the lithium molybdate. Exclusion limits on the SD elastic DM-nucleon interaction have been calculated for the exposure of ^{27}Al and ^7Li . The isotope ^6Li has not been included in the calculation due to the missing $\langle S_{p/n} \rangle$ values in the literature at that time. However, it has been considered (and presented in [66]), once these values became available. The resulting limits can be seen in figure 5.2. The black dashed line shows the exclusion limits calculated with the exposure of ^{27}Al and ^7Li , while the red continuous line also includes the exposure of ^6Li . The $\langle S_{p/n} \rangle$ and the natural abundances of these isotopes are given in table 5.1. Comparing the exclusion limits obtained with the lithium molybdate and the lithium aluminate, one can first see that LiAlO_2 probes lower DM masses, covering masses down to $0.3 \text{ GeV}/c^2$ compared to the $0.8 \text{ GeV}/c^2$ of the molybdate. This effect is due to the lower threshold that could be achieved with the aluminate. Furthermore, it is interesting to compare the lowest cross-section excluded by the molybdate and the aluminate at e.g. $1 \text{ GeV}/c^2$ DM mass. For this comparison, it is better to compare the first lithium aluminate results (without ^6Li) since the lithium molybdate did not include the ^6Li isotope in the calculation either. This comparison shows that the exclusion limit obtained with the aluminate improves by two orders of magnitude for the neutron-only case (10^{10} pb in molybdate and 10^8 pb in aluminate) and by one order of magnitude for the proton-only case (10^6 pb in molybdate and 10^5 pb in aluminate). Partially, this improvement is caused by the longer measuring time of the lithium aluminate measurement (which corresponds to a factor of 2.5 higher exposure). However, mostly it is due to the additional ^{27}Al isotope, which has high $\langle S \rangle$ values, both for the proton and for the neutron case.

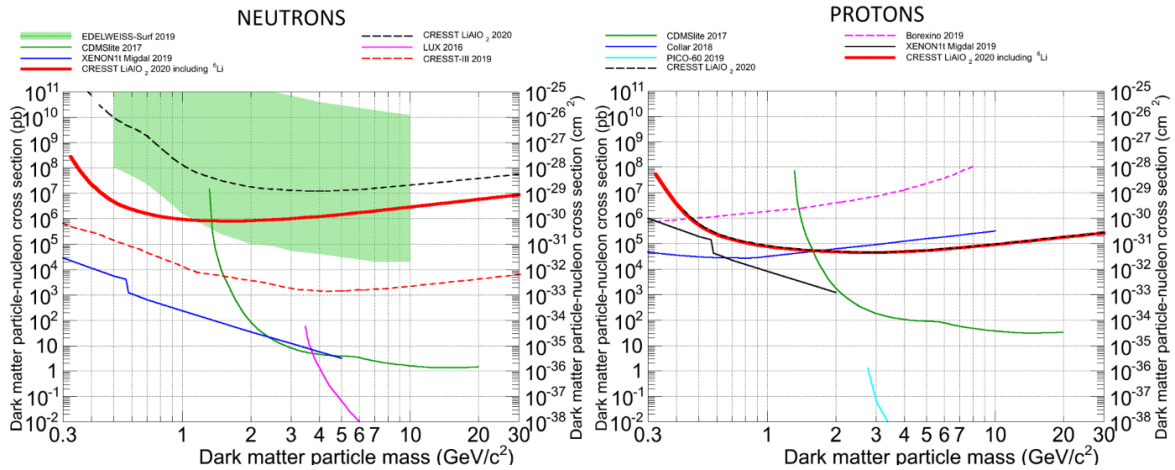


Figure 5.2: Upper limit on elastic scattering SD DM-nucleon cross-section for the neutron-only (left) and proton-only (right) case at 90% CL. The red dashed line shows the exclusion limits obtained with a lithium aluminate crystal. Figure reproduced from [66].

5.1.3 Lithium Fluoride

A lithium fluoride (LiF) crystal has been also tested in an R&D facility of the *Technische Universität München* and presented in [81]. This crystal configuration is particularly advantageous for light dark matter searches as it is formed entirely by light elements: Li ($A=7$) and F ($A=19$). More importantly, it is entirely composed of elements with $J_N \neq 0$, providing high sensitivity to SD interactions. As can be seen in table 5.1, the $\langle S_p \rangle$ value of fluorine is very close to the one of ${}^7\text{Li}$ and the $\langle S_n \rangle$ value is even higher. In contrast to lithium molybdate, this crystal is not soluble in water. However, it has the disadvantage of having a low melting point (870°C) which is not compatible with the high temperatures needed for a direct evaporation of a TES on the crystal surface. Therefore, the sensor needed to be first produced on a small suitable carrier, which was then glued on the lithium molybdate. Since the application of such a carrier significantly reduces the sensitivity to small energy depositions, the energy thresholds achieved with such a composite detector are generally higher than the ones obtained with a direct deposition of the sensor. In this case, a threshold of 300 keV was achieved. The goal of the measurement was to test the feasibility of an in-situ neutron monitoring and an exclusion limit on the SD cross-section has not been calculated.

5.1.4 Choice of the Material

After the test of a lithium molybdate, a lithium aluminate and a lithium fluoride crystal in R&D measurements, the CRESST collaboration decided to employ lithium aluminate crystals in the CRESST underground facility during Run36. Lithium aluminate is in fact the crystal, out of the three tested ones, that best fits the current CRESST technology, allowing to reach low energy thresholds. Thanks to the presence of two nuclei with $J_N \neq 0$, a high sensitivity to SD DM-nucleon interaction is expected with this material.¹

5.2 Analysis of Run36

As explained in section 3.3, Run36 adopts the CRESST-III detector design, which aims at low thresholds to allow for a sub-GeV DM search. In this run, two LiAlO_2 modules were operated, referred to as *Li1* and *Li2*.

5.2.1 Detector Design

The detector design follows the characteristics described in section 3.2.3. Both modules are composed of a phonon detector and a light detector enclosed in a copper housing, where they are kept in position by three copper sticks each. The inner housing is

¹An even higher sensitivity is expected by the LiF crystal which, however, cannot undergo the current sensor production process. For future measurements, a strategy to still adopt this very promising crystal configuration for light dark matter searches, could be to apply a TES directly on the crystal surface, adopting a cold method, e.g. sputtering.

covered with a reflecting and scintillating foil to enhance the light collection and veto events originating on the surfaces of the housing. Inside the detector housing, an ^{55}Fe source is installed for calibration purposes. A picture of the Li2 detector can be seen in figure 5.3. The LiAlO_2 crystals used for the phonon detector were provided by the *Leibniz-Institut für Kristallzüchtung*. Their dimensions are $(2 \times 2 \times 1) \text{cm}^3$, and the weight of each crystal is 10.46g.

The light detector of Li2 could not be operated since the TES did not show a transition. Therefore, the Li2 module worked as a phonon detector only, and no active background discrimination (as described in section 3.2.3) could be performed.

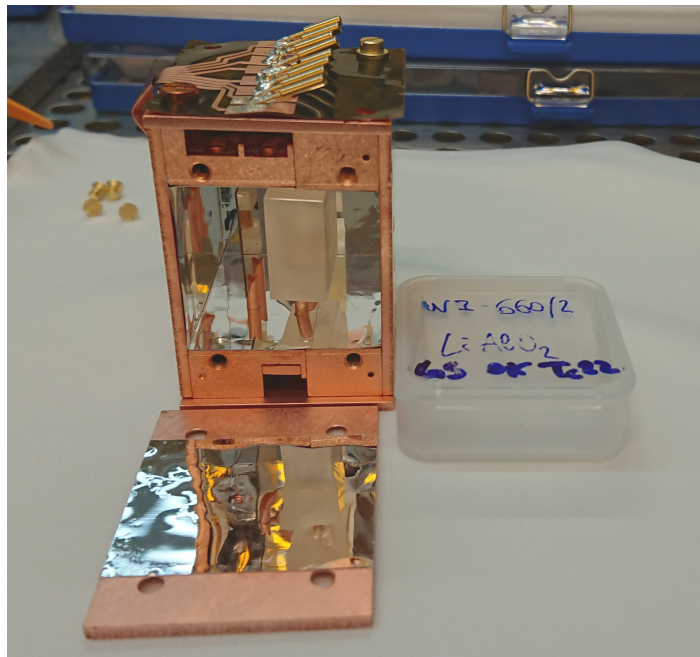


Figure 5.3: Picture of the Li2 module. The LiAlO_2 crystal is kept in position by three copper sticks and enclosed in a copper housing. The internal surface of the copper holder is covered by a reflecting and scintillating foil.

5.2.2 Data Taking and processing

We performed the data-taking with the procedure described in 3.2.6. The continuous stream of data was divided into a training and a blind data set to perform a blind dark matter analysis. The total measuring time of the training set, on which the analysis steps were performed first, was 355 h. The total measuring time of the blind data set was 2716 h. The chosen window size of each event was 655 ms long.

The analysis has been performed with the steps described in chapter 4. In this section, the relevant values relative to each step will be presented.

Creation of the Optimum Filter

First, with a list of clean empty baselines, we created a noise power spectrum (NPS) that represents the noise conditions of the data stream. Afterwards, we created the standard events (SEV) for particles and test pulses. With these two components, we created the optimum filter for particle pulses and for test pulses. The results for particle events can be seen in figure 5.4.

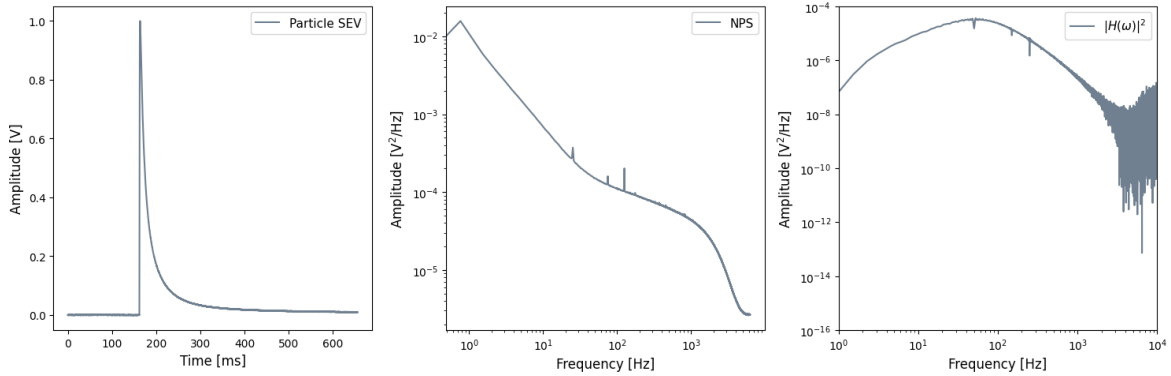


Figure 5.4: From left to right: standard event of a particle event, noise power spectrum, transfer function used for the filter creation.

Baseline Resolution and Threshold Determination

We estimated the baseline resolution with the procedure described in section 4.1.2, obtaining a value of 1.3 mV. The distribution of simulated pulses with fixed amplitude can be seen in figure 5.5.

The threshold has been obtained with the method described in section 4.1.2. The distribution of maxima coincides with a Gaussian distribution, indicating that the baseline presents a white noise distribution. The result of the fit can be seen in figure 5.6 (left). The same figure (right), shows the rate of noise triggers as a function of the trigger threshold. We have chosen to trigger the data at a threshold of 8.9 mV, corresponding to an accepted noise trigger rate of 1 count per kilogram day.

5.2.3 Calibration

We reconstructed the test pulse response (TPR) with the test pulse filter. With this TPR, we created a test pulse equivalent (TPE) of the filter amplitude of particle pulses. We then fitted the region of the TPE distribution containing events caused by the iron source. The mean value of the K_{α} line is obtained at 1.72 injV. With this value, the CPE factor corresponds to:

$$\frac{5.89\text{keV}}{1.72\text{injV}} = 3.42 \frac{\text{keV}}{\text{injV}} \quad (5.2)$$

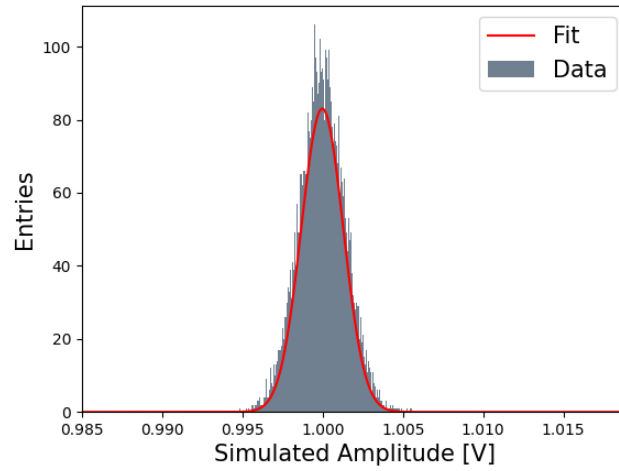


Figure 5.5: Distribution of the filter amplitude for the SEV with fixed amplitude of 1 V simulated on empty baselines. The width of the distribution is 1.3 mV.

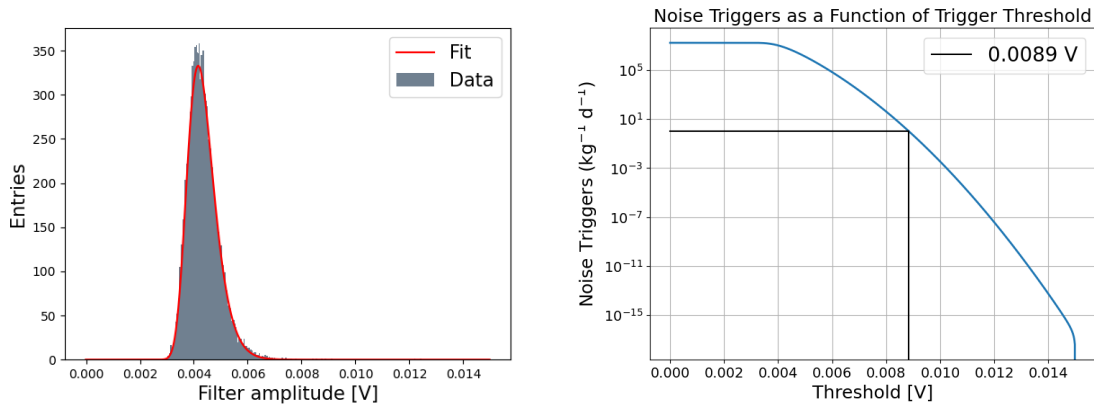


Figure 5.6: Distribution of maxima (left) and noise triggers as a function of the trigger threshold (right).

The calibration factor is then obtained with the amplitude of the lowest TP (0.032 V) that corresponds to a TPA of 0.1 injV.

$$\text{Calibration factor} = 3.42 \frac{\text{keV}}{\text{injV}} \cdot \frac{0.1 \text{ injV}}{0.032 \text{ V}} = 10.6 \frac{\text{keV}}{\text{V}} \quad (5.3)$$

With this factor, the trigger threshold converts to 94.36 eV and the baseline resolution to 13.8 eV.

5.2.4 Data Selection

Stability Cut: We removed from the data events that occurred during periods marked as unstable. Such periods are time slots before and after a control pulse with

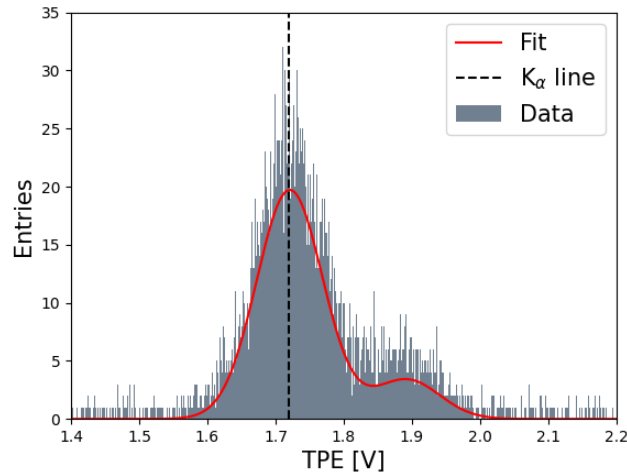


Figure 5.7: TPE distribution of the iron events and the corresponding Gaussian fit in red. The dashed black line shows the position of the K_{α} line, which is used for calibration.

pulse height values more than 3σ away from the mean value.

Rate Cut: We removed events from the data set that occurred in periods recording an excessive trigger rate. The average trigger rate has been calculated as 1 event every 10 minutes. We accepted only events occurring in periods recording up to 5 triggers every 10 minutes.

Quality Cuts: To remove events containing baseline resets or decaying baselines, we applied a cut on the baseline difference. Events containing irregularities in the pre-trigger region were removed with a cut on the baseline RMS. Spikes were discarded with a delta voltage cut. Finally, events with pulse shapes deviating from the SEV were removed with a cut on the filter RMS. The discarded values can be seen in figure 5.8. When considering the triggered particle events occurring in periods marked as stable and with an acceptable trigger rate, quality cuts remove 20.9% of the events.

Coincidence Cuts: We rejected events that are at a time distance of less than 5 ms from an event in the muon panels. This cut removes 4.42% of the total events. This fraction coincides with the probability of expected random coincidences that can be calculated as the following. For a muon trigger rate of 4.52 Hz, the number of expected muon triggers is

$$\lambda = 4.52\text{Hz} \cdot 0.01\text{s} = 0.0452 \quad (5.4)$$

Then the probability of measuring at least one uncorrelated coincidence is

$$P = 1 - \frac{\lambda^k}{k!} e^{-\lambda} \Big|_{k=0} = 1 - e^{-0.0452} = 4.45\% \quad (5.5)$$

Coincidences with other detectors have been tested, but 0 events coinciding with other detectors have been found in the final data set.

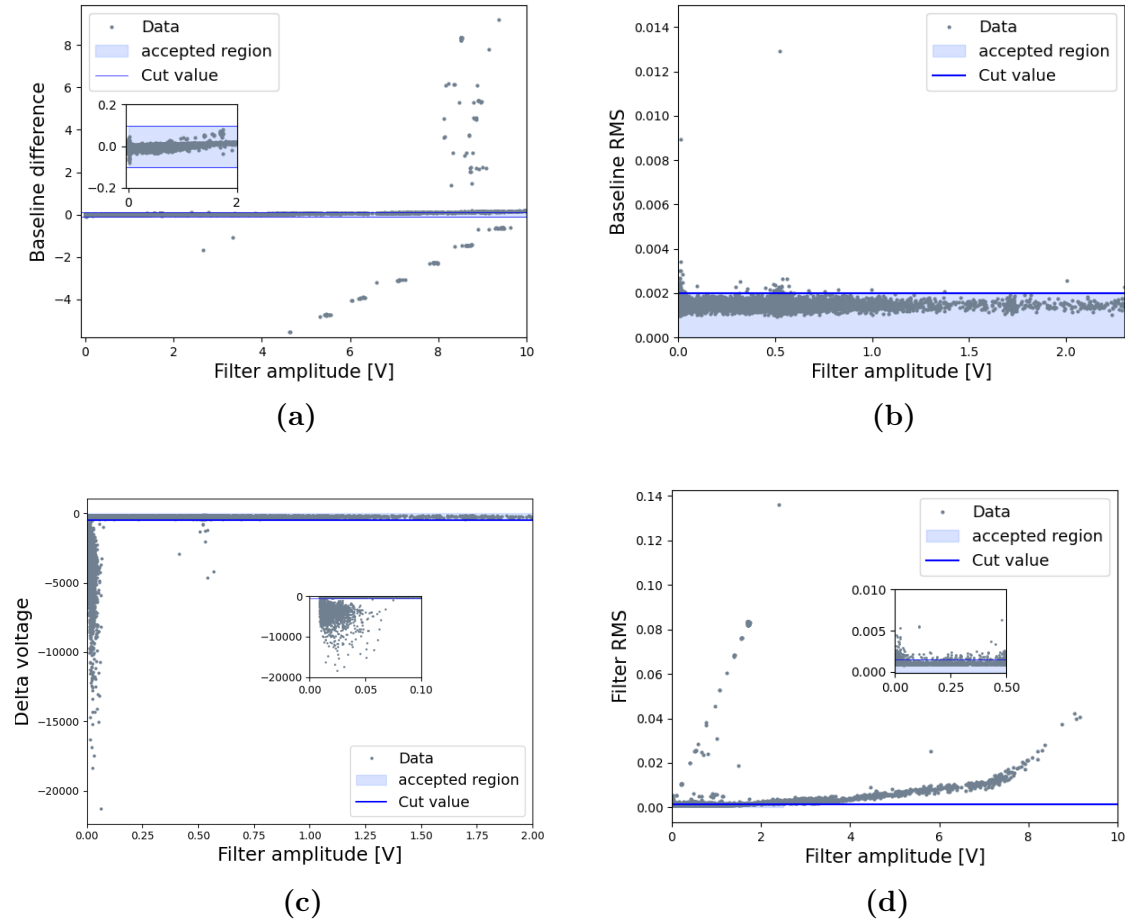


Figure 5.8: Visualization of the quality cuts. The plots show the parameters (a) *baseline difference* (b) *baseline RMS* (c) *delta voltage* and (d) *filter RMS*, each against the filter amplitude. The blue shaded areas show the accepted region and the blue lines the cut values. The cuts are applied in the sequence shown on the data set accepted by the preceding cut. The baseline difference cut in (a) is applied to the data set after stability and rate cut.

5.2.5 Energy Spectrum

After the data selection and calibration, we obtained the energy spectrum that can be seen in the left plot in figure 5.9. This spectrum is characterized by three main features. At low energies, the low energy excess described in section 2.2.4 is recognizable. The energy range between 5.5 keV and 7 keV is dominated by the events of the K_α and K_β lines originating from the ^{55}Fe decay. The rest of the spectrum is filled by a flat, continuous background. This background is expected to be composed of the sources

described in section 3.2.1 and of tritium. Tritium (^3H), is an intrinsic background of lithium aluminate, which originates from the neutron capture of ^6Li (see equation 5.1). For the final limit calculation, we accepted only the energy range from threshold (0.094 keV) to 5.5 keV. Higher energies were not considered because the sensitivity in that energy range would be significantly reduced by the dominating iron events. The spectrum used for the limit calculation can be seen in the right plot of figure 5.9, with a zoomed-in inset showing the low energy excess. In this plot, the spectrum is normalized with the exposure and is corrected with the flat survival probability that is presented in the next section.²

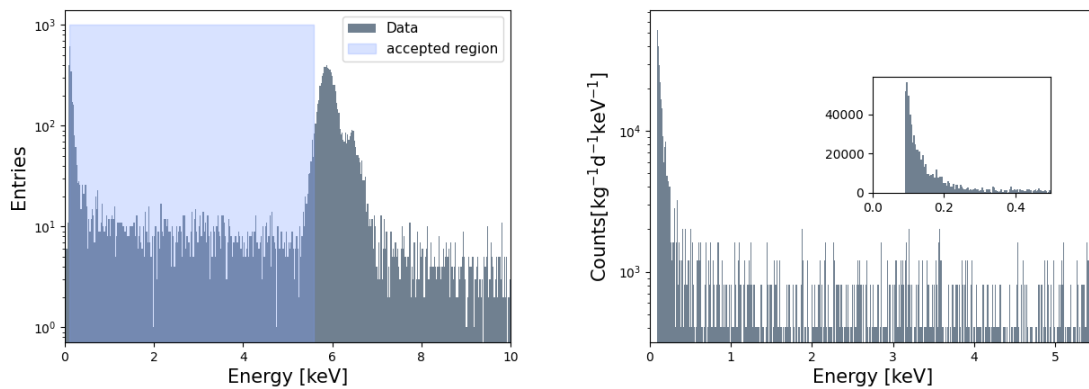


Figure 5.9: Energy spectrum of the Li2 module. *Left:* Complete energy spectrum in the linear range. The blue shaded area highlights the energy range which is finally used for the limit calculation. *Right:* Final energy spectrum used for limit calculation in units $[\text{kg}^{-1}\text{d}^{-1}\text{keV}^{-1}]$. This spectrum has been corrected with a constant survival probability of 70%.

5.2.6 Efficiency Estimation

Once the final energy spectrum was obtained, we estimated the trigger efficiency and survival probability following the procedure described in 4.2.3. For this purpose we simulated 10^6 events distributed randomly on the data stream. The simulated energy range was from 0 to 5.5 keV, to cover the energy range used for the final limit calculation. The trigger efficiency can be seen in figure 5.10 (left) for the limited range from 0 to 0.2 keV. This histogram has been fitted with an error function, obtaining a threshold value of (94.09 ± 0.13) eV, corresponding to the threshold value cited in section 5.2.3, confirming its validity. In the right plot of figure 5.10 the survival probability (red) is plotted over the trigger efficiency (gray) for the energy range 0-5.5 keV. The error function fit of the trigger efficiency (red line, left plot) shows a constant part of the trigger efficiency of 81.26%. As explained in section 4.2.3, this

²This correction is only an approximation in the region close to threshold and is used only for visualization, as the survival probability might be energy dependent.

shows that coincidences with higher pulses or test pulses cause an energy independent reduction of the trigger efficiency of 19%. In addition to that, the data selection cuts lead to a reduction of the survival probability in the region of the plateau by 11%.

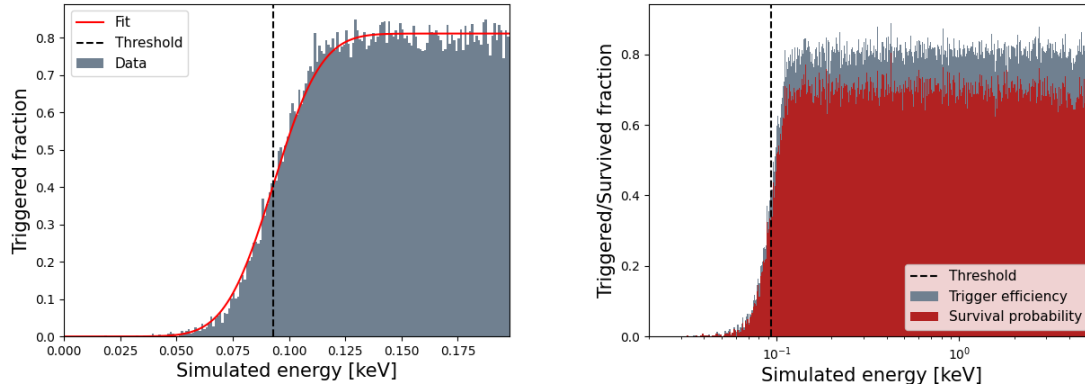


Figure 5.10: *Left:* Trigger efficiency of the Li2 module. The red line shows the error function fit of the efficiency while the black dashed line represents the trigger threshold. The trigger efficiency fit yields a constant part of the trigger efficiency of 81.26% *Right:* Survival probability (red) plotted over the trigger efficiency. The plateau of the survival probability above threshold is around 70%.

5.3 DM Results

5.3.1 Exclusion Limits

We calculated exclusion for the SD elastic DM-nucleon interaction for the Li2 module, following the procedure described in 4.3.2. The total exposure of the blind set of the Li2 module was 1.184 kg days. Only the isotopes ⁷Li, ⁶Li and ²⁷Al have been used for the calculation. The ¹⁷O isotope was not included, for its negligible natural abundance (see table 5.1). The $\langle S_{p/n} \rangle$ values used for the SD cross-section calculation are the ones that can be seen in table 5.1. The exclusion limits were calculated for DM masses from 0.16 to 6 GeV/ c^2 and can be seen on figure 5.11 as a dashed red line. The solid red lines show the exclusion limits calculated with the Li1 module, as published in [79].

5.3.2 Comparison of Li1 and Li2 Modules

It is evident from figure 5.11 that the Li1 module has a higher sensitivity than the Li2 module both for the proton-only and neutron-only cases. This effect is due to the additional scintillation light information provided by the functioning light detector of the Li1 module. Thanks to this detector a population of events originating from the scintillating foil, which covers the inner surface of the housing, could be removed in the Li1 module but not in the Li2. The interaction of particles with the foil can generate

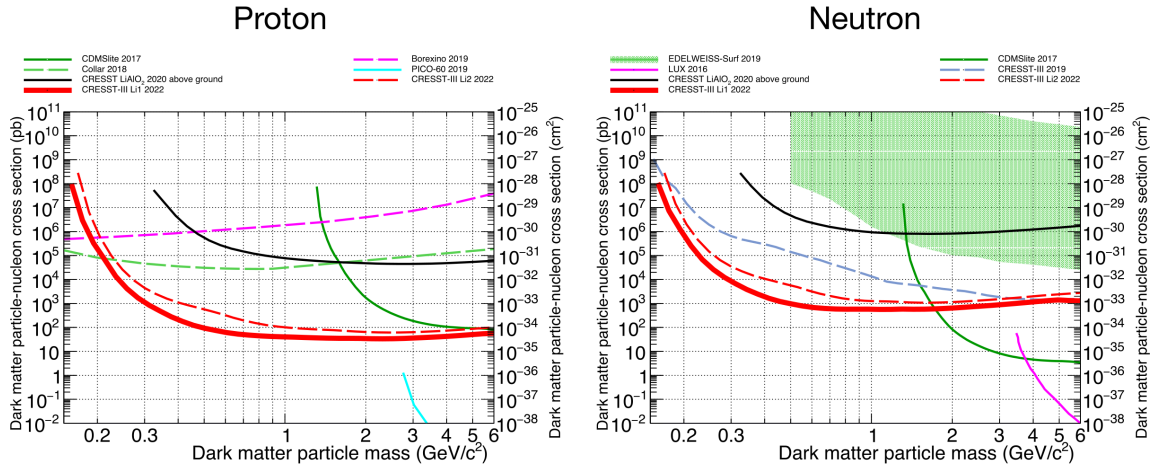


Figure 5.11: Upper limit on elastic scattering SD DM-nucleon cross-section for the proton-only (left) and neutron-only (right) case at 90% CL. The dashed red lines are the exclusion limits calculated with the Li2 module, while the solid red lines are the limits calculated for the Li1 module.

simultaneous hits in the light and phonon detectors. Such events which have phonon energies below 0.2 keV, present a much higher light signal compared to one expected by the scintillation light produced in the crystal and they can therefore be identified and removed (the population is highlighted in red in figure 5.12 - left). In addition to the discrimination of the scintillating foil events, the better sensitivity of the Li1 module is also provided by the possibility to perform a band fit of the light yield (LY) plot, as described in section 3.2.3, that allows to apply LY discrimination removing events in the e^-/γ recoil band. The LY plot for the Li1 module can be seen in figure 5.13: on the left the LY plot for the neutron calibration can be seen which is used to identify different bands. This band definition is then applied to the blind data set, plotted on the right. The final region of interest is shown as a green-shaded area.

5.4 Conclusions

The work presented in this chapter shows the first dark matter results obtained with a lithium-based crystal in the CRESST experimental set-up. We calculated upper limits on the spin-dependent elastic DM-nucleon cross-section. For both modules, these limits represent world-leading exclusion limits (under standard assumptions) in the mass range 0.25 GeV/c^2 to 2.5 GeV/c^2 for the proton-only case and in the mass range of 0.16 GeV/c^2 to 1.5 GeV/c^2 for the neutron only case. For DM masses below 0.6 GeV/c^2 , the sensitivity is significantly limited by the low energy excess.

These results show how lithium-based crystals, in particular in the LiAlO_2 configuration, are excellent for probing spin-dependent interactions at low dark matter masses, firstly thanks to the light nucleus of lithium which is kinematically favored to probe low DM masses, and secondly, thanks to the high $\langle S_{p/n} \rangle$ values of the lithium

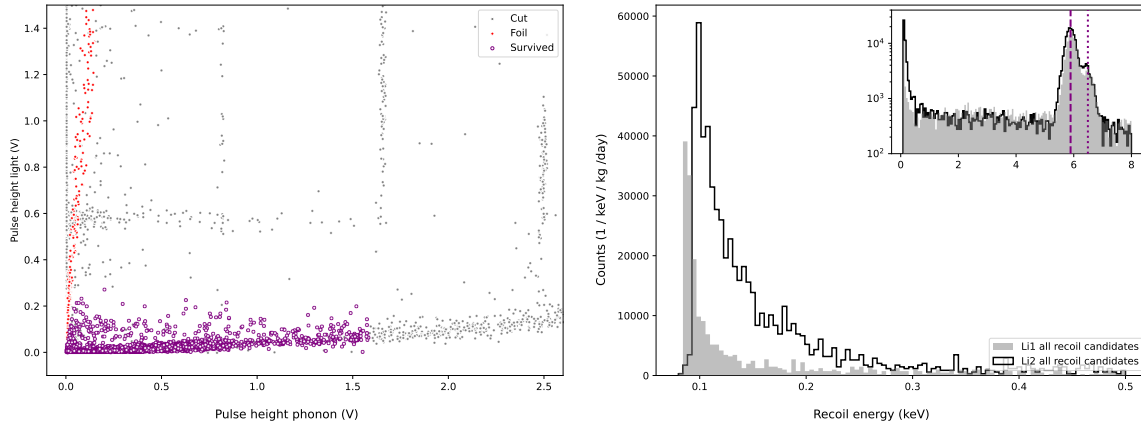


Figure 5.12: *Left:* Pulse height of the light channel versus pulse height of the phonon channel for the Li1 module. In purple are the events accepted in the final data set, in red are events assumed to be originating from the scintillating foil. The calibration factor for this data set is $16.1 \frac{\text{keV}}{\text{V}}$. *Right:* Energy spectra of the Li1 and Li2 modules. Both spectra have been corrected with the flat part of the survival probability. Original plots from [79].

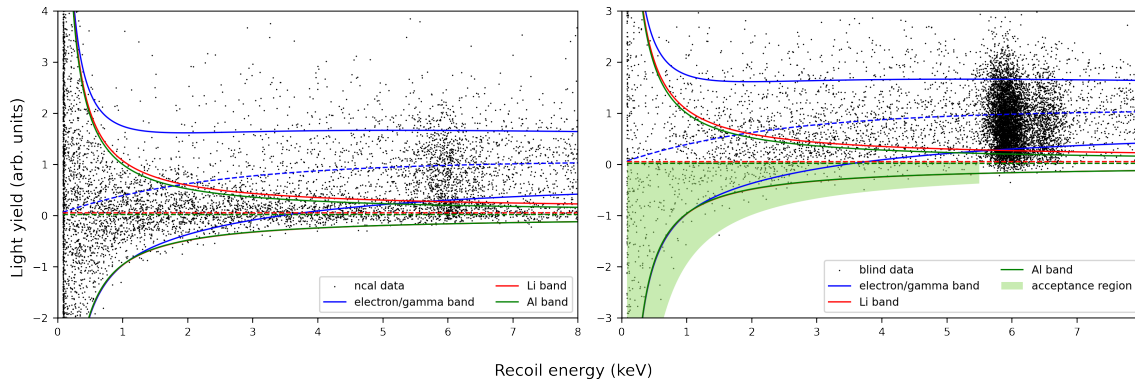


Figure 5.13: Band definition of the Li1 module. *Left:* The LY plot for the neutron calibration. *Right:* The LY plot for the blind data set. Original plots from [79].

and aluminum isotopes with $J_N \neq 0$.

5.5 Outlook

Based on the remarkable results presented in this chapter, lithium-based crystals will be very likely included in future CRESST projects. Nonetheless, some aspects can be improved to increase the sensitivity.

The threshold obtained with already tested materials should be improved. The Li1 and Li2 modules reached thresholds of 83.60 eV and 90.34 eV respectively, but it could be improved, as in the past thresholds down to 30.1 eV have been obtained with crystals of similar sizes. With a lower energy threshold lithium-based crystals can lead the

sensitivity of sub-GeV DM searches, also for the spin-independent case, thanks to the light nucleus of lithium. Moreover, the research on suitable lithium-based crystals can be continued. The focus should be on finding a material that can undergo the TES production process and contain other nuclei (besides lithium) that are light and sensitive to spin-dependent interactions.

Chapter 6

Diamond Detectors

In this chapter I will present the operation of two diamond detectors for which I have performed the analysis. The results presented here, have been published in two separate papers, included in appendix B. I have participated in the writing of "A low-threshold diamond cryogenic detector for sub-GeV dark matter searches" [89] and I am one of the corresponding authors of "Light Dark Matter Search Using a Diamond Cryogenic Detector" [90] together with Dr. Lucia Canonica who started this project with seed money from the Origins cluster. In [89] we presented the measurement of two cryogenic diamond detectors as a proof-of-principle measurement, while in [90] we presented the DM results derived from this measurement.

Recently, diamonds have been proposed for sub-GeV DM searches, as they are expected to probe lower DM masses compared to other commonly used materials [91]. This proposal is highly supported by the improvement in the production of CVD (Chemical Vapor Deposition [92]) crystals that made synthetic diamonds commercially available. One of the arguments for using diamonds in sub-GeV DM searches is that the light carbon nucleus is kinematically favored to probe light masses (see table 6.1 to compare the nuclei of other materials). Moreover, diamonds are expected to reach low energy thresholds when operated as cryogenic calorimeters. The importance of these two aspects for sub-GeV searches has been described in section 2.1

To understand better why diamond detectors would reach a good energy threshold, it is important to notice that the amount of detectable energy in a cryogenic calorimeter operated with the CRESST technology (sensitive to non-thermal phonons) is strongly dependent on the phonon collection. In comparison to other materials, phonon modes in diamonds are more energetic and faster. Therefore, the same energy deposition would create a higher non-thermal phonon signal in diamonds, compared to materials with weaker phonon modes. As a figure of merit of the phonon's properties, one can look at the Debye temperature. As can be seen in table 6.1, in comparison to other materials commonly used as absorbers for cryogenic detectors, the Debye temperature is considerably higher in diamonds.

An additional reason to use diamond as target materials is the excellent isotopic purity of this material. Carbon has two stable isotopes: ^{12}C (abundance 98.9%) and

^{13}C (abundance 1.1%). Thanks to this isotopic purity, diamonds show less isotopic scattering, i.e. scatterings caused by differences in the local potential due to the different masses of the isotopes [91]. Therefore, phonons propagating in diamonds have a longer mean free path than in other materials, translating into a higher probability of reaching the thermometer before thermalization.

Moreover, a long phonon mean free path allows for bigger crystal dimensions, which are crucial when aiming for high exposure experiments. Nonetheless, it is worth mentioning that nowadays the size of synthetic diamonds is still limited, but the progress in the CVD technology allows to expect that crystals in the order of $\sim \text{cm}^3$ could be attainable in the coming years.

In this chapter the measurement of two detectors using diamond as target material will be presented, with which we could show the superior properties of this material, in the form of a low energy threshold and a competitive exclusion limit on the spin-independent DM-nucleon interaction. The experimental setup will be described in section 6.1, while in section 6.2 the detector performance will be discussed. Section 6.3 will present the DM results obtained with this measurement and finally, these results will be summarized in the conclusions.

	Diamond (C)	Si	CaWO₄	Al₂O₃
Mass Number	12	28.1	40,184,16	27,16
Debye temperature [K]	2230 [93]	645 [93]	250 [94]	1000 [95]
Energy gap	5.47	1.11	5.2	8.8

Table 6.1: Relevant values for diamonds compared to other target materials. Values taken from [96] unless otherwise stated.

6.1 Experimental Setup

The diamonds used for this work were produced at AuDiaTec [97] using the Chemical Vapor Deposition (CVD) technique. Specifically, they have been grown using a heteroepitaxial technique on a multi-layer substrate of Ir/YSZ/Si. For this study we employed two single crystal diamonds with the size (2x5x5) mm³ and a mass of 0.175 g each.

6.1.1 Detector Design

To operate the two diamond crystals we adopted the holder structure that can be seen in figure 6.1. The main part of the holder was a copper structure. The crystals were fixed using four sapphire balls as a spacer, to minimize the thermal contact between the crystal and the holder. To hold the targets in position, we used two bronze clamps. The iron (^{55}Fe) sources used for calibration were placed at a distance of about 0.5 cm from each crystal. The holder was closed with a thin copper lid (not in the picture). The design of the TES is the same as the one usually used for the CRESST-III light

detectors to match the small size of the diamond crystals. A picture of the TES with the bond wires can be seen in figure 6.2.

The measurement was performed at the *Max-Planck-Institut für Physik* in Munich. In this facility, the cryostat (a Kelvinox-400HA dilution refrigerator from Oxford Instruments) is located above-ground and it is not equipped with a radiation shielding. Therefore, a high event rate is expected. The temperature control system and the read-out circuit are analogous to the ones used in the CRESST experiment, described in section 3.2.

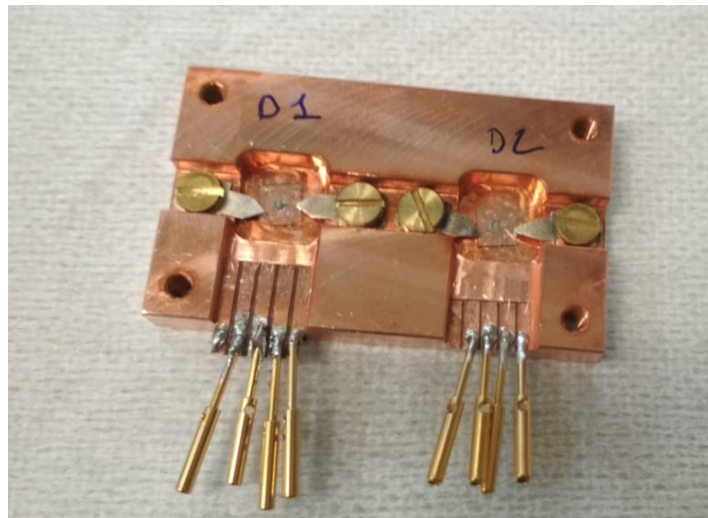


Figure 6.1: Holder of detectors 1 and 2. In this picture, one can see the copper structure holding the two transparent diamond crystals. Both crystals are held in position by two bronze clamps each. On the bottom, four pins are used to connect the heater and bias to the wiring in the cryostat.

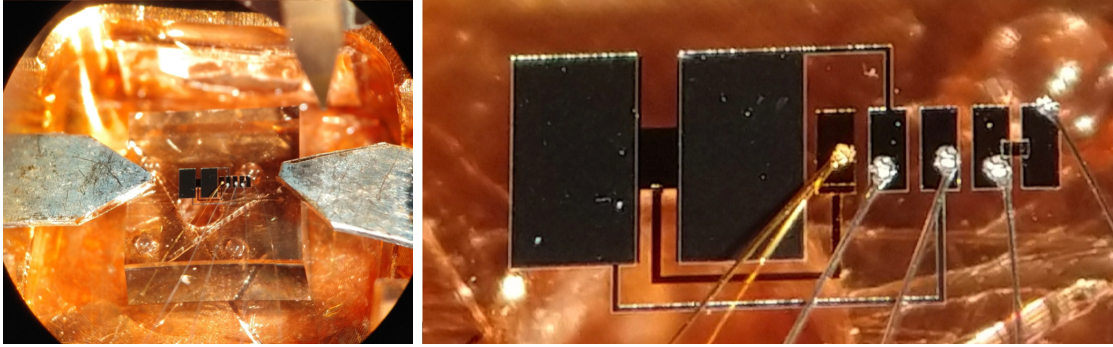


Figure 6.2: *Left:* One of the two diamond crystals instrumented with the TES and housed in the copper structure as seen under microscope during wire bonding. *Right:* Picture of the TES sensor fabricated on one of the two diamond crystals. On the left, it is possible to see two large aluminum areas (0.5×1 mm²), used as phonon collectors, evaporated on top of a darker strip of tungsten (140×300) μm^2 . A 50 nm thick and 1.5 mm long strip of gold connects the tungsten layer to a 40 μm thick gold pad, to which we bond a 25 μm gold wire; this gold strip provides a weak thermal coupling to the heat bath at ~ 10 mK. On the right part of the picture, there is the heater: this is made of a 50 nm thick strip of gold, with two aluminum pads deposited on top for electrical contact.

6.1.2 Data Taking and Processing

After the TES of both detectors showed a transition at around 25 mK, the operating points of the two detectors were optimized, i.e. the combination of heater and bias current that generated the best signal to noise ratio was found. Using an external pair of coils outside the cryostat, a magnetic field was applied to the detectors, since it has been demonstrated that a compensation of the Earth's magnetic field can improve the detector performance [98]. Once the optimal conditions were identified, the diamond detectors were operated in a stable operating point for a total of 58.4 h (this data set will be referred to as *DM data set*). In addition to the DM data set, a second measurement in under-performing conditions was also performed for calibration purposes (this data set will be referred to as *calibration data set*). This was necessary, because iron events could not be correctly reconstructed in the DM data set. In diamonds, particle pulses have a very short rise time due to the outstanding phonon propagation combined with the small dimensions of the crystals. As a consequence, the SQUIDs (see section 3.2.4) used in this measurement were not fast enough to follow high energy pulses, including the iron events, which caused a flux quantum loss. To avoid this effect, the magnetic field was turned off, which caused the transition curve to become less steep and the pulses comparably smaller. In this configuration, iron events did not cause frequent flux quantum losses and we could estimate their amplitude and calculate the CPE factor (the conversion factor from incoming energy to injected voltage value). Since the heater conditions were identical in both data sets, we could use the CPE factor obtained to calibrate the DM data set.

The high trigger rate above-ground led to a frequent pile-up probability of particle

events and heater pulses which made the pulse height monitoring of the CP very inefficient. Therefore, the temperature control (as described in section 3.2.5) was turned off during the collection of the DM data set. Consequently, a selection of usable stable periods was done during analysis.

In order to better evaluate the performance of the diamond detectors and reach the lowest possible energy threshold, we took data as a continuous stream. The data processing was performed with the procedure described in section 4.1.

In the following, the data taken with the two samples will be referred to as *data set 1* and *data set 2*, from *detector 1* and *detector 2*, respectively.

6.2 Detector performance

This section shows the detector performance, presenting the energy threshold and the baseline resolution as figures of merit. These results have been published in [89].

6.2.1 Calibration Factor

As a first step of the analysis of these detectors, we determined the baseline resolution and the threshold of the DM data set. To calibrate these values, we needed to analyze the calibration data first to calculate the CPE factor (see section 4.2.2). Afterwards, we could calculate a conversion factor from injected voltage to reconstructed voltage for the DM data set. Combining these two factors we determined the *calibration factor*, which we used to estimate the value of the baseline resolution and the threshold in energy.

As a first step to calculate the CPE factor, we produced the Test Pulse Equivalent (TPE) out of the iron events in the calibration data set. To create this parameter, we estimated the iron amplitude with a standard event fit. This estimation could not be done using the optimum filter, due to the saturation of the iron events. Therefore, we performed a truncated standard event fit, following the procedure described in section 4.1.4. An example of this fit can be seen in figure 6.3, while the resulting distribution of the TPE can be seen in figure 6.4. With the mean values of the K_α line originating from the iron decay, the CPE factors are calculated as:

$$\begin{aligned} \text{CPE}_{\text{Det1}} &= \frac{5.89 \text{ keV}}{0.962 \text{ injV}} = 6.12 \frac{\text{keV}}{\text{injV}} \\ \text{CPE}_{\text{Det2}} &= \frac{5.89 \text{ keV}}{0.872 \text{ injV}} = 6.75 \frac{\text{keV}}{\text{injV}} \end{aligned} \tag{6.1}$$

In order to calibrate the baseline resolution and the energy threshold, we calculated the calibration factor, using the response of the smallest test pulse which is 0.232 V for detector 1 and 0.373 V for detector 2. Both test pulses correspond to a test pulse with an injected voltage of 0.05 V. With these values we calculated the calibration factor as following:

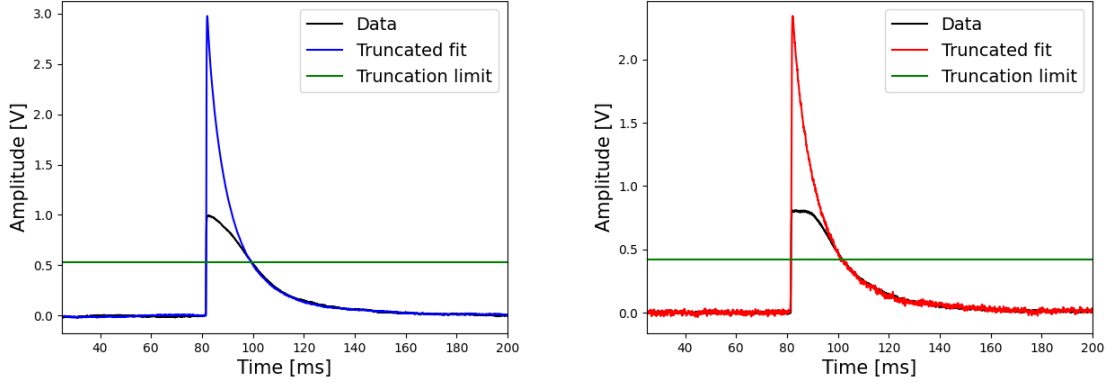


Figure 6.3: Truncated standard event fit of an iron event in the calibration data set for detector 1 (left) and detector 2 (right).

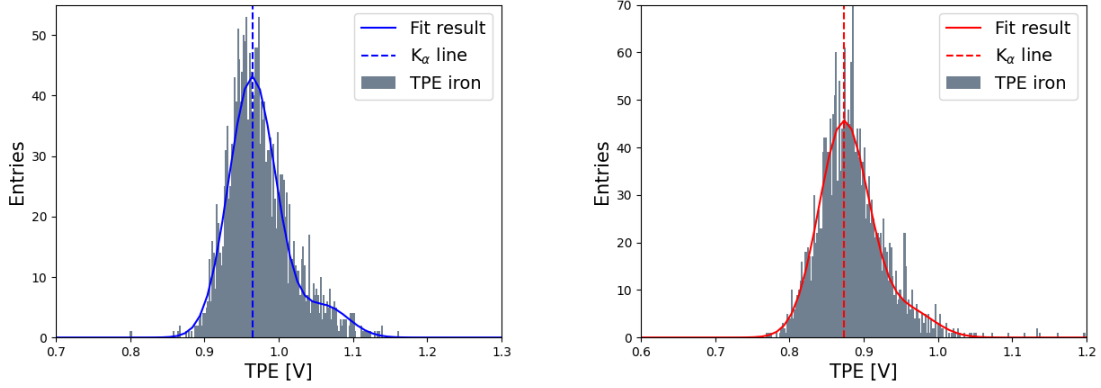


Figure 6.4: TPE distribution of iron hits in the calibration data set for detector 1 (left) and detector 2 (right). In blue (detector 1) and red (detector 2) are the Gaussian fits of the K_α and K_β lines of ^{55}Mn originating from the iron decay. The dashed lines show the position of the K_α line which is used for the calibration.

$$\begin{aligned} \text{Calibration factor}_{\text{Det1}} &= 6.12 \frac{\text{keV}}{\text{injV}} \cdot \frac{0.05 \text{ injV}}{0.232 \text{ V}} = 1.32 \frac{\text{keV}}{\text{V}} \\ \text{Calibration factor}_{\text{Det2}} &= 6.75 \frac{\text{keV}}{\text{injV}} \cdot \frac{0.05 \text{ injV}}{0.373 \text{ V}} = 0.90 \frac{\text{keV}}{\text{V}} \end{aligned} \quad (6.2)$$

6.2.2 Baseline Resolution Estimation

We estimated the baseline resolution with the procedure described in section 4.1.2. To do so, we first created a filter as described in section 4.1.1 for the DM data set. The NPS and the SEV that we used to create it, can be seen in figures 6.5 and 6.6 respectively. For the creation of the SEV, we selected a set of particle pulses contained

in the linear range of the detector, since also in this data set events originating from the iron source were outside the linear regime. The distribution obtained by superimposing the SEV on empty baselines and its Gaussian fit can be seen in figure 6.7. The fitted width is $\sigma_1 = 2.68$ mV and $\sigma_2 = 3.81$ mV. Once calibrated, these values correspond to $\sigma_1 = 3.54$ eV and $\sigma_2 = 3.42$ eV.

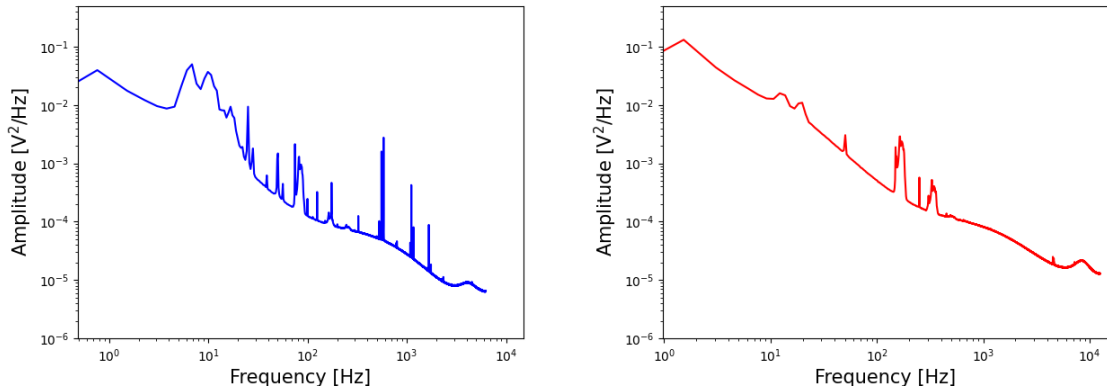


Figure 6.5: NPS of detector 1 (left) and detector 2 (right).

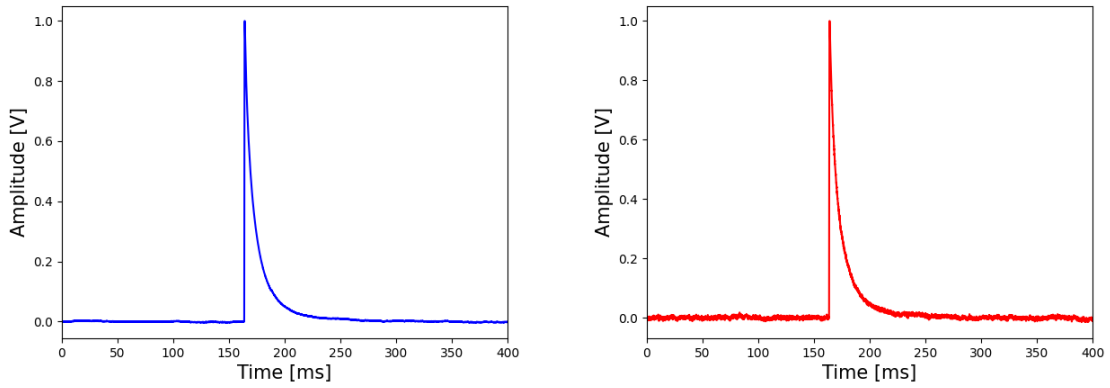


Figure 6.6: Particle SEV of detector 1 (left) and detector 2 (right).

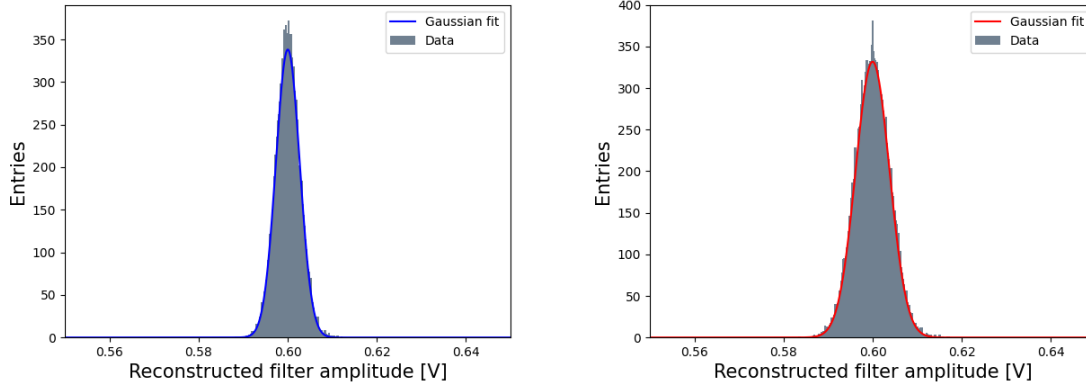


Figure 6.7: Fit of amplitude distribution from a set of empty baseline with superimposed SEV. The fit is used to infer the baseline resolution. The obtained values are 2.68 mV (Det1) and 3.81 (Det2).

6.2.3 Energy Threshold

To estimate the energy threshold we adopted the approach described in section 4.1.2, where the trigger threshold is defined on the base of the number of accepted noise triggers. The distribution of maxima of the empty baselines and its fit with equation 4.5 is illustrated in figure 6.8. Given that the count rate is considerably higher above-ground, compared to the CRESST underground facility, we accepted more than one noise trigger per kg d, adapting the acceptance value to the trigger rate above-ground. To find an appropriate number of accepted noise triggers, we first triggered the data set with a threshold corresponding to five times the baseline resolution. This threshold led to a particle trigger rate of $\mathcal{O}(10^8)$ $\text{kg}^{-1}\text{d}^{-1}$. We therefore accepted a number of noise triggers of $\mathcal{O}(10^6)$ $\text{kg}^{-1}\text{d}^{-1}$ which corresponds to around 1% of the total trigger rate in both detectors. The function of noise triggers depending on the threshold in volts can be seen in figure 6.9. We triggered the data of detector 1 with a threshold of 14.9 mV which corresponds to 19.7 eV, while we triggered detector 2 with a threshold of 18.7 mV which corresponds to 16.8 eV. These thresholds correspond to 5.5 (detector 1) and 4.9 (detector 2) times the baseline resolution. The values of the baseline resolution and the threshold are summarized in table 6.2.

Data set	1	2
Baseline resolution [mV]	2.68	3.81
Baseline resolution [eV]	3.54	3.42
Threshold [mV]	14.9	18.7
Threshold [eV]	19.7	16.8

Table 6.2: Values for threshold and baseline resolution of the two data sets. Each value is shown in mV and in eV. The values in eV have been obtained with the calibration factor of equation 6.2.

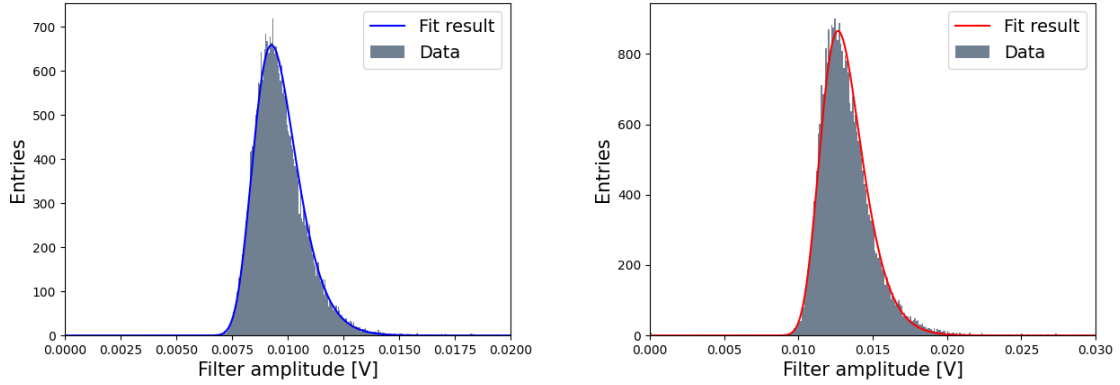


Figure 6.8: Distribution of maxima for detector 1 (left) and for detector 2 (right) with their relative fit.

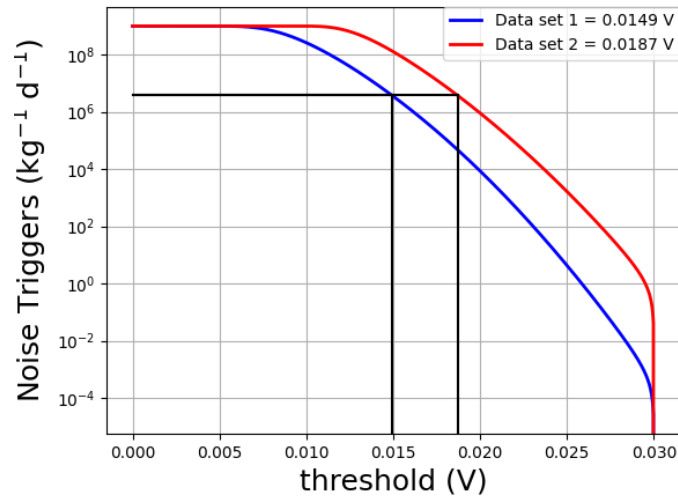


Figure 6.9: Threshold evaluation of the two data sets. The threshold is chosen by accepting a number of noise triggers $\mathcal{O}(10^6) \text{ kg}^{-1}\text{d}^{-1}$ (the choice of this number is motivated in the text). The thresholds that have been obtained are 14.9 mV for data set 1 and 18.7 mV for data set 2. Taking into account the calibration factors, they correspond to 19.7 eV and 16.8 eV respectively.

6.3 Dark Matter results

This section shows the dark matter results that could be obtained with the diamond detectors. These results have been published in [90].

6.3.1 Data Cleaning

After having processed the data with the same procedure described in section 4.2 which resulted in event windows of 655 ms, we started the data selection process.

The most problematic class of events present in the data set was due to the fast rise time of particle events in diamonds (to visualize how fast particle events are in diamonds, see figure 6.10 for a comparison with the same in lithium aluminate). The SQUIDs used

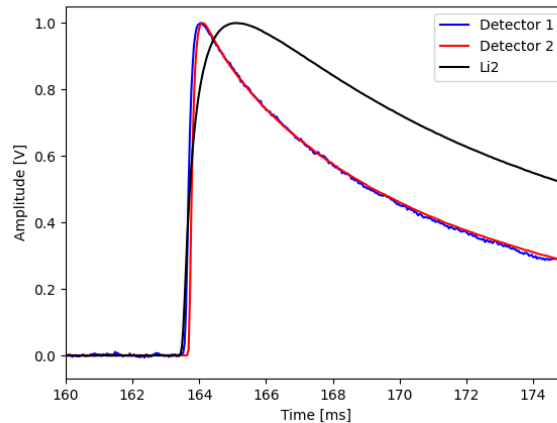


Figure 6.10: Particle SEV comparison between diamonds (red and blue) and in the Li2 module described in chapter 5. Comparing the peak position of the two templates it can be noticed that pulses in the diamond detector have a faster rise time.

in this measurement were not capable of following the fast change in current caused by high energetic events, including iron hits. This led to a loss of flux quanta in the SQUID read-out, resulting in the pulse shape distortion that can be seen in figure 6.11. Most of the high energetic pulses could therefore not be reconstructed correctly, thus we removed them with a *Baseline Difference* cut. The discarded baseline difference values can be seen in figure 6.12.

Compared to an underground measurement, the background rate in this data set was much higher, which led to a higher pile-up probability and more decaying baselines in the data set. We discarded such events using a *BaselineRMS* cut. This cut also discarded some periods with irregularities in the baseline, caused by electronic or mechanical disturbances. The rejected values can be seen in figure 6.13.

Finally, we also applied a cut on the ratio of the filter RMS and the filter amplitude to remove events with a pulse shape that differed from the one of the SEV. This cut was applied on the ratio of these two parameters instead of on the filter RMS itself to prevent energy dependence. The discarded events can be seen in figure 6.14.

The high trigger rate above-ground, makes the temperature control of the detectors (as described in section 3.2.5) very inefficient. Therefore, the control system was turned off during data taking. As a consequence, the operating point was less stable than e.g. for the data set presented in the previous chapter and the stability cut was not applied as presented in section 4.2.1, as it would have consistently reduced the statics

of the measurement. Instead, we accepted only those data periods where the detector response presented only slow fluctuations over time for which a reliable TPR could be calculated. After this stability check, the total usable time reduced to 37.08 h, out of a total data set of 58.4 h.

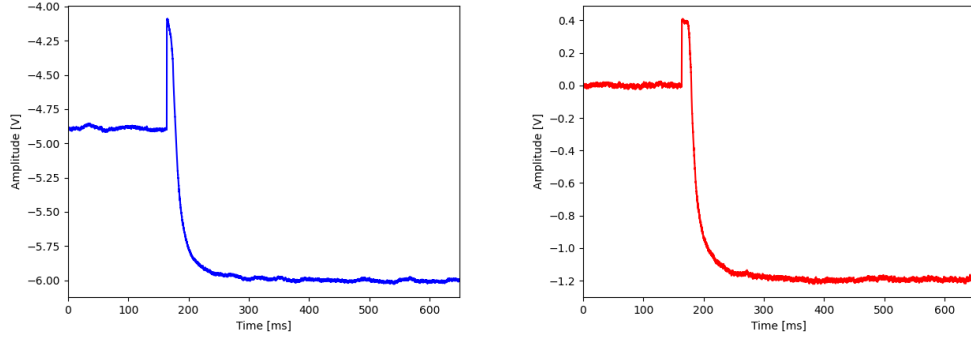


Figure 6.11: An example of baseline change caused by a flux quantum loss in detector 1 (left) and detector 2 (right).

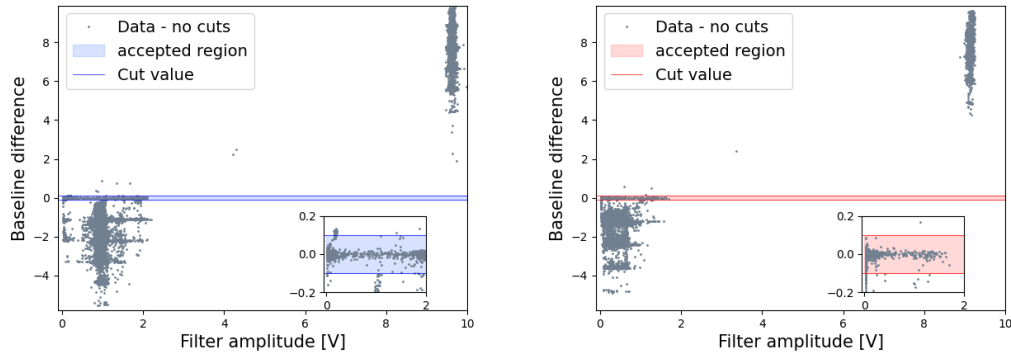


Figure 6.12: Baseline difference parameter distribution for detector 1 (left) and detector 2 (right). The shaded area shows the accepted values, which represent only a small fraction of the total events. On the bottom right one can see a zoom of the accepted region. The data points correspond to the data set of the measurement, after unstable periods were removed.

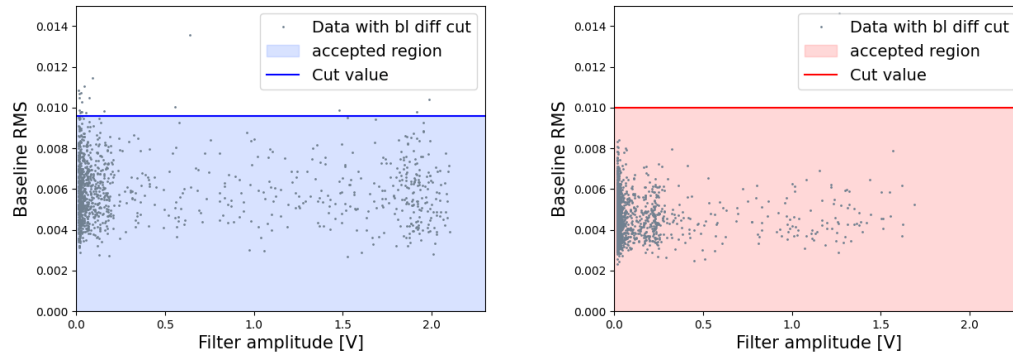


Figure 6.13: Baseline RMS parameter distribution for detector 1 (left) and detector 2 (right). The shaded area shows the accepted values. The data points correspond to the events accepted by the baseline difference cut.

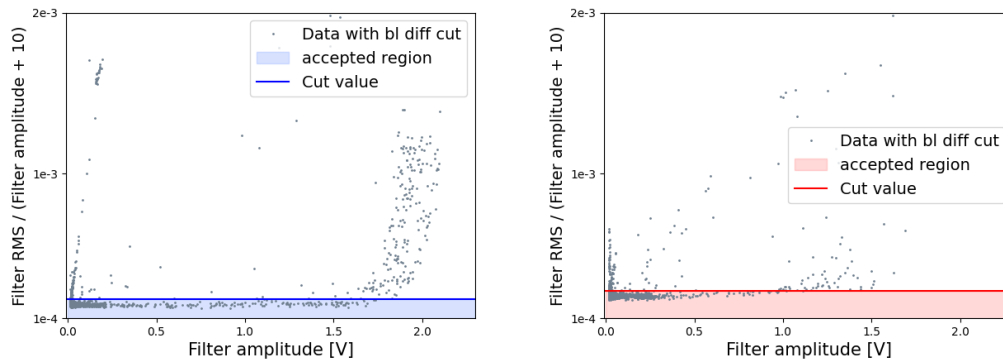


Figure 6.14: Filter RMS over filter amplitude distribution for detector 1 (left) and detector 2 (right). The shaded area shows the accepted values. The data points correspond to the events accepted by the baseline RMS cut.

6.3.2 Data Calibration

We performed the calibration of the DM data set as described in section 4.2.2. While in the calibration data set we used the SEV truncated fit as an amplitude estimator for test pulses and iron events, for the DM data set we used the optimum filter, which provides a better resolution. This was possible because in the DM data set the amplitude estimation was done only for the linear regime of the detector. The values delivered by these two amplitude estimators are equivalent within the linear range, as can be seen in figure 6.15, where the two amplitudes are plotted over time. Following the procedure described in section 4.2.2, we estimated the range of the linear regime: for detector 1 between threshold and 1.1 V, while for detector 2 from threshold up to 0.5 V. The reconstruction of the iron amplitude, which was outside the linear regime, was not necessary since we already calculated the CPE factor with the calibration data set. We therefore created a TPR with the test pulse amplitude obtained with the filter and then created a TPE with the filter amplitude of the clean particle events, using the CPE factors derived in equation 6.1.

Using the calibration factor of equation 6.2, the linear ranges correspond to 19.7 eV - 1.4 keV for detector 1 and 16.8 eV - 0.45 keV for detector 2. The final energy spectra in the respective linear range of the two detectors can be seen in figure 6.16.

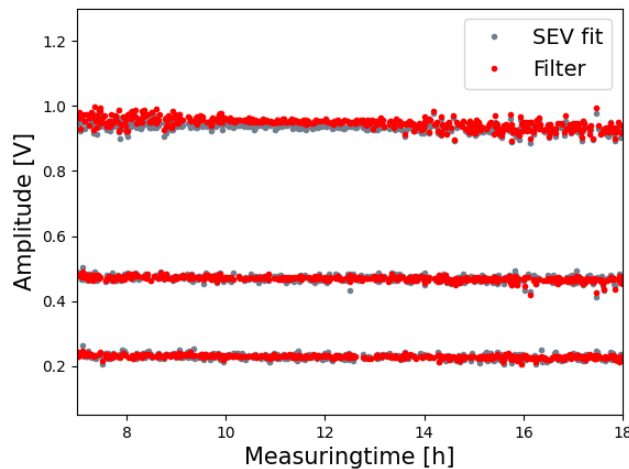


Figure 6.15: Test pulse amplitude estimated with the SEV fit (gray) and with the filter (red) over a limited time range of the data set of detector 1. This plot shows how the two estimations are equivalent within the linear regime (up to 1.1 V for detector 1.)

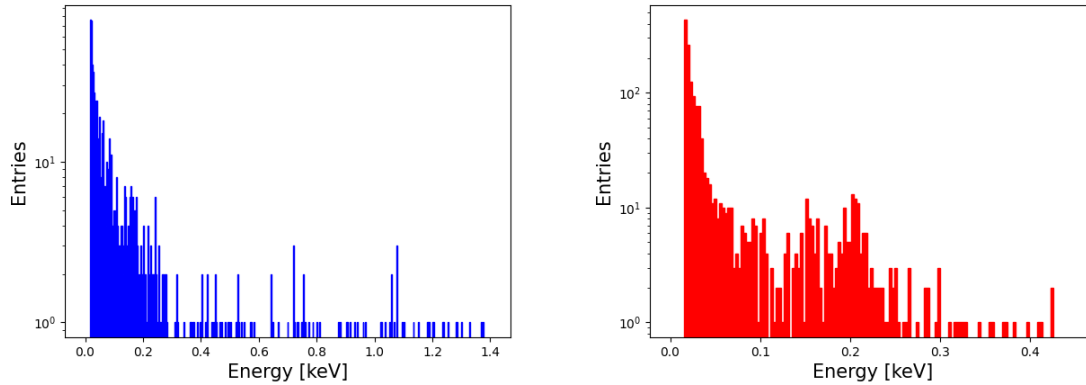


Figure 6.16: Cleaned and calibrated spectrum of detector 1 (left) and detector 2 (right) in their respective linear regime.

6.3.3 Efficiency Estimation

For the estimation of the efficiency of both detectors, we performed a simulation of a flat spectrum in their linear ranges. We then applied the cuts to estimate the trigger efficiency and the survival probability as described in section 4.2.3. The results can be seen in figure 6.17. As expected, at energies above threshold, the survival probability is constant in energy for both modules. The plateau of the survival probability is around 25% for detector 1 and 40% for detector 2. These ratios are very low compared to the ones seen in the underground measurement in chapter 5 ($\sim 80\%$ trigger efficiency and $\sim 70\%$ survival probability). The reason for the low trigger efficiency is a combination of the high total trigger rate, typical in above-ground measurements, and the trigger algorithm. As described in section 4.1.2, if two or more events are present in the same record window, only the one with the highest amplitude is reconstructed at the correct onset and tagged as triggered. This trigger decision causes a strong energy dependence, not equally pronounced in both detectors, as can be seen in figure 6.17. This effect can be understood by looking at the amplitude reconstruction of a flux quantum loss, as seen in figure 6.18. The voltage value of the incorrect amplitude assigned to the pulses is within the linear range of both detectors and therefore affects their trigger efficiency. Good signal events in the proximity of the pulses affected by the flux quantum losses are tagged as triggered only if they exceed their amplitude. Smaller pulses are tagged as not triggered and their amplitude is not estimated (see figure 6.19). As a result, the trigger efficiency with respect to the simulated amplitude (see figure 6.20) has a clear step at the value that corresponds to the incorrect amplitude assigned by the filter to the pulse affected by the flux quantum loss (this step is not extremely sharp, because the exact amplitude assigned by the filter varies slightly with the energy of the interaction). When looking at the trigger efficiency of the simulated energy (figure 6.17 blue), the step is smeared out due to the time dependence of the detector response, meaning that the same amplitude corresponds to a different energy value at different times. This energy dependence is not present in the survival probability, since we

removed events presenting flux quantum losses with the *baseline difference* parameter. The same effect is not visible in typical CRESST measurements, since flux quantum losses are not as frequent as for these diamond detectors. Usually, this effect is caused only by rare high energetic pulses, while due to the short rise time of pulses in diamonds, in this measurement the frequent iron events cause a non-negligible amount of flux quantum losses.

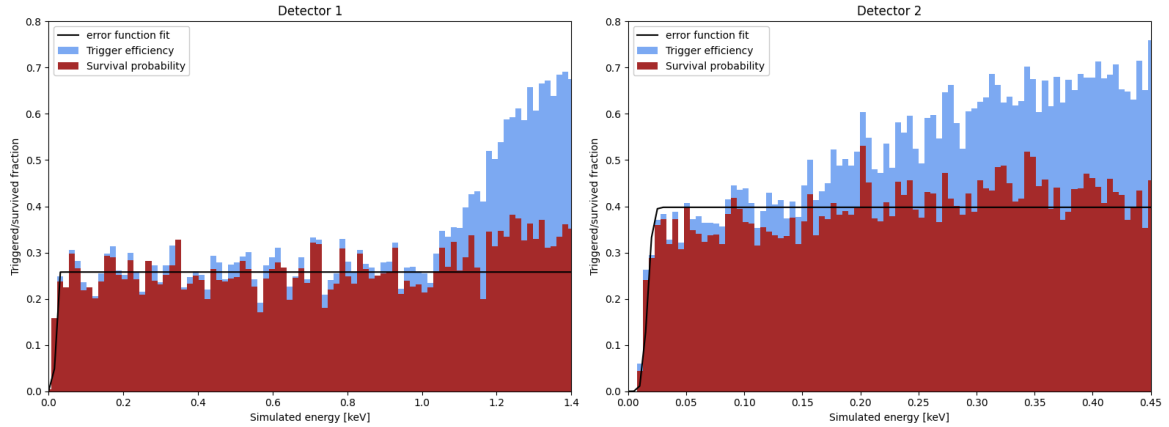


Figure 6.17: Trigger efficiency (blue) and survival probability (brown) of detectors 1 and 2 showing the probability of simulated events surviving the trigger and the quality cuts. The plateau of the survival probability of detector 1 is at $\sim 26\%$ while of detector 2 it is at $\sim 40\%$. Original plot from [90].

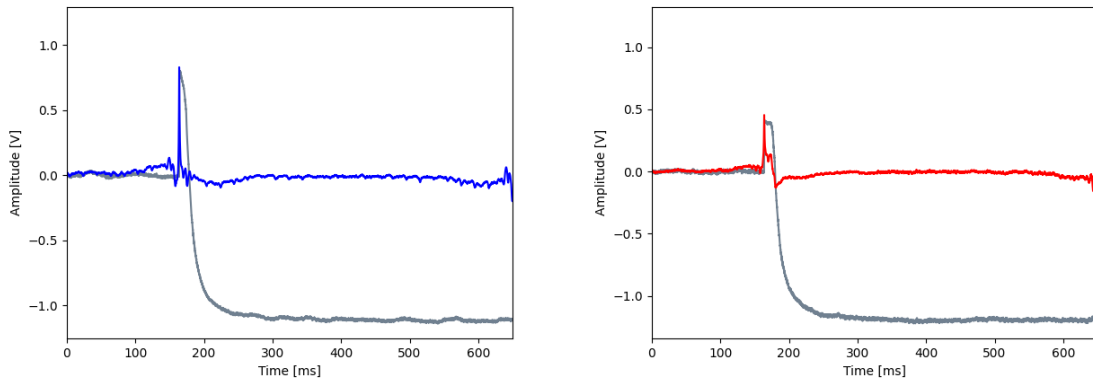


Figure 6.18: Flux quantum loss in raw data (gray) and filter data (blue and red) for detector 1 (left) and detector 2 (right).

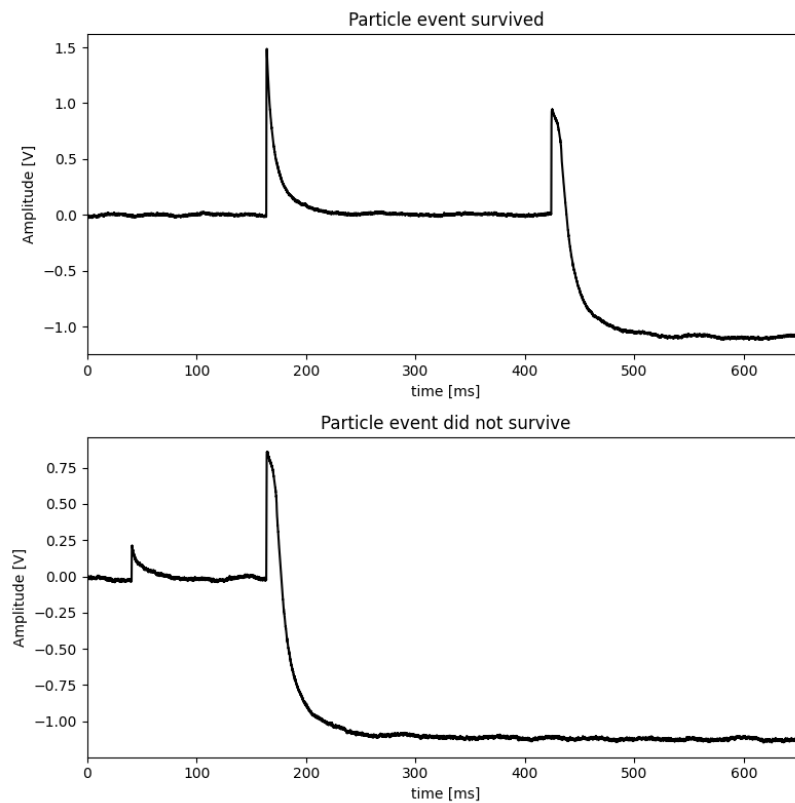


Figure 6.19: Visualization of the baseline change after a high energetic event. In both plots, a simulated signal event is followed by a baseline change caused by an energetic particle. In the upper plot, the simulated event is reconstructed at the correct onset (164 ms) and tagged as triggered because its amplitude is higher than the wrongly reconstructed amplitude, while in the lower plot the reconstructed amplitude is higher and therefore the simulated event is not tagged as triggered.

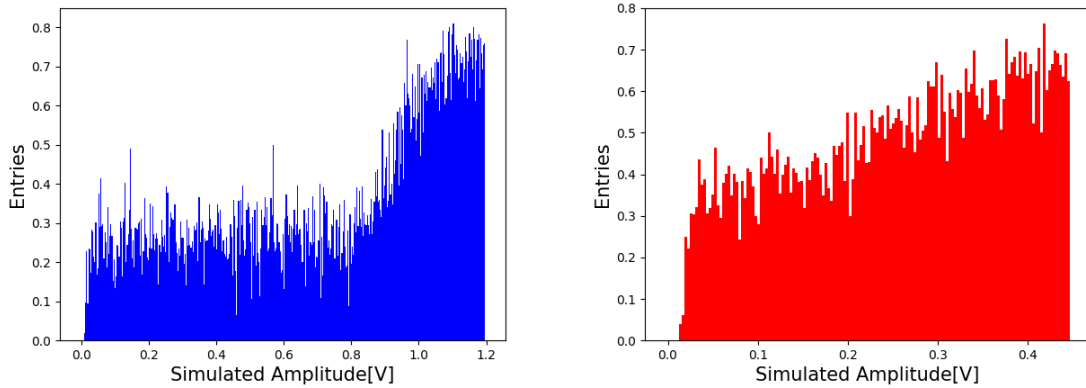


Figure 6.20: Trigger efficiency of detector 1 (left) and detector 2 (right) with respect to the simulated amplitude.

Energy Threshold

We used the trigger efficiency to compare the threshold value with the previously stated trigger threshold value converted into energy with the calibration factor (as described also in section 4.2.3). However, since this measurement had a much lower measuring time compared to the one in chapter 5, we performed an additional simulation in a limited energy range (from 0 keV to 0.1 keV) to enhance the statistics of events close to threshold. Figure 6.21 shows the trigger efficiency up to 0.1 keV, as well as the fitted error function to estimate the threshold. The fit parameters correspond to an energy thresholds of (19.7 ± 5.1) eV for detector 1 and (16.1 ± 4.4) eV for detector 2, which confirm the previously mentioned values of 19.7 eV (detector 1) and 16.8 eV (detector 2).¹

6.3.4 Comparison of Energy Spectra

The energy spectra obtained after the data selection and calibration process are compared in figure 6.22 for detector 1 (blue) and detector 2 (red). The survival probability is used to correct the energy spectra of the two detectors, to allow for a better comparison of the two results. The spectra are shown starting from 30 eV, where both detectors show a flat survival probability, and resolution effects at threshold do not need to be considered. The spectrum of detector 1 is shown only until the end of the linear range of detector 2 for easier comparison.

The two detectors show a comparable event rate and a rise of events in the same energy range. This rise has been observed in other measurements above-ground, though any possible common origin for the excesses above-ground and the LEE described in section 2.2.4, observed underground is still unsure.

¹Despite the additional simulation performed specifically to enhance statistics, this measurement has a lower statistic than the measurement presented in chapter 5 and suffers therefore from a larger error.

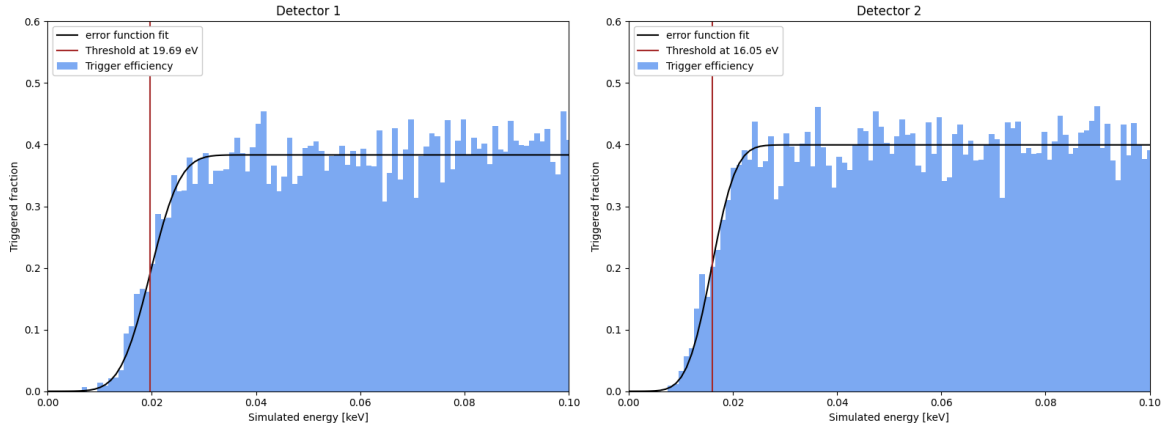


Figure 6.21: Confirmation of the energy threshold of detectors 1 and 2 using simulated data. We plotted the trigger efficiency against the simulated energy value (blue) and fitted the distribution with an error function (black line). We expect the threshold value to be at the energy value where the trigger efficiency drops below half of the constant trigger efficiency at higher energies. For detector 1 the threshold value is (19.7 ± 5.1) eV while for detector 2 it is (16.1 ± 4.4) eV (brown lines). For both detectors the threshold of the previous publication of 19.7 eV and 16.8 eV are within the fit errors. Original plot from [90].

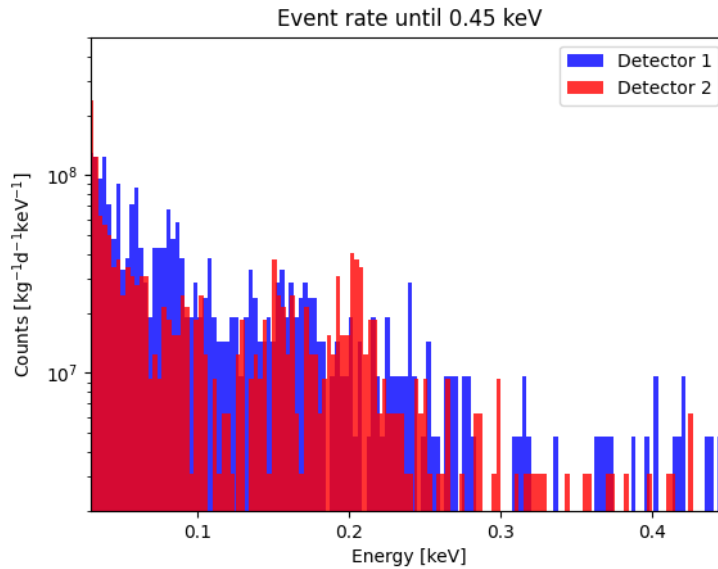


Figure 6.22: Event rate per kg day keV corrected with survival probability for the energy range 0.03-0.45 keV. We plotted the calibrated spectrum after trigger and quality cuts and corrected each energy bin of the size of 3 eV with the constant survival probability. The choice of the plotted energy range is motivated in the text.

6.3.5 Exclusion Limits

Although the purpose of this measurement was not a DM analysis, we also calculated exclusion limits on the elastic DM-nucleon interaction (as described in section 4.3.2) to visualize the sensitivity of the diamond detectors to low DM masses. The total exposure of both modules corresponds to 0.27 g-days. The results can be seen in figure 6.23 (and a zoomed in version in figure 6.24) where the exclusion limits obtained with detector 1 (blue) and detector 2 (red) are compared to the previous best above-ground limits of CRESST and to the best underground limits of CRESST (for masses below 0.16 GeV).

When comparing the two exclusion limits obtained with diamond detectors, one can observe that detector 2 is more sensitive to low DM masses. Indeed the value of the lowest DM mass excluded by detector 2 is 0.122 GeV/c², while for detector 1 it is 0.130 GeV/c², both for a cross-section $\sigma \sim 10^5 pb$. The sensitivity to lower masses of detector 2 is entirely attributable to the lower energy threshold compared to detector 1.

Furthermore, when comparing both diamond exclusion limits with the previous best above-ground limit (dashed black) one can clearly observe that the diamond detectors are extending the excluded parameter space below 0.2 GeV. The energy threshold of the measurement presented in dashed black is 19.7 eV and the target is a 0.5 g sapphire crystal (Al₂O₃) with a total exposure of 0.11 g-days. Therefore, the energy threshold is the same as for detector 1 (and comparable to detector 2) and also the exposures are in the same order of magnitude. For these reasons, the stronger sensitivity of the diamond detectors is attributable to the lighter nucleus of carbon, compared to aluminum or oxygen in sapphire, proving the advantage of using materials with light nuclei.

The best underground limit (for masses below 0.16 GeV/c²) obtained with a silicon wafer detector is shown as a reference for a better visualization of the performance of the diamond detectors. It has to be noticed that the goal of experiments located underground (e.g. DM analysis) usually implies much larger exposures than above-ground R&D measurements, which pushes exclusion limits to lower thresholds. It is therefore not surprising that the new above-ground limits do not probe a new parameter space (except a negligible part from detector 2) compared to the underground limits. It is however remarkable, that the lowest mass excluded by detector 2 (0.122 GeV/c²) is close to the lowest mass excluded by the silicon wafer detector (0.115 GeV/c²). Despite the higher energy threshold of the diamond detectors, compared to the one of the underground measurement (10 eV), the diamond detector can still probe comparable masses thanks to the lighter nucleus.

6.4 Conclusions

6.4.1 Evaluation of Results

The results presented in this chapter and published in [89] and [90] demonstrate the potential of diamond crystals used as target materials in cryogenic detectors. The low energy thresholds (16.8 eV and 19.7 eV) obtained with this proof-of-principle above-ground measurement confirm the prediction that the properties of diamond (such as the

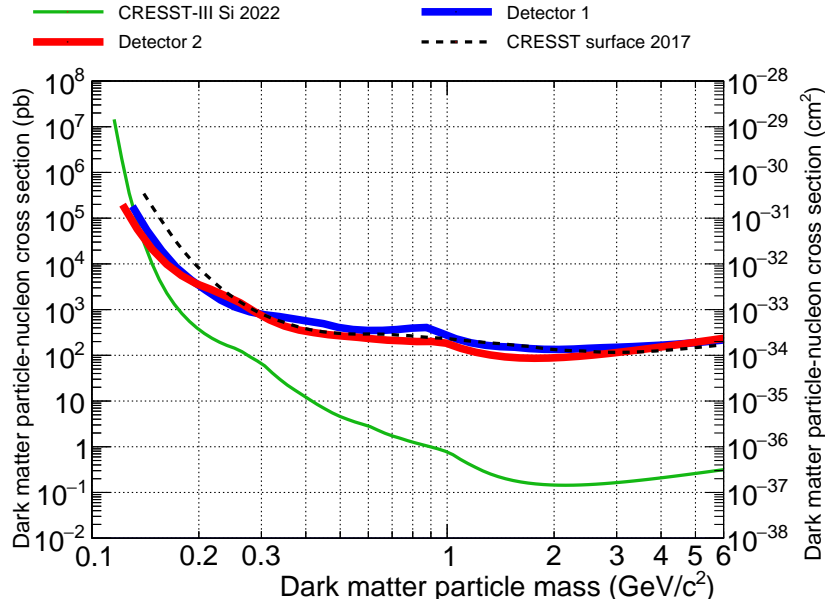


Figure 6.23: Upper limits for the elastic spin-independent DM-nucleon scattering cross-section, calculated for detector 1 (blue) and 2 (red). In black, the previous best above-ground exclusion limits of CRESST are plotted [99]. In green, the best exclusion limits below $0.160 \text{ GeV}/c^2$ from CRESST underground measurements [100] are plotted as a benchmark reference. Original plot from [90].

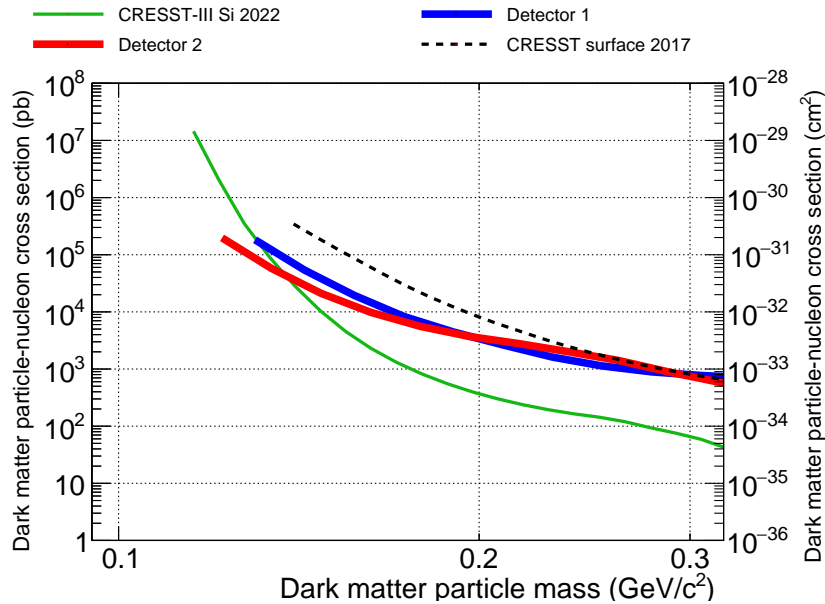


Figure 6.24: Zoom of figure 6.23. Original plot from [90].

high Debye temperature and good phonon propagation) make it an ideal material for sub-GeV direct detection DM experiments. Figures 6.23 and 6.24 prove the advantage of using materials with light nuclei by showing how more sensitive diamond detectors

can be, compared to detectors with comparable energy thresholds and exposure, but a heavier nucleus.

Although the measurement presented here was not meant for a DM analysis, it is remarkable how a simple proof-of-principle measurement in an above-ground facility can probe low DM masses very close to the ones excluded by a measurement in a low background facility.

By all means, the small volume of the diamond crystals presented in this work is not comparable to the ones usually used by the CRESST experiment (~ 50 times larger) and might therefore not be included in an underground measurement. Nonetheless, these results lay the foundation for the application of diamonds in DM searches and the research with this material is worth to be pursued further.

6.4.2 Outlook

In order to adopt diamond crystals in experiments such as CRESST, it is convenient to employ larger crystals in order to maximize the sensitivity to low cross-sections. For this purpose it is important to test the performance of detectors using larger diamond crystals and our group is already testing a crystal of the size $(5 \times 5 \times 7)$ mm³.

The results presented in this work were limited by the fast signal in diamond detectors that led to a low trigger efficiency caused by SQUID resets. Considering this, we are already improving our read-out chain by using faster SQUIDs. Besides that, we are currently working on the improvement of the TES sensor design. With these improvements, diamond detectors have the potential to explore new parameter space for the interaction of sub-GeV DM with ordinary matter.

Chapter 7

Conclusion and Outlook

The nature of dark matter is a longstanding question for which the scientific community has hypothesized numerous particle candidates at different masses. The effort to cover this broad mass range is shared by many experiments. Among these, the CRESST experiment contributes to this collective goal, providing sensitivity to sub-GeV dark matter particles.

The work presented in this thesis shows how the sensitivity of the CRESST experiment to light dark matter masses can be improved by employing light-nuclei target materials. Such materials are favored to probe light dark matter masses, due to the kinematics of the sought-for signal, the elastic scattering of a dark matter particle with a nucleon. The extent of improvement in sensitivity provided by light nuclei has been demonstrated through two measurements: one employing lithium-based crystals and one diamond crystals.

As the lightest element ($A=6$) that can be embedded in a crystalline structure, lithium could lead to ultimate sensitivity to light dark matter masses within the CRESST experiment. Besides being kinematically favored to test light DM masses, lithium also allows for probing a non-standard dark matter interaction, namely the spin-dependent DM-nucleon interaction. Thanks to the high $\langle S_{p/n} \rangle$ values of its isotopes (${}^7\text{Li}$ and ${}^6\text{Li}$), lithium is in fact one of the elements that provides the strongest sensitivity to such interactions. The combination of these advantageous aspects allowed to set world-leading upper limits on the elastic scattering spin-dependent DM-nucleon cross-section in the mass range $0.25 \text{ GeV}/c^2$ to $2.5 \text{ GeV}/c^2$ for the proton-only case and in the mass range of $0.16 \text{ GeV}/c^2$ to $1.5 \text{ GeV}/c^2$ for the neutron-only case. Based on these results, lithium-based crystals will be employed in future CRESST measurements. Nonetheless, some aspects should be improved. In this measurement, thresholds of $\sim 85 \text{ eV}$ were achieved, while the lowest threshold obtained with a detector of a similar size in CRESST was $\sim 30 \text{ eV}$. For future measurements it is crucial to improve the energy threshold, e.g. by optimizing the read-out sensor production. Moreover, the research on available lithium-based crystals, suitable for the CRESST technology, should be pursued further. The sensitivity to low dark matter masses can be improved by employing crystals that contain also other light nuclei, possibly also sensitive to spin-dependent interactions.

The first measurement of a diamond crystal as cryogenic calorimeter applied for dark matter searches is also presented. With the light nucleus of carbon ($A=12$), diamonds are an excellent target material that the CRESST experiment can adopt to improve its sensitivity. Besides the light nuclei, the high Debye temperature of this material is a figure of merit for the excellent phonon propagation in diamond crystals, that provides lower energy thresholds compared to other target crystals. This has been proven with the above-ground measurement presented in this manuscript, where thresholds below 20 eV have been achieved for two diamond detectors. Thanks to the light carbon nucleus and the achieved low energy thresholds, competitive upper limits on the elastic scattering spin-independent DM-nucleon cross-section could be set despite the very small exposure. Given these results, the research regarding diamonds will be pursued further, aiming at measuring them in the CRESST underground facility. To achieve this, diamond crystals with dimension $\sim 1\text{cm}^3$ should be obtained and the sensor design should be optimized to match the fast phonon propagation in this material, which are the subject of further studies.

Glossary

CL - Confidence Level

CP - Control Pulse

CPE - Convert Pulse height to Energy

ER - Electron Recoil

LEE - Low Energy Excess

LY - Light Yield

NPS - Noise Power Spectrum

NR - Nuclear Recoil

NTR - Noise Trigger Rate

OF - Optimum Filter

RMS - Root Mean Square

ROI - Region Of Interest

SD - Spin Dependent

SEV - Standard Event

SI - Spin Independent

SNR - Signal-to-Noise Ratio

SQUID - Superconducting QUantum Interference Devices

TES - Transition Edge Sensor

TP - Test Pulse

TPA - Test Pulse Amplitude

TPE - Test Pulse Equivalent

TPR - Test Pulse Response

Bibliography

- [1] F. Zwicky, On the masses of nebulae and of clusters of nebulae, *Astrophysical Journal* **86**, 217 (1937)
- [2] Particle data group, R.L. Workman Others, Chapter 22, *Prog. Theor. Exp. Phys.* 2022, 083C01, *PTEP* **2022**, 083C01 (2022)
- [3] Planck collaboration, N. Aghanim et al., Planck 2018 results - vi. cosmological parameters, *Astron. Astrophys.* **641**, A6 (2020). <https://doi.org/10.1051/0004-6361/201833910>
- [4] A.M. Green, Dark matter in astrophysics/cosmology, *SciPost Phys. Lect. Notes* p. 37 (2022). <https://scipost.org/10.21468/SciPostPhysLectNotes.37>
- [5] D. Clayton, *Principles of Stellar Evolution and Nucleosynthesis* (University of Chicago Press, 1984)
- [6] D. Tong. *Cosmology. Lecture Notes* (2019). <http://www.damtp.cam.ac.uk/user/tong/cosmo.html>
- [7] M. Davis et al., The end of cold dark matter?, *Nature* **356**(6369), 489 (1992). <https://doi.org/10.1038/356489a0>
- [8] E. Hubble, A relation between distance and radial velocity among extra-galactic nebulae, *Proceedings of the National Academy of Sciences* **15**(3), 168 (1929). <https://www.pnas.org/doi/abs/10.1073/pnas.15.3.168>
- [9] V. Rubin K. Ford, Rotation of the andromeda nebula from a spectroscopic survey of emission regions, *The Astrophysical Journal* **159**, 379 (1970)
- [10] V. Rubin et al., Rotational properties of 21 sc galaxies with a large range of luminosities and radii, from ngc 4605 (r=4kpc) to ugc 2885 (r=122kpc), *The Astrophysical Journal* **238**, 471 (1980)
- [11] G. Smoot et al., Structure in the COBE differential microwave radiometer first-year maps, *Astrophysical Journal Letters* **396**, L1 (1992)
- [12] Particle data group, R.L. Workman Others, Chapter 29, *Prog. Theor. Exp. Phys.* 2022, 083C01, *PTEP* **2022**, 083C01 (2022)

- [13] D. Clowe et al., A direct empirical proof of the existence of dark matter, *The Astrophysical Journal* **648**(2), L109 (2006). <https://doi.org/10.1086%2F508162>
- [14] R. Massey et al., The dark matter of gravitational lensing, *Reports on Progress in Physics* **73**(8), 086901 (2010). <https://doi.org/10.1088%2F0034-4885%2F73%2F8%2F086901>
- [15] S.W. Randall et al., Constraints on the self-interaction cross section of dark matter from numerical simulations of the merging galaxy cluster 1e 0657-56, *The Astrophysical Journal* **679**(2), 1173 (2008). <https://doi.org/10.1086%2F587859>
- [16] C.X. ray observatory (2021). <https://chandra.harvard.edu/photo/2006/1e0657/more.html>
- [17] J. Billard et al., Direct detection of dark matter- appec committee report, *Reports on Progress in Physics* **85**(5), 056201 (2022). <https://doi.org/10.1088%2F1361-6633%2Fac5754>
- [18] J.L. Feng, Dark matter candidates from particle physics and methods of detection, *Annual Review of Astronomy and Astrophysics* **48**(1), 495 (2010). <https://doi.org/10.1146/annurev-astro-082708-101659>
- [19] J.L. Feng, The WIMP paradigm: Theme and variations, *SciPost Physics Lecture Notes* (2023). <https://doi.org/10.21468%2Fscipostphyslectnotes.71>
- [20] S. Profumo. Tasi 2012 lectures on astrophysical probes of dark matter (2013). DOI 1301.0952. <https://arxiv.org/abs/1301.0952>
- [21] D. Bhatia S. Mukhopadhyay, Unitarity limits on thermal dark matter in (non-) standard cosmologies, *Journal of High Energy Physics* **2021**(3) (2021). [http://dx.doi.org/10.1007/JHEP03\(2021\)133](http://dx.doi.org/10.1007/JHEP03(2021)133)
- [22] Y. Hochberg, SIMP Dark Matter, *SciPost Phys. Lect. Notes* p. 59 (2022). <https://scipost.org/10.21468/SciPostPhysLectNotes.59>
- [23] K. Petraki R.R. Volkas, Review of Asymmetric Dark Matter **28**(19), 1330028 (2013). <https://doi.org/10.1142%2Fs0217751x13300287>
- [24] L.J. Hall et al., Freeze-In Production of FIMP Dark Matter, *JHEP* **03**, 080 (2010)
- [25] A. Boyarsky et al., Sterile neutrino dark matter, *Progress in Particle and Nuclear Physics* **104**, 1 (2019). <https://doi.org/10.1016%2Fj.pnnp.2018.07.004>
- [26] V. Brdar et al., Type i seesaw mechanism as the common origin of neutrino mass, baryon asymmetry, and the electroweak scale, *Physical Review D* **100**(7) (2019). <http://dx.doi.org/10.1103/PhysRevD.100.075029>

- [27] R.D. Peccei H.R. Quinn, CP conservation in the presence of pseudoparticles, Phys. Rev. Lett. **38**, 1440 (1977). <https://link.aps.org/doi/10.1103/PhysRevLett.38.1440>
- [28] G.G. di Cortona et al., The qcd axion, precisely, Journal of High Energy Physics **2016**(1) (2016). [http://dx.doi.org/10.1007/JHEP01\(2016\)034](http://dx.doi.org/10.1007/JHEP01(2016)034)
- [29] I.G. Irastorza, An introduction to axions and their detection, SciPost Phys. Lect. Notes p. 45 (2022). <https://scipost.org/10.21468/SciPostPhysLectNotes.45>
- [30] B. Carr F. Kuhnel, Primordial black holes as dark matter candidates, SciPost Phys. Lect. Notes p. 48 (2022). <https://scipost.org/10.21468/SciPostPhysLectNotes.48>
- [31] M. Milgrom, Mond theory, Canadian Journal of Physics **93**(2), 107–118 (2015). <http://dx.doi.org/10.1139/cjp-2014-0211>
- [32] H.E.S.S. Collaboration et al. Indirect dark matter searches with h.e.s.s (2007). DOI 0710.2493. <https://arxiv.org/abs/0710.2493>
- [33] M. Ahnen et al., Indirect dark matter searches in the dwarf satellite galaxy ursa major ii with the magic telescopes, Journal of Cosmology and Astroparticle Physics **2018**(03), 009–009 (2018). <http://dx.doi.org/10.1088/1475-7516/2018/03/009>
- [34] D.J. Thompson C.A. Wilson-Hodge, *Fermi Gamma-Ray Space Telescope* (Springer Nature Singapore, 2022), p. 1–31. DOI 10.1007/978-981-16-4544-0_58-1. http://dx.doi.org/10.1007/978-981-16-4544-0_58-1
- [35] D.P. Adan. Dark matter searches at cms and atlas (2023). DOI 2301.10141. <https://arxiv.org/abs/2301.10141>
- [36] F. J. Kerr, D. Lynden-Bell, Review of galactic constants, Mon. Notices Royal Astron. Soc. **221**(4), 1023 (1986). <https://doi.org/10.1093/mnras/221.4.1023>
- [37] F. Donato et al., Effects of galactic dark halo rotation on wimp direct detection, Astroparticle Physics **9**(3), 247–260 (1998). [http://dx.doi.org/10.1016/S0927-6505\(98\)00025-5](http://dx.doi.org/10.1016/S0927-6505(98)00025-5)
- [38] M. Smith et al., The RAVE survey: constraining the local Galactic escape speed, Mon. Notices Royal Astron. Soc. **379**(2), 755 (2007). <https://doi.org/10.1111/j.1365-2966.2007.11964.x>
- [39] P. Salucci, F.Nesti, G. Gentile, C. Frigerio Martins, The dark matter density at the sun’s location, Astron. Astrophys. **523**, A83 (2010). <https://doi.org/10.1051/0004-6361/201014385>

- [40] J. Cooley, Dark Matter direct detection of classical WIMPs, *SciPost Phys. Lect. Notes* p. 55 (2022). <https://scipost.org/10.21468/SciPostPhysLectNotes.55>
- [41] E.D. Nobile, *The Theory of Direct Dark Matter Detection* (Springer International Publishing, 2022). DOI 10.1007/978-3-030-95228-0. <https://doi.org/10.1007%2F978-3-030-95228-0>
- [42] M. Lisanti, in *New Frontiers in Fields and Strings* (WORLD SCIENTIFIC, 2016). DOI 10.1142/9789813149441_0007. https://doi.org/10.1142%2F9789813149441_0007
- [43] G. Dūda et al., Model-independent form factors for spin-independent neutralino–nucleon scattering from elastic electron scattering data, *Journal of Cosmology and Astroparticle Physics* **2007**(04), 012–012 (2007). <http://dx.doi.org/10.1088/1475-7516/2007/04/012>
- [44] M. Bauer T. Plehn. Yet another introduction to dark matter (2017). DOI 10.48550/ARXIV.1705.01987. <https://arxiv.org/abs/1705.01987>
- [45] P. Engel, J.; Vogel, Spin-dependent cross sections of weakly interacting massive particles on nuclei, *Physical Review D* 1989-nov 01 vol. 40 iss. 9 **40** (1989)
- [46] V.A. Bednyakov et al. Nuclear spin structure in dark matter search: The zero momentum transfer limit (2004). <https://arxiv.org/abs/hep-ph/0406218>
- [47] A.F. Pacheco D. Strottman, Nuclear-structure corrections to estimates of the spin-dependent wimp-nucleus cross section, *Phys. Rev. D* **40**, 2131 (1989). <https://link.aps.org/doi/10.1103/PhysRevD.40.2131>
- [48] A. Abdelhameed et al., First results from the CRESST-III low-mass dark matter program, *Physical Review D* **100**(10) (2019). <https://doi.org/10.1103%2Fphysrevd.100.102002>
- [49] P. Adari et al., EXCESS workshop: Descriptions of rising low-energy spectra, *SciPost Physics Proceedings* (9) (2022). <https://doi.org/10.21468%2Fscipostphysproc.9.001>
- [50] DarkSide collaboration, P. Agnes et al., Darkside-50 532-day dark matter search with low-radioactivity argon, *Physical Review D* **98**(10), 102006 (2018)
- [51] LUX collaboration, D.S. Akerib et al., Results from a search for dark matter in the complete lux exposure, *Physical Review Letters* **118**(2), 021303 (2017)
- [52] XENON collaboration, E. Aprile et al., Dark matter search results from a one ton-year exposure of xenon1t, *Physical Review Letters* **121**(11), 111302 (2018)

- [53] C.A.J. O'Hare, New definition of the neutrino floor for direct dark matter searches, *Physical Review Letters* **127**(25) (2021). <http://dx.doi.org/10.1103/PhysRevLett.127.251802>
- [54] EDELWEISS collaboration, E. Armengaud et al., Searching for low-mass dark matter particles with a massive Ge bolometer operated above ground, *Physical Review D* **99**(8), 082003 (2019)
- [55] SuperCDMS collaboration, I. Alkhatib et al., Light dark matter search with a high-resolution athermal phonon detector operated above ground, *Physical Review Letters* **127**(6), 061801 (2021)
- [56] XENON collaboration, E. Aprile et al., Search for light dark matter interactions enhanced by the migdal effect or bremsstrahlung in xenon1t, *Physical Review Letters* **123**(24), 241803 (2019)
- [57] M.J. Dolan et al., Directly detecting sub-gev dark matter with electrons from nuclear scattering, *Phys. Rev. Lett.* **121**, 101801 (2018). <https://link.aps.org/doi/10.1103/PhysRevLett.121.101801>
- [58] E. Armengaud et al., Searching for low-mass dark matter particles with a massive Ge bolometer operated above ground, *Physical Review D* **99**(8) (2019). <http://dx.doi.org/10.1103/PhysRevD.99.082003>
- [59] R. Agnese et al., Low-mass dark matter search with cdmslite, *Physical Review D* **97**(2) (2018). <http://dx.doi.org/10.1103/PhysRevD.97.022002>
- [60] E. Aprile et al., Constraining the spin-dependent wimp-nucleon cross sections with xenon1t, *Physical Review Letters* **122**(14) (2019). <http://dx.doi.org/10.1103/PhysRevLett.122.141301>
- [61] D. Akerib et al., Limits on spin-dependent wimp-nucleon cross section obtained from the complete lux exposure, *Physical Review Letters* **118**(25) (2017). <http://dx.doi.org/10.1103/PhysRevLett.118.251302>
- [62] PandaX-II collaboration, C. Fu Anonymous, Erratum: Spin-dependent weakly-interacting-massive-particle-nucleon cross section limits from first data of PandaX-II experiment [*phys. rev. lett.* 118, 071301 (2017)], *Phys. Rev. Lett.* **120**, 049902 (2018). <https://link.aps.org/doi/10.1103/PhysRevLett.120.049902>
- [63] J. Collar, Search for a nonrelativistic component in the spectrum of cosmic rays at earth, *Physical Review D* **98**(2) (2018). <http://dx.doi.org/10.1103/PhysRevD.98.023005>
- [64] A.H. Abdelhameed et al., First results on sub-GeV spin-dependent dark matter interactions with ${}^7\text{Li}$, *The European Physical Journal C* **79**(7) (2019). <https://doi.org/10.1140%2Fepjc%2Fs10052-019-7126-4>

- [65] C. Amole et al., Dark matter search results from the complete exposure of the pico-60 bubble chamber, *Physical Review D* **100**(2) (2019). <http://dx.doi.org/10.1103/PhysRevD.100.022001>
- [66] G. Angloher et al., Probing spin-dependent dark matter interactions with ${}^6\text{Li}$, *The European Physical Journal C* **82**(3), 207 (2022). <https://doi.org/10.1140/epjc/s10052-022-10140-3>
- [67] C. Pröbst, Frank et al., Model for cryogenic particle detectors with superconducting phase transition thermometers, *Journal of Low Temperature Physics* **100**(1-2), 69 (1995). <https://doi.org/10.1007/BF00753837>
- [68] M. Gluyas et al., The elastic constants of calcium tungstate, 4·2-300 K, *Journal of Physics D: Applied Physics* **6**, 2025 (2002)
- [69] G. Bellini et al., Cosmic-muon flux and annual modulation in borexino at 3800 m water-equivalent depth, *Journal of Cosmology and Astroparticle Physics* **2012**(05), 015 (2012). <https://doi.org/10.1088%2F1475-7516%2F2012%2F05%2F015>
- [70] A. Tanzke, Low-Threshold Detectors for Low-Mass Direct Dark Matter Search with CRESST-III. Ph.D. thesis, Munich, Tech. U. (2017)
- [71] R. Strauss et al., Gram-scale cryogenic calorimeters for rare-event searches, *Phys. Rev. D* **96**, 022009 (2017). <https://link.aps.org/doi/10.1103/PhysRevD.96.022009>
- [72] F. Reindl, Exploring light dark matter with CRESST-II low-threshold detectors. Ph.D. thesis, Technische Universität München (2016)
- [73] N.F. Iachellini. Increasing the sensitivity to low mass dark matter in CRESST-III with a new daq and signal processing (2019). <http://nbn-resolving.de/urn:nbn:de:bvb:19-237623>
- [74] A.C. Kinast, Enhancing the dark matter sensitivity of cressst: Purification, stress reduction and ${}^{17}\text{O}$ enrichment of CaWO_4 target crystals. Ph.D. thesis, Technische Universität München (2023)
- [75] E. Gatti, P. F. Manfredi, Processing the signals from solid-state detectors in elementary-particle physics, *La Rivista del Nuovo Cimento* (1978-1999) **9**(1), 1 (1986). <https://doi.org/10.1007/BF02822156>
- [76] M. Mancuso et al., A low nuclear recoil energy threshold for dark matter search with CRESST-III detectors, *Journal of Low Temperature Physics* **193**(3), 441 (2018). <https://doi.org/10.1007/s10909-018-1948-6>
- [77] S. Yellin, Finding an upper limit in the presence of an unknown background, *Physical Review D* **66**(3) (2002). <http://dx.doi.org/10.1103/PhysRevD.66.032005>

- [78] G. Cowan et al., Asymptotic formulae for likelihood-based tests of new physics, *The European Physical Journal C* **71**(2), 1554 (2011). <https://doi.org/10.1140/epjc/s10052-011-1554-0>
- [79] G. Angloher et al., Testing spin-dependent dark matter interactions with lithium aluminate targets in CRESST-III, *Physical Review D* **106**(9) (2022). <http://dx.doi.org/10.1103/PhysRevD.106.092008>
- [80] J. Meija et al., Isotopic compositions of the elements 2013 (iupac technical report), *Pure and Applied Chemistry* **88**(3), 293 (2016). <https://doi.org/10.1515/pac-2015-0503>
- [81] A.K.H. Langenkämper, Characterisation of the muon-induced neutron background with a lif cryogenic detector. Ph.D. thesis, Technische Universität München (2023)
- [82] A. Gnech et al., Calculation of the ${}^6\text{Li}$ ground state within the hyperspherical harmonic basis, *Phys. Rev. C* **102**, 014001 (2020). <https://link.aps.org/doi/10.1103/PhysRevC.102.014001>
- [83] A.F. Pacheco D. Strottman, Nuclear-structure corrections to estimates of the spin-dependent wimp-nucleus cross section, *Phys. Rev. D* **40**, 2131 (1989). <https://link.aps.org/doi/10.1103/PhysRevD.40.2131>
- [84] M.T. Ressell et al., Nuclear shell model calculations of neutralino-nucleus cross sections for ${}^{29}\text{Si}$ and ${}^{73}\text{Ge}$, *Phys. Rev. D* **48**, 5519 (1993). <https://link.aps.org/doi/10.1103/PhysRevD.48.5519>
- [85] J. Engel et al., Response of mica to weakly interacting massive particles, *Phys. Rev. C* **52**, 2216 (1995). <https://link.aps.org/doi/10.1103/PhysRevC.52.2216>
- [86] A.H. Abdelhameed et al., First results on sub-gev spin-dependent dark matter interactions with ${}^7\text{Li}$, *The European Physical Journal C* **79**(7), 630 (2019). <https://doi.org/10.1140/epjc/s10052-019-7126-4>
- [87] E.E. Haller et al., *NTD Germanium: A Novel Material for Low Temperature Bolometers* (Springer US, Boston, MA, 1984), pp. 21–36. DOI 10.1007/978-1-4613-2695-3_2. https://doi.org/10.1007/978-1-4613-2695-3_2
- [88] A.H. Abdelhameed et al., Cryogenic characterization of a LiAlO_2 crystal and new results on spin-dependent dark matter interactions with ordinary matter, *The European Physical Journal C* **80**(9), 834 (2020). <https://doi.org/10.1140/epjc/s10052-020-8329-4>
- [89] Abdelhameed, A. H. et al., A low-threshold diamond cryogenic detector for sub-gev dark matter searches, *Eur. Phys. J. C* **82**(9), 851 (2022). <https://doi.org/10.1140/epjc/s10052-022-10829-5>

- [90] G. Angloher et al., Light dark matter search using a diamond cryogenic detector, *The European Physical Journal C* **84**(3), 324 (2024). <https://doi.org/10.1140/epjc/s10052-024-12647-3>
- [91] N. Kurinsky et al., Diamond detectors for direct detection of sub-gev dark matter, *Phys. Rev. D* **99**, 123005 (2019). <https://link.aps.org/doi/10.1103/PhysRevD.99.123005>
- [92] P.M. Martin, *Handbook of Deposition Technologies for Films and Coatings*, third edition edn. (William Andrew Publishing, Boston, 2010). DOI <https://doi.org/10.1016/B978-0-8155-2031-3.00001-6>. <https://www.sciencedirect.com/science/article/pii/B9780815520313000016>
- [93] C. Kittel, *Introduction to Solid State Physics*, 8th edn. (Wiley, 2005)
- [94] R.F. Lang W. Seidel, Search for dark matter with CRESST, *New Journal of Physics* **11**(10), 105017 (2009). <https://doi.org/10.1088/2F1367-2630/2F11/2F10/2F105017>
- [95] M. Cruceru G. Nicolescu, Detection of solar neutrinos with a torsion balance with sapphire crystal, *Journal of Physics: Conference Series* **940**(1), 012036 (2018). <https://dx.doi.org/10.1088/1742-6596/940/1/012036>
- [96] S.M. Griffin et al., Multichannel direct detection of light dark matter: Target comparison, *Physical Review D* **101**(5) (2020). <https://doi.org/10.1103/2Fphysrevd.101.055004>
- [97] <https://www.audiatec.de/>. <https://www.audiatec.de/>. Accessed: July 18, 2024
- [98] J.F.M. Rothe, Low-threshold cryogenic detectors for low-mass dark matter search and coherent neutrino scattering. Ph.D. thesis, Technische Universität München (2021)
- [99] CRESST collaboration, G. Angloher et al., Results on mev-scale dark matter from a gram-scale cryogenic calorimeter operated above ground, *Eur. Phys. J. C* **77**(9), 637 (2017). <https://doi.org/10.1140/epjc/s10052-017-5223-9>
- [100] CRESST collaboration, G. Angloher et al., Results on sub-gev dark matter from a 10 eV threshold CRESST-III silicon detector, *Phys. Rev. D* **107**, 122003 (2023). <https://link.aps.org/doi/10.1103/PhysRevD.107.122003>

Testing spin-dependent dark matter interactions with lithium aluminate targets in CRESST-III

G. Angloher,¹ S. Banik,^{4,5} G. Benato,² A. Bento,^{1,§} A. Bertolini,^{1,*} R. Breier,⁸ C. Bucci,² J. Burkhart,^{4,5} L. Canonica,¹ A. D'Addabbo,² S. Di Lorenzo,² L. Einfalt,^{4,5} A. Erb,^{3,¶} F. v. Feilitzsch,³ N. Ferreiro Iachellini,¹ S. Fichtinger,⁴ D. Fuchs,¹ A. Fuss,^{4,5} A. Garai,¹ V. M. Ghete,⁴ S. Gerster,⁶ P. Gorla,² P. V. Guillaumon,² S. Gupta,^{4,†} D. Hauff,¹ M. Jeřkovský,⁸ J. Jochum,⁶ M. Kaznacheeva,³ A. Kinast,³ H. Kluck,^{4,5} H. Kraus,⁷ A. Langenkämper,^{3,1} M. Mancuso,¹ L. Marini,^{2,||} L. Meyer,⁶ V. Mokina,⁴ A. Nilima,¹ M. Olmi,² T. Ortman,³ C. Pagliarone,^{2,**} L. Pattavina,^{3,2} F. Petricca,¹ W. Potzel,³ P. Povinec,⁸ F. Pröbst,¹ F. Pucci,¹ F. Reindl,^{4,5} J. Rothe,³ K. Schäffner,¹ J. Schieck,^{4,5} D. Schmiedmayer,^{4,5} S. Schönert,³ C. Schwertner,^{4,5} M. Stahlberg,¹ L. Stodolsky,¹ C. Strandhagen,⁶ R. Strauss,³ I. Usherov,⁶ F. Wagner,^{4,‡} M. Willers,³ and V. Zema¹

(CRESST Collaboration)

¹Max-Planck-Institut für Physik, 80805 München, Germany

²INFN, Laboratori Nazionali del Gran Sasso, 67010 Assergi, Italy

³Physik-Department, Technische Universität München, 85747 Garching, Germany

⁴Institut für Hochenergiephysik der Österreichischen Akademie der Wissenschaften, 1050 Wien, Austria

⁵Atominstytut, Technische Universität Wien, 1020 Wien, Austria

⁶Eberhard-Karls-Universität Tübingen, 72076 Tübingen, Germany

⁷Department of Physics, University of Oxford, Oxford OX1 3RH, United Kingdom

⁸Faculty of Mathematics, Physics, and Informatics, Comenius University, 84248 Bratislava, Slovakia



(Received 25 July 2022; accepted 15 November 2022; published 28 November 2022)

In the past decades, numerous experiments have emerged to unveil the nature of dark matter, one of the most discussed open questions in modern particle physics. Among them, the Cryogenic Rare Event Search with Superconducting Thermometers (CRESST) experiment, located at the Laboratori Nazionali del Gran Sasso, operates scintillating crystals as cryogenic phonon detectors. In this work, we present first results from the operation of two detector modules which both have 10.46 g LiAlO₂ targets in CRESST-III. The lithium contents in the crystal are ⁶Li, with an odd number of protons and neutrons, and ⁷Li, with an odd number of protons. By considering both isotopes of lithium and ²⁷Al, we set the currently strongest cross section upper limits on spin-dependent interaction of dark matter with protons and neutrons for the mass region between 0.25 and 1.5 GeV/c².

DOI: 10.1103/PhysRevD.106.092008

I. INTRODUCTION

The nature of dark matter (DM) is one of the most discussed open questions in modern physics and has been the motivation for numerous experiments in the past decades. DM direct detection experiments aim at measuring the scattering of DM particles directly off a target material to test interaction scenarios of particle DM with standard model (SM) particles [1]. A particularly promising DM model is the weakly interacting massive particle (WIMP) model [2]. Direct-detection experiments searching for WIMPs are sensitive to two parameters: the WIMP mass and its effective interaction cross section. The original WIMP model considers the weak nuclear force as the mediating force between DM and the SM. The model is in conflict with the Lee-Weinberg bound for light DM [3] but remains valid for other massive mediators and

*Corresponding author.
anbertol@mpp.mpg.de

†Corresponding author.
shubham.gupta@oeaw.ac.at

‡Corresponding author.
felix.wagner@oeaw.ac.at

§Also at LIBPhys, Departamento de Física, Universidade de Coimbra, P3004 516 Coimbra, Portugal.

¶Also at Gran Sasso Science Institute, 67100, L'Aquila, Italy.

||Also at Walther-Meißner-Institut für Tieftemperaturforschung, 85748 Garching, Germany.

**Also at Dipartimento di Ingegneria Civile e Meccanica, Università degli Studi di Cassino e del Lazio Meridionale, 03043 Cassino, Italy.

is used as a benchmark model to compare results from different experiments.

The Cryogenic Rare Event Search with Superconducting Thermometers (CRESST) experiment probes the interaction of DM with scintillating crystals operated as cryogenic calorimeters in a low-background facility at the Laboratori Nazionali del Gran Sasso (LNGS). The experiment is in its third phase (CRESST-III), focusing on sub-GeV/ c^2 DM searches, using crystals with light nuclei as targets and transition edge sensors (TESs) as phonon sensors. With this technology, CRESST-III provides one of the strongest limits for spin-independent interactions with sub-GeV/ c^2 DM and the strongest under standard assumptions [4]. The cryogenic technology is versatile and allows for changing the target material. In recent runs multiple materials were employed simultaneously in individual detector modules: calcium tungstate, sapphire, silicon, and lithium aluminate (LiAlO₂). With a very low atomic number and unpaired nuclei, lithium has appealing properties to test light DM with spin-dependent interactions. In previous measurements above ground, the CRESST Collaboration demonstrated the competitiveness of DM results achieved with lithium targets [5]. LiAlO₂ is a suitable target material in particular, because a TES can be deposited directly on the crystal surface, and the CRESST light detectors have a high absorption at the wavelength of its scintillation peak. The motivations behind the detector design were discussed in detail in Ref. [6]. The inclusion of ⁶Li in the calculation of DM results was studied in Ref. [7].

In the current phase of the experiment CRESST-III is operating two detector modules with LiAlO₂ targets. In this paper we present the dark matter search performed on the data acquired between February and August 2021. We discuss the design choices of the detector module and the experimental setup at LNGS in Sec. II. The details of the analysis chain are explained in Sec. III. The datasets allow for the calculation of upper limits on the spin-dependent DM-SM cross section. We present these in Sec. IV and conclude the discussion in Sec. V.

II. DETECTOR DESIGN AND EXPERIMENTAL SETUP

The detector modules “Li1” and “Li2” were identically manufactured in the laboratories of the Max-Planck-Institut für Physik in Munich. A picture of the Li1 module during the assembly phase is displayed in Fig. 1.

The modules are constituted by a phonon detector and a light detector, mounted in a copper housing. The phonon detectors feature LiAlO₂ absorber crystals, which were provided by the Leibniz-Institut für Kristallzüchtung and have the dimensions of $(2 \times 2 \times 1)$ cm³. The targets have a weight of 10.46 g each. The lithium in LiAlO₂ occurs as ⁷Li and ⁶Li with natural abundances of 92.41% and 7.49%, respectively [8] while aluminium occurs as ²⁷Al with a

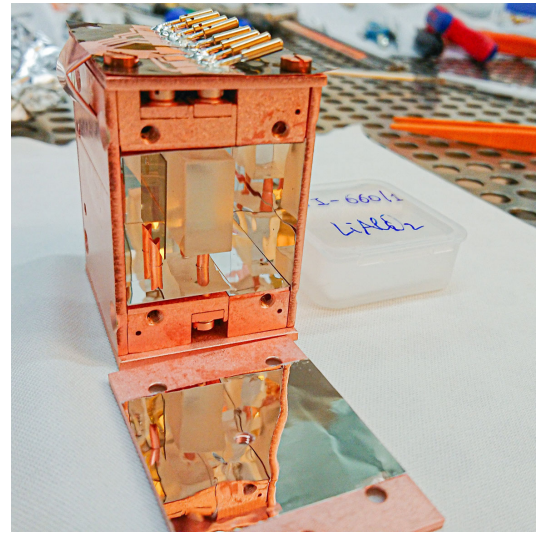


FIG. 1. The Li1 detector module. Inside the copper housing, a LiAlO₂ crystal (right, transparent) as a target for particle scattering is held by three copper sticks as a target for particle scattering. Next to the crystal a SOS light detector (left, gray) is mounted. The inside of the housing is covered with reflective foil, best visible on the detached side of the module (center, lower part of the picture).

natural abundance of 100%. LiAlO₂ emits scintillation light with an emission maximum at a wavelength of 340 nm [9]. A silicon-on-sapphire (SOS) substrate of $(2 \times 2 \times 0.04)$ cm³ is placed next to the crystal to detect the scintillation light. Both the LiAlO₂ crystal and the SOS substrate are equipped with a tungsten TES featuring Al phonon collectors.

The housing of the detector modules are made from copper with the crystals held in place by three copper sticks. The inner side of the housing is covered with reflective and scintillating foil, a 3M Vikuiti™ enhanced specular reflector, to maximize the collection efficiency of scintillation light emitted by the target LiAlO₂ crystal.

The modules were operated next to each other in the CRESST setup at LNGS, which is located below the Gran Sasso massif in central Italy with a rock overburden of 3600 m water equivalent. The vertical muon flux inside the lab was measured to ~ 1 counts/m²/h [10–12]. Remaining muons are tagged by active muon veto panels around the experiment, which cover the detector location to more than 98%. Additional shieldings are in place: a polyethylene layer protects the detectors from environmental neutrons. Inside the polyethylene, a lead and a copper layer shield against γ rays. Directly surrounding the detector modules, a second polyethylene layer moderates neutrons produced inside the lead and copper.

For the measurement, the detector modules are cooled with a commercial $^3\text{He}/^4\text{He}$ -dilution refrigerator to a base temperature of about 5 mK. The temperature of the TES is stabilized with heating resistors on the holding structure of the detector modules and on the crystal itself, to an operation point within the superconducting phase transition, which is around 15 mK. The heating resistor is also used to periodically induce thermal pulses every 10 sec that saturate the TES (control pulses) to measure and stabilize the exact working point within the superconducting transition. Additionally, in between the control pulses, thermal pulses (in the following called “test pulses”) with certain amplitudes (TPA) are sent every 20 sec to monitor the calibration over time [13,14]. The TESs are read out by a superconducting quantum interference device (SQUID) amplifier and continuously digitized with 16 bit precision and 25 kHz sampling frequency.

An ^{55}Fe source with an activity of ~ 1 mBq was mounted inside each detector housing to calibrate the detector response to electron recoils. For the calibration of the detector response to nuclear recoils and after the collection of the dataset for the calculation of physics results, an AmBe source with an activity of ~ 35.5 MBq was put in place, outside the shielding of the experimental setup, to provide a strong neutron flux.

The TES of the light detector of Li2 did not show a transition to a superconducting state and the channel could therefore not be operated. We could only read out one channel of the module, the phonon channel. However, the Li1 module has the scintillation light channel, which enabled the discrimination between electron and nuclear recoils by their individual quenching factor. We use the Li2 module for cross checks of the analysis chain, while the Li1 module provides the performance for competitive DM results.

III. DATA ANALYSIS

A particle recoil inside the target produces a population of athermal phonons, which spread ballistically over the crystal. They thermalize mostly through scattering with the crystal surface, heating up the crystal. A share of the athermal phonons is collected by the phonon collectors and led to the thermometer. This produces a temperature signal with two components in the TES, corresponding to the athermal and thermal phonons, respectively. The employed TESs are designed such that the athermal component dominates the pulse height and sensitivity of the detector. For small energy depositions, the pulse height scales approximately linearly with the deposited energy. This model was thoroughly described in Ref. [15]. For larger recoil energies, saturation effects of the TES cause a flattening of the pulses. In our DM dataset we consider only the region of linear pulse height.

The dataset of the total measurement is split into a training and a blind dataset. The blind dataset for Li1 accumulates to 2665 h measurement time, for the Li2

module to 2716 h. The total exposure of the blind set is 1.161 kg days (Li1) and 1.184 kg days (Li2). That of the used training set is 0.153 kg days (Li1 and Li2 each). The analysis, including the event selection, is designed on the training set and applied with no further modification to the blind set. This procedure is recommended within the DM community [16].

A. Trigger and data processing

As a first step in the detector characterization we generate a standard event (SEV) for recoil events by averaging a selection of events from a narrow energy interval. The SEV is then used to create an optimum (matched) filter (OF) that corresponds to the quotient of our SEV and the noise power spectrum in frequency space [17,18]. The OF provides the theoretically optimal signal-to-noise ratio for events with the characteristic particle recoil SEV shape and is applied to the recorded data stream for off-line triggering with an optimized trigger threshold. The trigger threshold is calibrated to 1 noise trigger/kg/day with the method proposed in Ref. [19] on the training set data. The triggered events are stored in windows with a length of 16384 samples, where the trigger position is placed at $1/4$ of the window size. We extract the main shape parameters of each triggered pulse for both the phonon and light channel: e.g. pulse height, onset, rise, and decay time of the values within the pulse window. These values are stored for the phonon and light channel individually. Additionally, we fit each pulse with the SEV plus a third-order polynomial to model the baseline fluctuations and record the fitted pulse height and root-mean-square deviation of the fit. With a truncated template fit, also weakly saturated pulse heights could be reconstructed. This is done by scaling the SEV until it properly fits the part of the pulse which is within the linear region of the TES response, reconstructing an amplitude which is higher than the saturated one [20].

For cross checks and validation purposes, the analysis of the modules was done by independent analysts. For data processing and analysis we used a collaboration internal package CAT and the publicly available PYTHON package CAIT [21].

B. Energy calibration

The energy scale of our detector is calibrated with an iron source (^{55}Fe) emitting x rays. The spectral lines for x-ray hits in the target and directly in the light detector are clearly visible in both channels, respectively, and provide recoil-type independent (total) energy scales. The scintillation light produced by the iron source shining on the target is visible in the light detector as well, thus a measure of the detected light coming from the crystal and an electron equivalent (ee)-energy scale calibration are possible.

The test pulses are used to fine-tune the slight non-linearities in the transition curve. The TPA values scale similarly to the recoil energy of particle events. The pulse heights of particle events are therefore first translated to

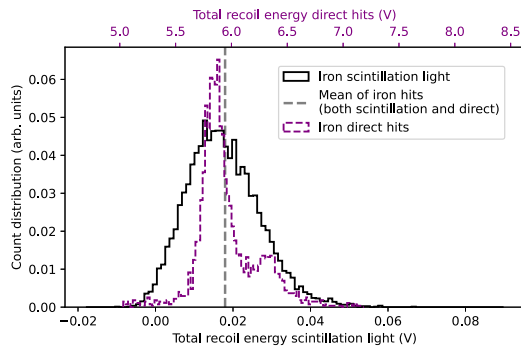


FIG. 2. Overlay of the normalized Li1 light detector energy count distribution of the iron line from scintillation light (black, bottom x axis) and the iron line from direct hits (purple dotted, top x axis). The two x axes are shifted and scaled, such that the average value of the two iron lines overlap. Their ratio determines the collected light of the target (see text).

equivalent TPA values. Knowing the mean energies 5.89 and 6.49 keV corresponding to the K- α and K- β shells, respectively, we can convert these values with a linear factor to recoil energies.

The collected scintillation light is the share of energy from an electron recoil in the crystal that is emitted as scintillation light and detected by the light detector. We estimate it for Li1, using the spectral x-ray lines from the iron source. Specifically, we compare the mean amplitude of events registered by the light detector when the iron x ray is absorbed in the crystal (black line in Fig. 2) to that of events where the x ray is directly absorbed by the light detector (purple dotted line in Fig. 2). With this procedure, we measure the value $(0.302 \pm 0.001)\%$. The reported uncertainty includes only statistical fluctuations, the systematic uncertainties are expected to be much larger.

C. Event selection

We apply several cuts to the events in order to reject nonphysical pulses caused e.g. by earthquakes or human activity inside the laboratory. To develop such cuts, we first select time periods where the detectors were operated in stable conditions:

- (i) We exclude periods of time when the detector is out of its operating point. To do so we remove periods where the height of control pulses is not within 3σ of its mean value.
- (ii) We calculate the average rate of particle recoils within all 10 min intervals of the measurement. We exclude time intervals with an average rate not within 3σ of the mean rate of all intervals (≈ 0.4 events/min).

We then use the data from the stable periods to develop quality cuts on the pulse shape parameters which are designed with the goal to keep only events with particle recoils with a correct energy reconstruction.

Finally, we apply an anticoincidence cut, taking advantage of the muon veto panels, which trigger and record the time stamps of incoming muons. For each trigger of a muon panel we exclude a window of $+10/-5$ ms. The muon veto triggers with 4.52 Hz, most of which are dark counts. The muon veto cut removes 6.82% of the events and 6.79% of the exposure. The expected percentage of event removed due to random coincidences is $(6.79 \pm 0.23)\%$. Similar observations were made for the Li2 module.

In the same run, CRESST-III operated ten detector modules independently, mounted inside the same holding structure. Due to their low interaction probability, DM recoils are expected to be seen only in single modules (multiplicity 1). Other particle recoils or environment-induced energy depositions can feature a higher multiplicity. Therefore we apply an anticoincidence cut on the multiplicity of events: for each trigger in another detector module, we exclude a window of $+10/-10$ ms in the Li1 and Li2 detector. This cut removes 0.93 h runtime in Li1, which is 0.0387% of the exposure, and two events from the Li1 blind dataset. Also for Li2 a negligible share of exposure was removed, and no additional events were rejected by this cut.

Our event selection for the blind dataset of the Li1 module is visualized in Fig. 3. As the event selection was designed on the training dataset, the remaining outliers are an effect of the imperfect generalization from the training to the blind data. Nevertheless, overall we observe a good performance of our chosen cuts in the discrimination between recoils and artifacts. In Fig. 4 the calibrated spectrum of the final event selection can be seen. At low energies the Li2 module has a significantly higher number of events compared to the Li1 module. This is related to a special class of events that is highlighted in Fig. 3 (right, red). A significant share of the events with low recoil energies (below 1 keV) in the phonon channel coincidentally has the pulse shape of direct hits in the light channel (see Sec. III E) and corresponds to large energy depositions. Direct hits feature a significantly sharper pulse shape as the phonon population is created instantaneously with a single particle scattering, while in the formation of a pulse shape from scintillation light multiple photons are collected and accumulate to form the observed pulse shape. In the past these events could be connected to the presence of the reflective foil inside the housing of the detector module [22]. With the information from the light channel these events can be identified in the Li1 data, while in Li2, they remain in the final DM dataset.

D. Efficiency and detector performance

We evaluate the overall selection cut efficiency simulating 2×10^6 particle recoil events for the two modules, respectively. These events are evenly distributed in the time of the measurement and the identical analysis chain of the blind data is applied to the simulated events.

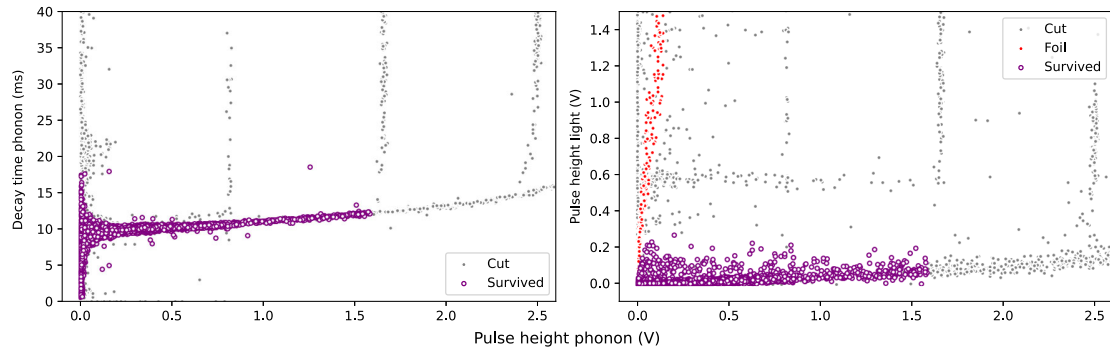


FIG. 3. Visualization of the surviving (purple) and cut (gray) events in the Li1 DM dataset. Left: the distribution of decay times in the phonon channel over pulse heights in the phonon channel. The band of recoil events is clearly visible and mostly distinct from the artefact events. For pulse heights below 0.2 V the band widens, which degrades the discriminating power of quality cuts. Right: the distribution of pulse heights in the light channel versus the corresponding pulse height in the phonon channel. Again, the band of particle recoils is clearly visible. For low phonon pulse heights the event class of foil events appears: due to their high pulse height in the light channel, higher than for regular target recoils, these events can be rejected as background. In both pictures the vertical event bands, as well as the secondary horizontal event bands, are SQUID resets caused by high energetic recoils.

The energy-dependent survival rate of the simulated events provides a realistic estimate of the survival probability of particle recoil events and is used for the limit calculation. To obtain a statement on the energy threshold, we fit an error function to the triggered events as a function of the simulated recoil energy. The energy threshold of our detectors is defined as the recoil energy at which the error function drops below half of its constant value at higher energies (see Fig. 5). We find an energy threshold of (83.60 ± 0.02) eV for the Li1 module and (94.09 ± 0.13) eV for the Li2 module. These values correspond to the voltage value chosen as trigger threshold, converted to a recoil energy. The constant trigger efficiencies above

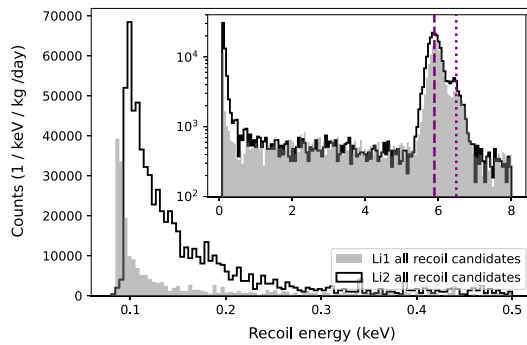


FIG. 4. Recoil energy spectrum for the Li1 (gray) and Li2 (black) modules. Inset: the energy region up to 8 keV. The most prominent event clusters are the LEE and the two iron lines (purple dashed, $K-\alpha$; purple dotted, $K-\beta$). Main figure: the energy region up to 0.5 keV, dominated by the LEE. The Li1's LEE is less prominent due to the cut based on light channel information, which removes the foil events.

threshold are $(85.71 \pm 0.01)\%$ for Li1 and $(81.26 \pm 0.08)\%$ for Li2. The plateau is not at unity due to the induced dead time from test and control pulses and the dead time caused by previous triggers.

We estimate the baseline energy resolution of the phonon detector with the width of the fitted error function. This leads for the Li1 module to a value of (13.10 ± 0.02) eV and for the Li2 module to a value of (15.89 ± 0.18) eV. For the light channel of the Li1 module, we estimate the baseline energy resolution by superimposing the standard

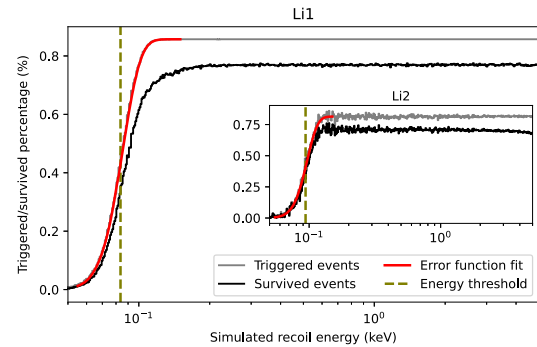


FIG. 5. The normalized trigger rate (gray) and survival rate (black) of simulated Li1 events (Li2 events in inset), as a function of the simulated recoil energy. The latter provides a realistic estimate of the survival probability. The energy threshold (olive, dashed) is the recoil energy at which the fitted error function (red) drops below 0.5 times the constant triggered fraction above threshold. The constant trigger efficiency for Li1 is $(85.71 \pm 0.01)\%$ and the trigger energy threshold (83.60 ± 0.02) eV. For Li2 the trigger efficiency is $(81.26 \pm 0.08)\%$ and the trigger energy threshold (94.09 ± 0.13) eV.

G. ANGLOHER *et al.*PHYS. REV. D **106**, 092008 (2022)

event to a set of empty noise traces and measuring the standard deviation (σ) of the reconstructed pulse heights. We observe a baseline resolution of (748 ± 7) eV_{ee} (*ee* energy scale) and (2.26 ± 0.02) eV (total energy scale). The method used for the phonon channel is more precise, as it includes also corrections of the detector response over time. However, the values agree with the ones obtained with the second method.

E. Results

In the final DM dataset, shown in Fig. 7 (left, black), it is possible to identify three main contributions: first, the x-ray lines at 5.89 and 6.49 keV induced by the internal calibration source and second, the beta spectrum of tritium. Beta events from tritium are expected due to the accumulation of tritium inside the crystal. ${}^6\text{Li}$ has a high cross section for the reaction ${}^6\text{Li}(n, \alpha)$ which leaves behind tritium nuclei inside the crystal lattice. The third contribution is a low energy excess (LEE), a phenomenon that is seen by many experiments with low energy thresholds and is the matter of ongoing discussion in the community [23–26]. Its origin is still unclear. An interpretation of the foil events as the origin of the LEE can be excluded due to their significantly different spectral shape. As there is no method to discriminate particle recoils from LEE events, we treat them as particle recoils in the analysis.

In Fig. 7 (right) the count rate between threshold and 500 eV is displayed in this energy region the main contribution is given by the LEE. The LEE spectrum can be fitted with a combination of an exponential and a power law function:

$$f(x, a, b, c, d) = a \exp(-bx) + cx^{-d}, \quad (1)$$

where x is the running parameter, and a , b , c , and d are free fit parameters. The values obtained with a χ^2 fit to the

TABLE I. The parameters obtained from a χ^2 fit of Eq. (1) to the binned spectrum for the Li1 LEE.

	Value	Uncertainty	Units
a	4.7×10^8	$\pm 7.3 \times 10^8$	$(\text{keV} \cdot \text{kg} \cdot \text{day})^{-1}$
b	84	± 16	$(\text{keV})^{-1}$
c	162	± 41	$(\text{keV}^{(1-d)} \cdot \text{kg} \cdot \text{day})^{-1}$
d	1.2	± 0.2	

binned spectrum for the Li1 LEE are summarized in Table I to make a comparison with spectra obtained from other measurements possible.

The region of interest for a DM analysis is defined using the light yield parameter (LY)

$$\text{LY} = \frac{E_l}{E_p}, \quad (2)$$

which quantifies the collected scintillation light from an individual event. Here, E_l is the energy of the light channel in *ee*-energy units, and E_p is the energy of the phonon channel in total energy units. Note that our definition of the LY automatically normalizes it to one for recoils induced by the iron source. The amount of produced scintillation photons in the target is quenched for nuclear recoils, with respect to electron and gamma recoils (EM recoils). We use this information to suppress the EM background. The quenching factor is measured *in situ* with the neutron calibration data. The exposure of the neutron calibration dataset is 0.178 kg days. The same analysis chain for the blind dataset has been applied to the neutron calibration data except that no coincidence cuts were applied, to keep higher statistics.

Figure 6 shows the LY versus energy from neutron calibration and blind data. The nuclear recoils are quenched

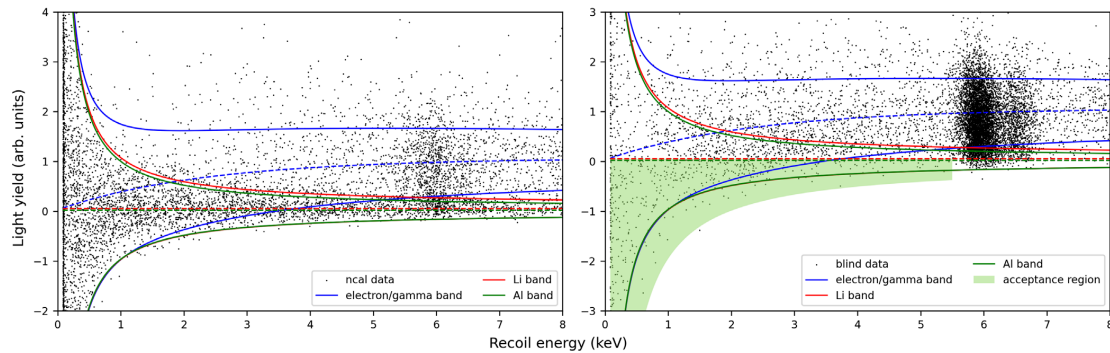


FIG. 6. Fitted light yield bands as a function of the recoil energy in the Li1 neutron (left) and blind (right) datasets, after application of the selection criteria discussed in Sec. III C. Electron/ γ (blue) and nuclear recoils off the nuclei with odd proton number (lithium red, aluminium green) cluster in bandlike structures and are fitted with Gauss distributions, with energy-dependent means and standard deviations. The acceptance region for DM candidates (light green) is chosen as the lower half of the lithium and aluminium bands, mitigating the EM background.

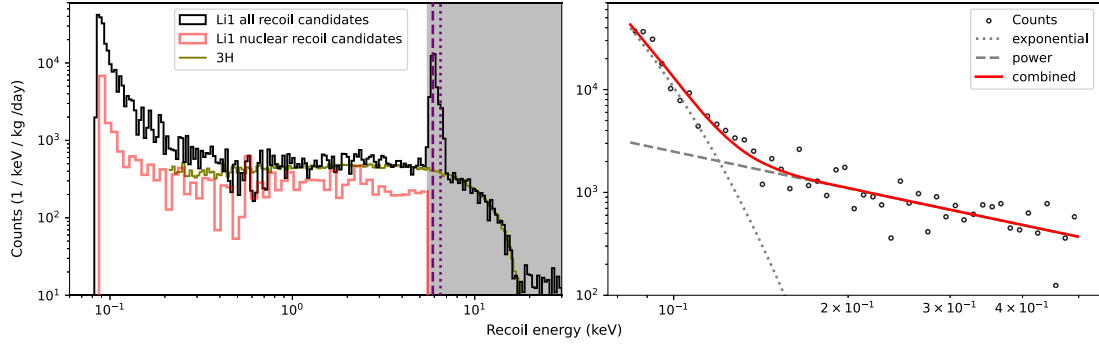


FIG. 7. Recoil energy spectrum of particle events inside the target of Li1. Left: the recoil spectrum up to 30 keV (black), the ROI for the DM search ends at 5.5 keV, indicated by the gray shade. The choice of the ROI is motivated in the text. The three prominent contributions are the clearly visible iron line (purple dashed, K- α ; purple dotted, K- β), the tritium background (olive line to guide the eye), and the LEE. The events within the acceptance region are considered nuclear recoil candidates (red). Right: the region below 0.5 keV, which is dominated by the LEE. The recoil energy spectrum of all recoil candidate events (black dots) can be fitted with the sum of an exponential (gray, dotted) and a power law component (gray, dashed).

according to the mass of the nucleus which they scatter off. For the two lithium isotopes only one band is drawn since no big difference is expected due to the negligible difference in masses. The oxygen band is not drawn, because it overlaps almost fully with the aluminium band. We can clearly identify the band of neutrons which scatter on nuclei, while the EM band is wider and less prominently pronounced. However, the light yield of the iron source, which builds a clearly visible cluster around 6 keV, indicates the position of the EM bands. To quantify the position of the nuclear recoil bands an unbinned likelihood fit of the recoil bands is performed: each band is described by a Gaussian distribution with energy-dependent mean and standard deviation. Their parametrization is nontrivial and described in detail in Ref. [27]. The bands plotted in Fig. 6 correspond to the 80% central interval of the Gauss function. The lower half of the lithium nuclear recoil band is defined as the region of interest (ROI, acceptance region) for the DM search, as a trade-off between efficiency and background minimization. Our ROI ends below the iron line, i.e. it extends from the trigger threshold of 83.60 eV (Li1) and 94.09 eV (Li2) to 5.5 keV. We do not consider higher recoil energies for our DM search for two reasons: first, the region does not show a significant signal expectation for recoils from sub-GeV/ c^2 DM particles, and second, it is dominated by the contribution from the iron source. The resulting energy spectrum of events that fall in the ROI is shown in Fig. 7 (left, red).

IV. DARK MATTER RESULTS

In order to calculate the upper limit for spin-dependent DM-nucleon interactions, we work in the limit of zero momentum transfer and thus neglect the form factors. The

expected different recoil rate for the proton/neutron *only* spin-dependent DM interactions is given by

$$\frac{dR}{dE_R} = \frac{2\rho_0}{m_\chi} \sigma_{p/n}^{SD} \sum_{i,T} f_{i,T} \left(\frac{J_{i,T} + 1}{3J_{i,T}} \right) \left(\frac{\langle S_{p/n,i,T} \rangle^2}{\mu_{p/n}^2} \right) \eta(v_{\min}), \quad (3)$$

where E_R is the recoil energy, ρ_0 is the local DM density, m_χ is the WIMP mass, and $\sigma_{p/n}^{SD}$ is the reference DM-proton/neutron cross section. The parameter $f_{i,T}$ is the fraction of each nucleus in the target scaled by its mass and is given by

$$f_{i,T} = \frac{n_T \zeta^i m_T^i}{\sum_{i,T} n_T \zeta^i m_T^i}, \quad (4)$$

where n_T is the multiplicity of nucleus T , ζ^i is the natural abundance of isotope i , and m_T^i is its mass. It should be noted that we consider $f_{\text{oxygen}} = 0$, i.e. we do not include the contribution from oxygen in the spin-dependent interaction. The reason for this is very low natural abundance of ^{17}O (i.e. 0.0367%) and thus including it changes the expected DM rate only negligibly. Furthermore, $J_{i,T}$ is the nuclear ground state angular momentum of the isotope i of nucleus T ; $\langle S_{p/n,i,T} \rangle$ is the expected value of the proton/neutron spins in the target isotope i of nucleus T and $\mu_{p/n}^2$ is the nucleon-DM reduced mass, and $\eta(v_{\min})$ is the mean inverse velocity in the standard model halo [28] where v_{\min} is the minimum velocity required to produce a nuclear recoil of energy E_R [29]. This formalism is equivalent to the one that was employed in our previous work [5].

We adopt the standard DM halo model that assumes a Maxwellian velocity distribution and a local DM density of

$\rho_{\text{DM}} = 0.3 \text{ (GeV}/c^2\text{)}/\text{cm}^3$ [30], the Galactic escape velocity at the position of the Sun of $v_{\text{esc}} = 544 \text{ km/s}$ [31], and the solar orbital velocity of $v_{\odot} = 220 \text{ km/s}$ [32]. For the calculation of neutron- and proton-only limits, we use $\langle S_n \rangle = \langle S_p \rangle = 0.472$ for ${}^6\text{Li}$ [33], $\langle S_p \rangle = 0.497$ for ${}^7\text{Li}$ [34], and $\langle S_n \rangle = 0.0296$, $\langle S_p \rangle = 0.343$ for ${}^{27}\text{Al}$ [35].

For the calculation of DM exclusion limits it needs to be understood what a DM signal would look like after application of our analysis chain. For this, the input simulated spectrum discussed in Sec. III D is reweighted such that it resembles the expected recoil spectrum from each DM mass. The resulting recoil spectrum seen after triggering, applying data quality cuts, and energy reconstruction in the same way it is done for the blind set, automatically includes the information about the detector resolution and threshold. Thus, an *observed* energy spectrum for a given *injected* spectrum is obtained. We additionally remove events where the reconstructed amplitudes differ from the injected amplitude by more than 3 times the detector resolution. This is done in order to avoid any nonphysical reconstruction of subthreshold events if they happen to pile up with exceptionally strong upward fluctuations of the noise baseline. The same formalism was also employed and discussed in our previous work [4].

The choice of ROI is motivated in Sec. III E, where we define our candidate events. A similar procedure was used for

the calculation of the limits from the Li2 blind data except that no band fit could be employed. The exclusion limits are finally calculated using Yellin's optimum interval method [36,37] to extract the upper limit on the cross section of DM particles with ${}^6\text{Li}$ along with ${}^7\text{Li}$ and ${}^{27}\text{Al}$. Limits on the spin-dependent reference cross section for proton/neutron-only interaction are shown in Fig. 8 for DM masses from 0.16 to 6 GeV/c^2 , for both the modules, and compared with those from other experiments. These results are reported using Yellin's optimum interval method to extract the 90% confidence level upper limits. We can see around 3–4 orders of magnitude improvement in both proton and neutron limits for the entire probed mass range, compared to our previous test done with the same material in the aboveground facility with a higher energy threshold and lower exposure [7]. The Li1 module provides up to an order of magnitude better results than the Li2 module because of the additional scintillation light information. For very low masses, which are dominated by the LEE that cannot be discriminated from nuclear recoils, the difference is negligible. For the proton-only interactions, we improve the existing limits from 0.25 to 2.5 GeV/c^2 by up to a factor of 2.5 compared to other experiments. For the neutron-only interactions, we achieve the strongest limit between 0.16 and 1.5 GeV/c^2 , more than an order of magnitude better than the limits from our 2019 results using ${}^{17}\text{O}$ [4].

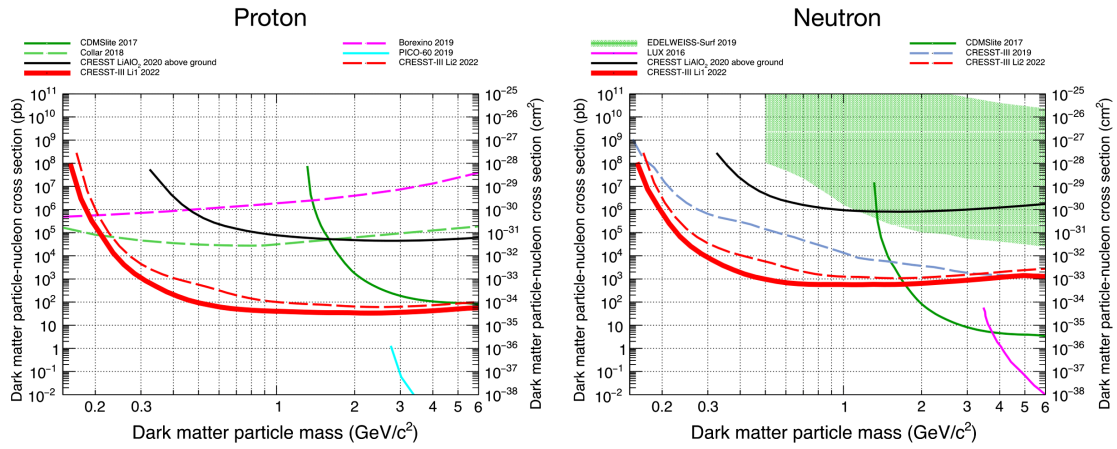


FIG. 8. The exclusion limits for proton-only (left) and neutron-only (right) spin-dependent DM-nucleon cross sections versus DM particle mass set by various experiments compared with the two lithium modules described in this work with ${}^6\text{Li}$, ${}^7\text{Li}$, and ${}^{27}\text{Al}$. This work gives the most stringent limits between 0.25 and 2.5 GeV/c^2 for proton only and between 0.16 and 1.5 GeV/c^2 for neutron-only interactions. The solid red line shows the Li1 limits which includes the scintillation light information and the dashed red line shows the Li2 limits where no light information was available (hence worse). The previous aboveground results from CRESST using the same detector material and procedure with higher threshold and lower exposure are also shown with the solid black line [7]. Also, CRESST-III 2019 results for neutron-only interactions using ${}^{17}\text{O}$ are shown also with the dashed light-blue line (right) [4]. Additionally, we show the limits from other experiments: EDELWEISS [38] and CDMSlite with ${}^{73}\text{Ge}$ [39], PICO with ${}^{19}\text{F}$ [40], LUX [41] which use ${}^{129}\text{Xe} + {}^{131}\text{Xe}$, J. I. Collar with ${}^1\text{H}$ [42], and the constraint derived in [43] from Borexino.

V. CONCLUSION

In this work we present the detailed analysis and results of two lithium-based cryogenic detectors operated in the underground facility of the CRESST experiment at LNGS. We highlight the results of the best performing one and validate its analysis with the result of a second, identically manufactured detector. The best performing one achieves a threshold of 83.60 eV that corresponds to sensitivities down to a DM mass of 0.16 GeV/ c^2 . We have probed spin-dependent DM particle interactions with nuclei, distinguishing proton- and neutron-only interactions. For proton-only interactions, leading exclusion limits for the mass region between 0.25 and 2.5 GeV/ c^2 are presented. Additionally, for neutron-only interactions, best sensitivity was achieved in the mass range of 0.16 and 1.5 GeV/ c^2 .

The results of this run showed that LiAlO₂ is an excellent material to study spin-dependent interactions and will therefore be included in future CRESST projects. Below DM masses of 0.6 GeV/ c^2 the limit-setting power of the CRESST lithium detector modules decreases. The reason

for this is an excess of events at low energies. The source of these is currently under investigation.

ACKNOWLEDGMENTS

We are grateful to LNGS for their generous support of CRESST. This work has been funded by the Deutsche Forschungsgemeinschaft (DFG, German Research Foundation) under Germany's Excellence Strategy—EXC 2094–390783311 and through the Sonderforschungsbereich (Collaborative Research Center) SFB1258 “Neutrinos and Dark Matter in Astro- and Particle Physics,” by the BMBF 05A20W01 and 05A20VTA and by the Austrian Science Fund (FWF): I5420-N, W1252-N27, and FG1 and by the Austrian research promotion agency (FFG), project ML4CPD. The Bratislava group acknowledges a partial support provided by the Slovak Research and Development Agency (project APVV-15-0576). The computational results presented were partially obtained using the Vienna CLIP cluster and the Munich MPCDF.

-
- [1] M. W. Goodman and E. Witten, *Phys. Rev. D* **31**, 3059 (1985).
- [2] G. Jungman, M. Kamionkowski, and K. Griest, *Phys. Rep.* **267**, 195 (1996).
- [3] B. W. Lee and S. Weinberg, *Phys. Rev. Lett.* **39**, 165 (1977).
- [4] A. H. Abdelhameed *et al.* (CRESST Collaboration), *Phys. Rev. D* **100**, 102002 (2019).
- [5] A. H. Abdelhameed *et al.* (CRESST Collaboration), *Eur. Phys. J. C* **79**, 630 (2019).
- [6] A. H. Abdelhameed *et al.* (CRESST Collaboration), *Eur. Phys. J. C* **80**, 834 (2020).
- [7] G. Angloher *et al.*, *Eur. Phys. J. C* **82**, 207 (2022).
- [8] J. Meija *et al.*, *Pure Appl. Chem.* **88**, 293 (2016).
- [9] T. Yanagida, Y. Fujimoto, M. Koshimizu, N. Kawano, G. Okada, and N. Kawaguchi, *J. Phys. Soc. Jpn.* **86**, 094201 (2017).
- [10] M. Ambrosio *et al.*, *Phys. Rev. D* **52**, 3793 (1995).
- [11] M. Aglietta *et al.* (LVD Collaboration), *Phys. Rev. D* **58**, 092005 (1998).
- [12] M. Schumann, *J. Phys. G* **46**, 103003 (2019).
- [13] G. Angloher *et al.*, *Astropart. Phys.* **23**, 325 (2005).
- [14] G. Angloher, M. Bauer, I. Bavykina, A. Bento, A. Brown, C. Bucci, C. Ciemiak, C. Coppi, G. Deuter, and F. von Feilitzsch, *Astropart. Phys.* **31**, 270 (2009).
- [15] F. Pröbst, M. Frank, S. Cooper, P. Colling, D. Dummer, P. Ferger, G. Forster, A. Nucciotti, W. Seidel, and L. Stodolsky, *J. Low Temp. Phys.* **100**, 69 (1995).
- [16] D. Baxter *et al.*, *Eur. Phys. J. C* **81**, 907 (2021).
- [17] E. Gatti and P. F. Manfredi, *Riv. Nuovo Cimento* (1978–1999) **9**, 1 (1986).
- [18] C. Alduino *et al.*, *Eur. Phys. J. C* **77**, 857 (2017).
- [19] M. Mancuso, A. Bento, N. F. Iachellini, D. Hauff, F. Petricca, F. Pröbst, J. Rothe, and R. Strauss, *Nucl. Instrum. Methods Phys. Res., Sect. A* **940**, 492 (2019).
- [20] M. Stahlberg, Probing low-mass dark matter with CRESST-III data analysis and first results, Ph.D. thesis, Technische Universität Wien, 2020.
- [21] F. Wagner, D. Bartolot, D. Rizvanovic, F. Reindl, J. Schieck, and W. Waltenberger, *arXiv:2207.02187*.
- [22] P. M. M. Bauer, Data analysis for the CRESST experiment: New methods, improved alpha analysis, and results on light dark matter and backgrounds, Ph.D. thesis, Technische Universität München, 2020.
- [23] P. Adari *et al.*, *SciPost Phys. Proc.* **9**, 001 (2022).
- [24] N. Kurinsky, D. Baxter, Y. Kahn, and G. Krnjaic, *Phys. Rev. D* **102**, 015017 (2020).
- [25] M. Heikinheimo, S. Sassi, K. Nordlund, K. Tuominen, and N. Mirabolfathi, *Phys. Rev. D* **106**, 083009 (2022).
- [26] P. Abbamonte, D. Baxter, Y. Kahn, G. Krnjaic, N. Kurinsky, B. Mandava, and L. K. Wagner, *Phys. Rev. D* **105**, 123002 (2022).
- [27] D. Schmiedmayer, Calculation of dark-matter exclusion-limits using a maximum likelihood approach, Master's thesis, Technische Universität Wien, 2019.
- [28] K. Freese, M. Lisanti, and C. Savage, *Rev. Mod. Phys.* **85**, 1561 (2013).
- [29] S. K. Lee, M. Lisanti, S. Mishra-Sharma, and B. R. Safdi, *Phys. Rev. D* **92**, 083517 (2015).
- [30] P. Salucci, F. Nesti, G. Gentile, and C. Frigerio Martins, *Astron. Astrophys.* **523**, A83 (2010).
- [31] M. C. Smith *et al.*, *Mon. Not. R. Astron. Soc.* **379**, 755 (2007).
- [32] F. J. Kerr and D. Lynden-Bell, *Mon. Not. R. Astron. Soc.* **221**, 1023 (1986).

G. ANGLOHER *et al.*PHYS. REV. D **106**, 092008 (2022)

- [33] A. Gnech, M. Viviani, and L. E. Marcucci, *Phys. Rev. C* **102**, 014001 (2020).
- [34] A. F. Pacheco and D. Strottman, *Phys. Rev. D* **40**, 2131 (1989).
- [35] J. Engel, M. T. Ressell, I. S. Towner, and W. E. Ormand, *Phys. Rev. C* **52**, 2216 (1995).
- [36] S. Yellin, *Phys. Rev. D* **66**, 032005 (2002).
- [37] S. Yellin, arXiv:0709.2701.
- [38] E. Armengaud *et al.* (EDELWEISS Collaboration), *Phys. Rev. D* **99**, 082003 (2019).
- [39] R. Agnese *et al.* (SuperCDMS Collaboration), *Phys. Rev. D* **97**, 022002 (2018).
- [40] C. Amole *et al.* (PICO Collaboration), *Phys. Rev. D* **100**, 022001 (2019).
- [41] D. S. Akerib *et al.* (LUX Collaboration), *Phys. Rev. Lett.* **118**, 251302 (2017).
- [42] J. I. Collar, *Phys. Rev. D* **98**, 023005 (2018).
- [43] T. Bringmann and M. Pospelov, *Phys. Rev. Lett.* **122**, 171801 (2019).


Eur. Phys. J. C (2022) 82:851
<https://doi.org/10.1140/epjc/s10052-022-10829-5>

THE EUROPEAN
 PHYSICAL JOURNAL C



Letter

A low-threshold diamond cryogenic detector for sub-GeV dark matter searches

A. H. Abdelhameed¹, G. Angloher¹, A. Bento^{1,2}, E. Bertoldo^{1,3}, A. Bertolini¹, L. Canonica^{1,4} , N. Ferreiro Iachellini¹, D. Fuchs¹, A. Garai¹, D. Hauff¹, A. Nilima¹, M. Mancuso¹, F. Petricca¹, F. Pröbst¹, F. Pucci¹, J. Rothe^{1,4}

¹ Max-Planck-Institut für Physik, 80805 Munich, Germany

² LIBPhys-UC, Departamento de Física, Universidade de Coimbra, 3004 516 Coimbra, Portugal

³ Present Address: Institut de Física d'Altes Energies (IFAE), Barcelona Institute of Science and Technology (BIST), 08193 Bellaterra, Barcelona, Spain

⁴ Present Address: Physik-Department and Excellence Cluster Universe, Technische Universität München, 85748 Garching, Germany

Received: 24 March 2022 / Accepted: 21 September 2022 / Published online: 30 September 2022
 © The Author(s) 2022

Abstract In this work we report the realization of the first low-threshold cryogenic detector that uses diamond as absorber for astroparticle physics applications. We tested two 0.175 g CVD diamond samples, each instrumented with a W-TES. The sensors showed transitions at about 25 mK. We present the performance of the diamond detectors and we highlight the best performing one, where we obtained an energy threshold as low as 16.8 eV. This promising result lays the foundation for the use of diamond for different fields of applications where low threshold and excellent energy resolution are required, as i.e. light dark matter searches and BSM physics with coherent elastic neutrino nucleus scattering.

1 Introduction

It is undeniable that the identification of dark matter (DM) is one of the most urgent open questions in physics today. Several observational evidences based on gravitational effects (i.e. anisotropies in the cosmic microwave background, large-scale structure distributions, galaxy cluster velocity dispersions, gravitational lensing effect) support the assumption that 26% of the mass-energy density in the Universe is in the form of non-barionic and cold DM. For recent reviews see, e.g., [1, 2]. However, despite the world-wide efforts and the tremendous experimental progresses, the nature of DM is still unresolved. A standard approach in the field of direct DM searches is to look for the scattering of hypothetical DM particles with the atomic nuclei of target materials, contained in low-background experiments typically located in underground laboratories. One of the crucial parameters in

direct DM experiments is the energy threshold, since it drives the sensitivity to the detection of low-energy nuclear recoils induced by DM interactions. While the elastic scattering of DM particles with masses above a few GeVs can be easily accessed by experiments using large TPCs filled with noble-liquids (Argon [3, 4] and Xenon [5–7]), light DM particles with masses in the sub-GeV range are not accessible to these experiments due to the kinematics of the process. Simply, light DM particles, that interact with Ar or Xe nuclei, induce nuclear recoils that are below the experimental threshold. Recently, the Migdal effect [8, 9] has been proposed to extend the reach of these experiments to sub-GeV DM masses [10, 11], but the existence of this effect has still to be experimentally demonstrated. An experimental technique complementary to TPCs is the one of cryogenic detectors. They enable the reach of low-energy thresholds by means of detecting of the phonons created following the particle interaction with the crystalline detector nuclei. As of today, Si [12], Ge [13] and CaWO₄ [14] crystals are the targets most widely used in state-of-the art experiments for direct DM searches. For the read-out of the tiny temperature variations induced by particle interactions, the crystal targets must be instrumented with highly sensitive temperature sensors. Among the available thermometers, Transition Edge Sensors using W films [15] and Neutron Transmutation Doped thermistors [16] have the properties that fulfill the requirements of a sub-GeV DM experiment, having obtained energy thresholds of $O(10 \text{ eV})$. Thanks to their performance, cryogenic detector are currently leading the sensitivity of spin-independent DM-nucleons interactions for DM masses below few GeV [12–14]. However, to further extend the reach of cryogenic experiments and explore new region of parameters of lighter

^a e-mail: canonica@mpp.mpg.de (corresponding author)

DM particles, experimental thresholds as low as few eV are required.

Diamond targets have the potential to reach such a low energy threshold thanks to their superior thermal properties [17] and only recently it has been proposed as detection medium for sub-GeV DM searches [18]. Despite the outstanding thermal properties, diamond has not been operated as a cryogenic absorber for astroparticle physics applications until recently. This was mainly due to the limited availability of cheap, high-purity and large-size single crystal (SC) diamonds on the market. Our group has already reported the first operation of a diamond cryogenic absorber equipped with a W-TES, but due to the poor performance of the setup, it was not possible to obtain any information on the threshold achieved by the prototype [19]. Here we report the results on the cryogenic performance of a new prototype realized with a synthetic SC diamond equipped with a W-TES. We achieved a detector energy threshold of 16.8 eV. This result opens a wealth of opportunities for using high-purity lab-grown diamonds in field of light DM particle searches, but also for other sectors where low energy thresholds are needed (i.e. coherent elastic neutrino nucleus scattering). The low-threshold achieved will allow to study new properties of DM with the data presented in this work. We leave this topic for a future publication that is currently in preparation.

2 Diamond as cryogenic target for DM detection

Cryogenic calorimeters have been developed to explore different sectors of particle physics and astrophysics, from direct DM searches [12–14], to neutrinoless double beta decay [20–22] and neutrino mass measurements [23, 24]. One of their characteristics is that they can be realized with many different materials, with the only requirement to have crystalline structure with low enough heat capacity at the operating temperature $O(10$ mK).

The Debye temperature of diamond, that can be used as a figure of merit of the thermal properties of the material [25], is among the highest available in nature (2220 K) and it is significantly higher than other established target materials used in DM direct detection experiments (e.g. 645 K for Si, 371 K for Ge and 250 K for CaWO_4). This parameter ensures high phonon density of states, that is key for achieving the ultimate sensitivity in the detection of small energy deposits. Moreover, diamond is made of light nuclei ($Z = 6$) and this ensures a good match in the kinematics of the interaction of the light DM particle. A complete review of the properties of diamond as cryogenic sub-GeV DM detector can be found in [18].

Thanks to the developments in the synthetic grown diamond technologies of the last decades, the barrier of the availability of high-quality crystals has been overcome. We can

nowadays easily find on the market SC crystals grown using the Chemical Vapour Deposition (CVD) technology [26]. In this technique the crystal is grown starting from a source gas (typically methane) that is deposited over a proper seed substrate. The samples used in this work have been realized using the heteroepitaxial technique on a foreign multilayer substrate made of Ir/YSZ/Si [27]. This, in contrast to the homoepitaxial technique, does not require the use of a diamond seed to start the growth process. However, it requires only a lattice-matched substrate, enabling the growth of large volume diamonds more easily.

3 Experimental setup

In this work, the crystals used as absorbers are made by two identical SC diamond samples of 0.175 g each and $(2 \times 5 \times 5)$ mm³, grown at AuDiaTec [28]. To detect the phonons produced in the absorber following a particle interaction, both crystals are instrumented with a W-TES. The TES design is very similar to the ones used for the CRESST-III experiment [29]. They are made of a thin strip of W with two large Al pads partially overlapping the W layer. These Al pads have two different features: they serve as phonon collectors [15] and as ohmic contacts. They are connected via a pair of 25 μm Al bond wires through which the bias current is injected. The W film is also connected by a long and thin strip of Au to a thicker Au bond pad on which a 25 μm Au wire is bonded. This connection serves as weak thermal link between the sensor and the heat bath at ~ 10 mK. On the same surface, but separated from the TES, we also evaporated a heater. The heater is made of a thin strip of Au with two Al pads deposited on top. These pads are also bonded with a pair of 25 μm Al bond wires through which a tunable current can be injected to maintain the TES at the desired operating temperature. The heater is also used to inject artificial pulses to monitor the detector response over time and to refine the energy calibration during data analysis. In Fig. 1 (top) we show one of the two diamond crystals after the TES fabrication.

Each of the two diamond crystals is housed in a Cu structure, held in position by a pair of bronze clamps (see Fig. 1 (bottom)). Four sapphire balls sitting on the Cu holder are used as spacers and provide a point-like contact between the crystal and the holder itself. At a distance of about 0.5 cm from the crystal, a ⁵⁵Fe source (activity ~ 0.3 Bq) is installed for calibration purposes. The samples were cooled down in a dilution refrigerator at the Max Planck institute for Physics in Munich, Germany, in a surface building, using a Kelvinox-400HA dilution refrigerator from Oxford Instruments (see [30] and references therein for details of the cryogenic infrastructure). Electrical connections to the TES were made by superconducting NbTi twisted pairs wires. The TES read-

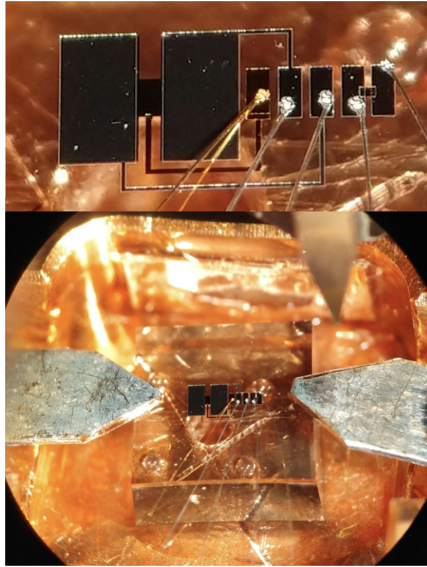


Fig. 1 Top: Picture of the TES sensor fabricated on one of the two diamond crystals. On the left, it is possible to see two large aluminum areas (0.5×1) mm² evaporated on top of a darker strip of tungsten (140×300) μ m². A 50 nm thick and 1.5 mm long strip of gold connects the tungsten layer to a 40 μ m thick gold pad, to which we bond a 25 μ m gold wire; this gold wire provides a weak thermal coupling to the heat bath at ~ 10 mK. On the right part of the picture, there is the heater: this is made of a 50 nm thick strip of gold with two aluminum pads deposited on top. Bottom: One of the two diamond crystals instrumented with the TES and housed in the copper structure

out circuit uses a reference resistor at mK and a commercial SQUID system sensor as front end amplifier, combined with a CRESST-like detector control system [31]. The two detectors were readout using an Applied Physics System model 581 DC SQUID.

4 Measurement and data processing

During the cryogenic measurement, the diamond samples were measured simultaneously in a stable working point for 58.4 h. We collected statistics for a total exposure of 4.3×10^{-4} kg-d. The TESs showed a superconducting transition at about 25 mK. In the following, the data sets acquired with the diamond samples #1 and #2 are referred to as data set 1 and 2 respectively.

Given the small size of the samples and the limited dynamic range of the TESs, a sub-set of measurements was carried out in under-performing conditions. The goal was to extend the sensor dynamic range such that events from the ⁵⁵Fe at 5.9 keV were clearly visible and could be used

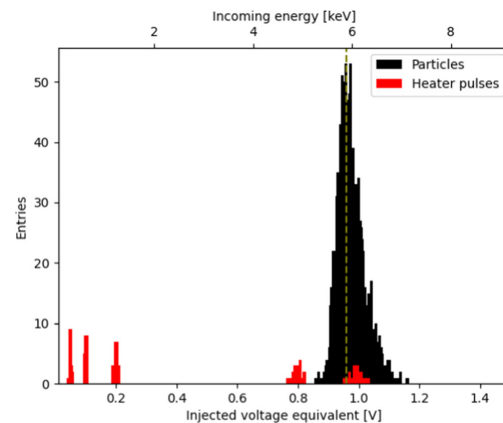


Fig. 2 Events coming from the iron source (black) in the energy region 5.2 keV–7 keV and events coming from the artificial pulses sent by a heater (red) in the calibration data set for module number 1 (duration 17.7 h)

for calibration purposes. The artificial pulses sent through the heater during this measurement were used to calculate the conversion factor between the deposited energy and the injected heater voltage in the entire energy range from threshold up to the iron energy region. Thanks to this calibration of the heater response, we were able to reconstruct the energy scale also in different operational conditions, namely during the full data set acquired with the optimized settings. As an example, events from the ⁵⁵Fe source and from the artificial pulses injected through the heater are shown in Fig. 2 for detector 1.

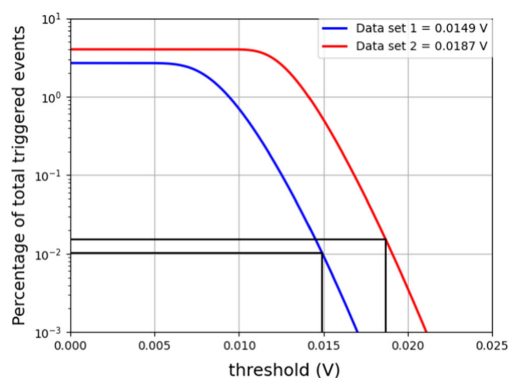
After the data set for calibration was acquired, the detectors were operated at their optimal operating point, focusing on achieving a low energy threshold. Data were acquired in a continuously recorded stream and processed with a software trigger after data taking [30].

Triggered events were filtered with an *optimum filter* [32] algorithm which improves the reconstruction of the amplitude of a pulse with a given pulse shape in the presence of noise. The noise conditions of each detector were inferred from empty traces which were acquired with the continuous recording process. For the representation of the pulse shape, we created a standard event (SEV) by averaging a selection of clean particle events. Following the directions described in [33], the SEV could be used to reproduce the shape of the acquired pulses at different energies.

With the aim of estimating the noise level of the baselines of each detector, we superimposed the SEV with a fixed amplitude on a set of empty traces. The distribution of this amplitude evaluated with the filter was then fitted with a Gaussian function. The sigma of this distribution was used

Table 1 Values for threshold and baseline resolution of the two data sets. Each value is shown in mV and in eV

Data set	1	2
Baseline resolution (mV)	2.68	3.81
Baseline resolution (eV)	3.54	3.42
Threshold (mV)	14.9	18.7
Threshold (eV)	19.7	16.8

**Fig. 3** Threshold evaluation of the two sets of data. The threshold is estimated with a function that gives the number of noise triggers for a given threshold (see [34] for details). The thresholds that have been calculated are 14.9 mV for data set 1 and 18.7 mV for data set 2. Taking into account the calibration functions, they correspond to 19.7 eV and 16.8 eV respectively

to determine the resolution of the baseline. The obtained values in Volt and their respective calibrated values in eV can be found in Table 1 for the two diamond samples.

Following the approach described in [34], the threshold was computed accepting a fixed number of noise triggers for exposure units which is negligible compared to the particle event rate. For this analysis in both modules the number of accepted noise trigger events is around 1% of the total number of triggered events. The final threshold values obtained with this method can be inferred from Fig. 3, where the noise trigger curves are shown as a function of the trigger threshold. Taking into account the calibration factors, these threshold values correspond to 19.7 eV and 16.8 eV for data set 1 and data set 2, respectively.

This result, although obtained with a prototype, shows for the first time the excellent performance of diamond when operated as cryogenic detector. We believe that future work on the optimization of the W-TES design to better match the properties of thermal signals in diamonds will allow for further reduction of the energy threshold, making the goal of reaching $O(eV)$ values within reach.

5 Conclusions

This work shows the advanced performance achieved with two detectors made of diamonds operated as cryogenic detectors. The results presented in this work represent a major milestone for future sub-GeV DM investigations, since the low-energy thresholds achieved with these prototypes already compete with the most advanced detector currently operating in the field of light DM searches. A dedicated future work on the exploration of new region of the parameter space for DM interactions with regular matter obtained with the data presented in this work is currently under preparation.

Acknowledgements This research was supported by the Excellence Cluster ORIGINS which is funded by the Deutsche Forschungsgemeinschaft (DFG, German Research Foundation) under Germany's Excellence Strategy - EXC-2094-390783311.

Data Availability Statement This manuscript has no associated data or the data will not be deposited. [Authors' comment: The datasets analysed during the current study are available from the corresponding author on reasonable request.]

Open Access This article is licensed under a Creative Commons Attribution 4.0 International License, which permits use, sharing, adaptation, distribution and reproduction in any medium or format, as long as you give appropriate credit to the original author(s) and the source, provide a link to the Creative Commons licence, and indicate if changes were made. The images or other third party material in this article are included in the article's Creative Commons licence, unless indicated otherwise in a credit line to the material. If material is not included in the article's Creative Commons licence and your intended use is not permitted by statutory regulation or exceeds the permitted use, you will need to obtain permission directly from the copyright holder. To view a copy of this licence, visit <http://creativecommons.org/licenses/by/4.0/>.

Funded by SCOAP³. SCOAP³ supports the goals of the International Year of Basic Sciences for Sustainable Development.

References

1. R. Massey, T. Kitching, J. Richard, Rep. Prog. Phys. **73**, 086901 (2010)
2. P. Salucci, Found. Phys. **48**, 1517 (2018)
3. DarkSide Collaboration, P. Agnes et al., Phys. Rev. D **98**, 102006 (2018)
4. DEAP-3600 Collaboration, R. Ajaj et al., Phys. Rev. D **100**, 022004 (2019)
5. LUX Collaboration, D.S. Akerib et al., Phys. Rev. Lett. **118**, 021303 (2017)
6. PandaX-II Collaboration, X. Cui et al., Phys. Rev. Lett. **119**, 181302 (2017)
7. XENON Collaboration, E. Aprile et al., Phys. Rev. Lett. **121**, 111302 (2018)
8. M.J. Dolan et al., Phys. Rev. Lett. **121**, 101801 (2018)
9. M. Ibe et al., J. High Energy Phys. **2018**, 194 (2018)
10. XENON Collaboration, E. Aprile et al., Phys. Rev. Lett. **123**, 241803 (2019)
11. CDEX Collaboration, Z.Z. Liu et al., Phys. Rev. Lett. **123**, 161301 (2019)

12. SuperCDMS Collaboration, I. Alkhatib et al., *Phys. Rev. Lett.* **127**, 061801 (2021)
13. EDELWEISS Collaboration, E. Armengaud et al., *Phys. Rev. D* **99**, 082003 (2019)
14. CRESST Collaboration, A.H. Abdelhameed et al., *Phys. Rev. D* **100**, 102002 (2019)
15. K.D. Irwin et al., *Rev. Sci. Instrum.* **66**, 5322 (1995)
16. S. Pirro, P. Mauskopf, *Annu. Rev. Nucl. Part. Sci.* **67**, 161 (2017)
17. W. Saslow et al., *Phys. Rev. Lett.* **16**, 354 (1966)
18. N. Kurinsky et al., *Phys. Rev. D* **99**, 123005 (2019)
19. L. Canonica et al., *J. Low Temp. Phys.* **199**, 606 (2020)
20. CUORE Collaboration, C. Alduino et al., *Phys. Rev. Lett.* **120**, 132501 (2018)
21. CUPID-0 Collaboration, O. Azzolini et al., *Phys. Rev. Lett.* **120**, 232502 (2018)
22. AMoRE Collaboration, V. Alenkov et al., *Eur. Phys. J. C* **79**, 791 (2019)
23. ECHo Collaboration, L. Gastaldo et al., *Eur. Phys. J. Spec. Top.* **226**, 1623 (2017)
24. HOLMES Collaboration, A. Giachero et al., *J. Instrum.* **12**, C02046 (2017)
25. C. Kittel, *Introduction to Solid State Physics* (Wiley Eastern, New Delhi, 1974)
26. P.M. Martin, *Handbook of Deposition Technologies for Films and Coatings*, 3rd edn. (William Andrew Publishing, Boston, 2010)
27. M. Schreck et al., *Sci. Rep.* **7**, 44462 (2017)
28. <https://www.audiatec.de/>. Accessed 22 Sep 2022 17:52:13
29. J. Rothe et al., *J. Low Temp. Phys.* (2018)
30. CRESST Collaboration, G. Angloher et al., *Eur. Phys. J. C* **77**, 637 (2017)
31. CRESST Collaboration, G. Angloher et al., *Astropart. Phys.* **31**, 270 (2009)
32. E. Gatti, P.F. Manfredi, *La Rivista del Nuovo Cimento* (1978–1999) **9**, 1 (1986)
33. F. Pröbst et al., *J. Low Temp. Phys.* **100**, 69 (1995)
34. M. Mancuso et al., *Nucl. Instrum. Methods Phys. Res. Sect. A* **940**, 492. [arXiv:1711.11459](https://arxiv.org/abs/1711.11459) (2019)



Light dark matter search using a diamond cryogenic detector

CRESST Collaboration

G. Angloher¹, S. Banik^{2,3}, G. Benato⁴, A. Bento^{1,9}, A. Bertolini^{1,a}, R. Breier⁵, C. Bucci⁴, J. Burkhart², L. Canonica^{1,13,b}, A. D'Addabbo⁴, S. Di Lorenzo¹, L. Einfeldt^{2,3}, A. Erb^{6,10}, F. v. Feilitzsch⁶, S. Fichtinger², D. Fuchs¹, A. Garai¹, V. M. Ghete², P. Gorla⁴, P. V. Guillaumon⁴, S. Gupta², D. Hauff¹, M. Jeřkovský⁵, J. Jochum⁷, M. Kaznacheeva⁶, A. Kinast⁶, H. Kluck², H. Kraus⁸, S. Kuckuk⁷, A. Langenkämper¹, M. Mancuso¹, L. Marini^{4,11}, B. Mauri¹, L. Meyer⁷, V. Mokina², M. Olmi⁴, T. Ortmann⁶, C. Pagliarone^{4,12}, L. Pattavina^{4,6}, F. Petricca¹, W. Potzel⁶, P. Povinec⁵, F. Pröbst¹, F. Pucci¹, F. Reindl^{2,3}, J. Rothe⁶, K. Schäffner¹, J. Schieck^{2,3}, S. Schönert⁶, C. Schwertner^{2,3}, M. Stahlberg¹, L. Stodolsky¹, C. Strandhagen⁷, R. Strauss⁶, I. Usherov⁷, F. Wagner², M. Willers⁶, V. Zema¹

¹ Max-Planck-Institut für Physik, 80805 Munich, Germany² Institut für Hochenergiephysik der Österreichischen Akademie der Wissenschaften, 1050 Wien, Austria³ Atominstytut, Technische Universität Wien, 1020 Wien, Austria⁴ INFN, Laboratori Nazionali del Gran Sasso, 67100 Assergi, Italy⁵ Faculty of Mathematics, Physics and Informatics, Comenius University, 84248 Bratislava, Slovakia⁶ Physik-Department, TUM School of Natural Sciences, Technische Universität München, 85747 Garching, Germany⁷ Eberhard-Karls-Universität Tübingen, 72076 Tübingen, Germany⁸ Department of Physics, University of Oxford, Oxford OX1 3RH, UK⁹ Also at: LIBPhys-UC, Departamento de Física, Universidade de Coimbra, 3004 516 Coimbra, Portugal¹⁰ Also at: Walther-Meißner-Institut für Tieftemperaturforschung, 85748 Garching, Germany¹¹ Also at: GSSI-Gran Sasso Science Institute, 67100 L'Aquila, Italy¹² Also at: Dipartimento di Ingegneria Civile e Meccanica, Università degli Studi di Cassino e del Lazio Meridionale, 03043 Cassino, Italy¹³ Present address: INFN, Sezione di Milano LASA, Via Fratelli Cervi 201, Segrate, 20054 Milan, Italy

Received: 11 October 2023 / Accepted: 5 March 2024

© The Author(s) 2024

Abstract Diamond operated as a cryogenic calorimeter is an excellent target for direct detection of low-mass dark matter candidates. Following the realization of the first low-threshold cryogenic detector that uses diamond as absorber for astroparticle physics applications, we now present the resulting exclusion limits on the elastic spin-independent interaction cross-section of dark matter with diamond. We measured two 0.175 g CVD (Chemical Vapor Deposition) diamond samples, each instrumented with a Transition Edge Sensor made of Tungsten (W-TES). Thanks to the energy threshold of just 16.8 eV of one of the two detectors, we set exclusion limits on the elastic spin-independent interaction of dark matter particles with carbon nuclei down to dark matter masses as low as 0.122 GeV/c². This work shows the scientific potential of cryogenic detectors made from diamond and lays the foundation for the use of this material as target for direct detection dark matter experiments.

1 Introduction

Dark matter (DM) is one of the most investigated topics in astroparticle physics. Its presence is highly motivated by many observational evidences [1–3]. Many theories have been built around the idea of a particle-like DM, predicting candidates that cover an extended mass range. In the last decade cryogenic experiments have been very successful in reaching extremely low energy thresholds, taking on a crucial role in the exploration of DM in the GeV mass range and below. Among them, the Cryogenic Rare Event Search with Superconducting Thermometers (CRESST) experiment has recently gained sensitivity to DM masses of 0.115 GeV/c² with an energy threshold down to 10 eV in an underground measurement [4].

We have reported in a previous publication how a similar energy threshold was achieved in an above ground measure-

^a e-mail: anbertol@mpp.mpg.de (corresponding author)^b e-mail: canonica@mpp.mpg.de

ment employing diamond single crystals as detector material [5]. In this work we report limits on the elastic spin-independent DM-nucleon interactions using data obtained with these detectors. The experimental setup, data taking and energy calibration will be described very concisely in this work. For a more detailed description, we refer the reader to our previous work in [5].

2 Diamond as cryogenic detectors

Cryogenic calorimeters are used in many different fields of astroparticle physics. See [6] for a comprehensive review. The high interest in these devices can be attributed among others to the possibility of using different materials as energy absorbers, with the remarkable advantage that the most suitable material can be chosen depending on the particular research purpose [7]. With a Debye temperature of 2220 K and therefore a favorable phonon propagation, diamond crystals have the properties to be excellent absorbers for cryogenic calorimeters aiming at reaching low-energy thresholds. Additionally, the light nucleus of carbon ($A = 12$) allows to probe lower DM masses, being kinematically favored compared to heavier target nuclei. For a more detailed description of the advantages of using diamond for low mass DM searches, see [8,9].

In the following we present the results obtained using two diamond single crystals of 0.175 g and a size of $(2 \times 5 \times 5)$ mm³ each. In the following they will be referred to as *detector 1* and *detector 2*. Each crystal has been instrumented with a W-TES, with a design similar to the one used for the CRESST experiment: a thin strip of W and two larger Al pads that are partially covering the W layer. In the proximity of the W-TES, an ohmic heater (Au film) is used to inject artificial pulses to maintain the TES at the desired operating temperature and to calibrate the energy response of the sensor during the data taking. For calibration purposes, a ⁵⁵Fe source (activity ~ 0.3 Bq) was installed on the crystals holder, at a distance of about 0.5 cm from the crystals. For more details about the experimental setup we refer to [5].

3 Energy reconstruction and data analysis

The detectors were operated in a dilution refrigerator at the Max-Planck-Institute for Physics in Munich, Germany, in an above ground facility without radiation shielding. To calibrate the energy spectra, for each detector we acquired a dedicated data set, in which, by operating the W-TES with a low bias current, we were able to maximize the dynamic range of the sensor. This was necessary to reconstruct the energy scale of the artificial pulses sent through the heater using the 5.9 keV line from the calibration source, which

would otherwise saturate the response of the sensor. We then optimized the operational condition of the W-TES, focused on achieving a low energy threshold, and we acquired a second set of data that was used to perform the analysis presented in this work. Thanks to the calibration of the heater response, we were able to reconstruct the energy scale also in the operational conditions dedicated to maximize the sensitivity to small energy deposits. For a more detailed description of the energy calibration procedure we refer to [5]. The data taking used in this work lasted 58.4 h and we collected statistics for a total exposure of 4.3×10^{-4} kg day. Both detectors achieved an excellent performance, reaching a baseline resolution of 3.54 eV and 3.42 eV respectively and energy thresholds of 19.7 eV and 16.8 eV, derived with the method described in [5].

3.1 Data processing

The data has been recorded as a continuous stream with 25 kHz sampling frequency, using a 16 bit digitizer from National Instruments (NI USB-6218 BNC). The complete stream was then processed offline with an optimum filter, to optimize the trigger threshold. Such a filter provides the theoretically best signal to noise ratio for the sought-for signal shape (for more details, see e.g.[10]). It was created from the noise power spectrum of the specific noise conditions of the measurements, and from the shape of an averaged particle event, also called standard event.

During data processing, the data stream was first divided into windows of 655 ms around the triggered timestamp (in case of multiple events in the same time window, the highest pulse in the window is set at the correct position) and then some parameters that describe the shape of the pulses and of the baseline (e.g. pulse height, difference of the average baseline values at the beginning and at the end of the window and RMS of the baseline) were calculated. Figure 1 shows an example of an event (black), as well as its filtered version (grey).

3.2 Event selection

In the analysis procedure, we used the same filter used for the offline triggering also for the amplitude estimation at the trigger position. We extracted additional parameters from the filtered data, in particular, the amplitude value evaluated by the filter and the filter RMS which quantifies the difference between the filtered pulse and the filtered standard event. The latter determines the deviation of the particle pulse shape from the one of the standard event that was used to create the optimum filter. Using all these parameters, we applied several cuts to remove artifacts and to select only windows where we could assure a correct amplitude reconstruction of the pulse.

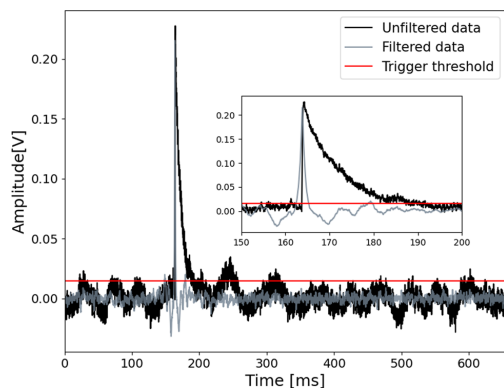


Fig. 1 Example of a particle event. In black the data stream is presented, while in grey the filtered data can be seen. The inset shows a zoom into the pulse. The red line represents the trigger threshold

The main artifacts in our data set were caused by the fast rise time of the pulses. The readout electronic was too slow for high energetic pulses and caused a reset of the baseline with respect to the pre-trigger range which deformed the pulse shape. Given that these artifacts have different baseline values before and after the reset, they were easily removed by selecting only events with a small difference of the average of the baseline at the beginning and at the end of the window.

We also accepted only those events with the best noise condition and therefore discarded events with a high baseline RMS. Finally, we excluded remaining artifacts and distorted pulse shapes by applying a cut on the ratio of the filter RMS and the filter amplitude.

We removed several hours at the beginning of the data taking where the detector response was very unstable. The stability check was performed by injecting heat pulses through the resistor on the detectors for the entire duration of the measurement with the purpose of monitoring the detector response over time. After this stability cut, our final data set counted 37.08 h measuring time that resulted in an exposure of 0.27 g day.

Finally, the acquired data were calibrated using the procedure described at the beginning of the section (see [5] for more details).

3.3 Trigger efficiency and survival probability

Once we obtained a calibrated energy spectrum for each detector, we also performed a simulation to estimate the signal survival probability (or cut efficiency), i.e. with which probability valid signal events survive the data processing and cleaning steps. We simulated particle-like events with a flat energy spectrum from 0 until the end of the dynamic

range of each detector which is 1.4 keV for detector 1 and 0.45 keV for detector 2.

These events were simulated by superimposing scaled standard particle events on our real data stream at random times. The voltage amplitude of each simulated pulse was determined with a specific time-dependent detector response function to account for the effect of instabilities. The detector response of each point in time could be studied with the heater pulses. By applying the identical analysis steps as for real data we studied the probability of signal events surviving the trigger algorithm and our quality cuts. To avoid an overestimation of the signal survival probability we removed events where the simulated and the reconstructed amplitude differed by more than 3 times the baseline resolution of the detector (with this cut we removed simulated events under threshold that coincided with strong upward fluctuations of the baseline). The result of the trigger and survival probability can be seen in Figs. 2 and 3.

In Fig. 2, we plotted only the trigger efficiency that we determined with a dedicated simulation in a limited energy range until 0.1 keV to enhance the statistics at low energies. With this simulated data set we calculated the ratio of the triggered events to the total number of simulated events and fitted it with an error function. We expect the energy threshold to be at the simulated energy value where the error function drops below half of its constant value. With the fit we obtained the value of (19.7 ± 5.1) eV for detector 1 and (16.1 ± 4.4) eV for detector 2. This confirms our previous energy threshold cited in [5] which was calculated by simply converting the voltage threshold into eV using a calibration factor. For the determination of the trigger efficiency and the survival probability over the whole dynamic range of the two detectors we used a second set of simulated data. The results are presented in Fig. 3. For typical underground measurements of CRESST, the trigger efficiency is constant throughout the whole energy range at a level of $\sim 80\%$. This trigger efficiency includes dead time mostly due to the removal of unstable periods and to a lesser extent due to pile-up with heater pulses or other events. In above ground measurements the total event rate is much higher leading to a much higher pile-up probability. This leads to a lower trigger efficiency of only $\sim 65\%$ at higher energies. Since during the trigger process in case of multiple pulses in the same time window, only the largest one was tagged as triggered, the trigger efficiency is even lower at low energies. This energy dependence of the trigger efficiency is enhanced due to an artifact caused by high energy particles. The fast rise of these pulses caused resets of the baseline that resulted in pulses being assigned a fixed wrong amplitude (calibrated at about 1.1 keV in detector 1 and around 0.2 keV in detector 2). Events smaller than this amplitude were hidden by this artifact and were therefore tagged as not triggered. Such energy dependence is not

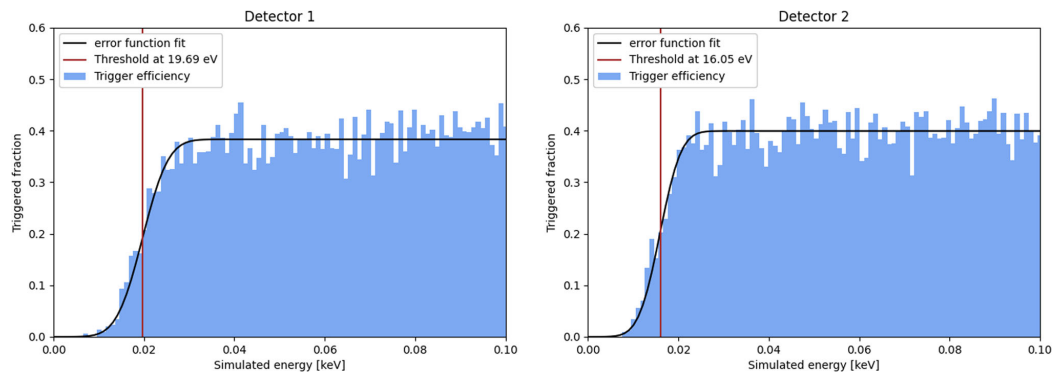


Fig. 2 Confirmation of the energy threshold of detector 1 and 2 using simulated data. We plotted the trigger efficiency against the simulated energy value (blue) and fitted the distribution with an error function (black line). We expect the threshold value to be at the energy value where the trigger efficiency drops below half of the constant trigger

efficiency at higher energies. For detector 1 the threshold value is (19.7 ± 5.1) eV while for detector 2 it is (16.1 ± 4.4) eV (brown lines). For both detectors the threshold of the previous publication of 19.7 eV and 16.8 eV are within the fit errors

present in the signal survival probability since pulses with the incorrect pulse shape are effectively removed.

We fitted the survival probability with an error function considering a flat survival probability at high energies. With this fit we estimated a survival probability of 25.8% in detector 1 and one of 39.8% in detector 2. As can be seen, by comparing the survival probability (brown) with the trigger efficiency (blue) the quality cuts don't remove a significant number of signal events at low energies, where the efficiency is mainly reduced by the trigger algorithm. At higher energies, the quality cuts remove events that could not be correctly reconstructed due to baseline jumps occurring in their vicinity.

Figure 4 shows the final calibrated spectra for both detectors corrected with the corresponding survival probability. For better visualization both detectors are plotted up to the same energy value of 0.45 keV, which corresponds to the end of the dynamic range of detector 2 and starting from the energy value where both detectors have a constant survival probability.

4 Dark matter results

The final energy spectra of our analysis (Fig. 4) show a rise of events towards low energies. This is an effect that is not new to the scientific community, as it has been observed in many other experiments operated both underground and above ground, as described in [11]. We conservatively consider these events as potential signal and calculate exclusion limits adopting Yellin's optimum interval method [12, 13]. The upper limit on the elastic spin-independent DM-nucleon

interaction is derived by comparing for each DM particle mass the observed spectrum with the expected one, corrected with the detector response as obtained by simulation. For the calculation of the expected differential energy spectra we adopted the standard DM halo model, with an asymptotic velocity of $v_{\odot} = 220$ km/s [14], a local DM density of $\rho_{\text{DM}} = 0.3$ (GeV/c²)/cm³ [15] and the galactic escape velocity of $v_{\text{esc}} = 544$ km/s [16].

The resulting elastic spin-independent DM-nucleon scattering cross section exclusion limits with 90% confidence level are shown in Fig. 5. A zoomed in version of it can be seen in Fig. 6. In these plots we are comparing the exclusion limits obtained with the diamond detector only to the previous CRESST results, in order to highlight the potential of the use of this new material compared to standard CRESST detectors.

One can clearly observe that, due to the light nucleus, the diamond detectors are extending the excluded parameter space to lower DM masses compared to the previous best above ground limits of CRESST [17] (dashed black in Figs. 5 and 6), that was obtained using a 0.5 g sapphire detector with an energy threshold of 19.7 eV. Using the detector 2 results it was possible to exclude masses until 0.122 GeV/c². For large dark matter masses the sensitivity of all the above ground measurements is limited by the low exposure and by the background.

The green curve shows as a reference the current best limit from CRESST for masses below 0.16 GeV, which was obtained with a 0.35 g silicon wafer detector with a threshold of 10 eV in the well shielded underground setup of CRESST at the LNGS [4]. The lower background in the below ground measurement leads to a much better limit at higher masses.

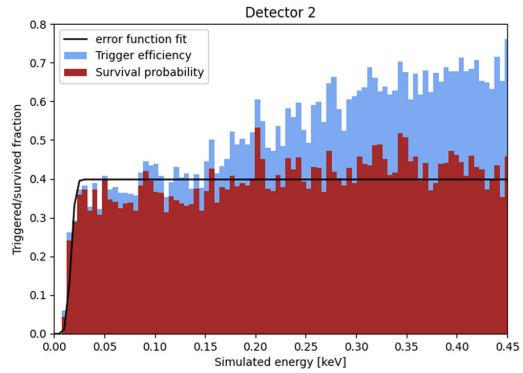
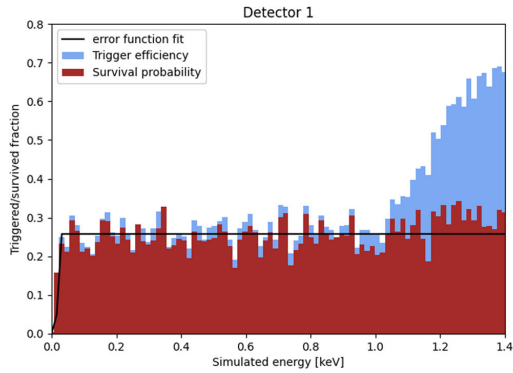


Fig. 3 Trigger efficiency (blue) and survival probability (brown) of detector 1 and 2. We calculated the probability of simulated events surviving the trigger and the quality cuts. The distribution of the survival

probability has been fitted with an error function (black line). The constant survival probability of detector 1 is 25.8 % while of detector 2 it is 39.8%

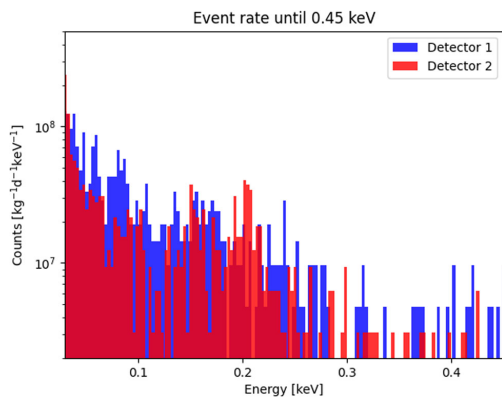


Fig. 4 Event rate per kg day keV corrected with survival probability. We plotted the calibrated spectrum after trigger and quality cuts and corrected each energy bin of the size of 3 eV with the constant survival probability. The spectra are plotted starting from the energy value at which the survival probability is constant for both detectors (0.03keV). Detector 2 (red) is plotted until the end of its dynamic range (0.45 keV) while detector 1 (blue) is plotted only until 0.45 keV for a better visualization

At low masses the diamonds cover a similar range compared to the silicon results despite the higher threshold. This highlights again the advantage of using a material with light target nuclei and demonstrate the potential of using diamond as a target in cryogenic detectors for low mass direct dark matter searches.

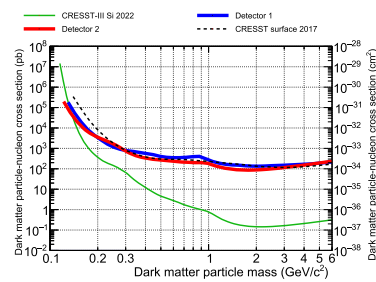


Fig. 5 Exclusion limits for the elastic spin-independent DM-nucleon scattering cross section at 90% CL, calculated for detector 1 (blue) and 2 (red) using Yellin’s optimum interval method. In black, the previous best above ground exclusion limits of CRESST are plotted [17]. In green, the best exclusion limits below 0.160 GeV/c² from CRESST underground measurements [4] are plotted as a benchmark reference

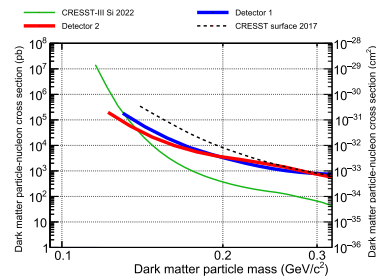


Fig. 6 Zoomed in version of Fig. 5. From this picture it is more evident how detector 1 (blue) and 2 (red) are excluding additional parameter space compared to the previous best above ground limits

5 Conclusions

These results demonstrate the potential of cryogenic detectors using diamond as target material for direct DM searches. In particular, their properties make them an ideal material for low-threshold experiments. With this proof-of-principle measurement we reach an energy threshold of 16.8 eV on the best performing detector, which allows for a sensitivity to DM masses down to $0.122 \text{ GeV}/c^2$.

Figures 5 and 6 show how thanks to the lighter nucleus diamond could exclude a larger parameter space compared to the previous best above ground measurement which had a comparable threshold and exposure. The difference with respect to the best underground limit has to be attributed not only to the different mass of the nucleus but also on the differences in energy threshold, exposure and low energy background, the origin of which is not yet known [11].

Diamond has the potential to be sensitive to a larger parameter space than the one presented in this work by pushing down the energy threshold and reduce the background in an underground measurement. Therefore, we are planning to extend our research with this material. In particular we aim to reach a higher exposure using larger crystals, and a better performance thanks to an improved read-out chain and an optimized W-TES sensor design. With these improvements, cryogenic diamond detectors will have the possibility to explore new properties for the interaction of sub-GeV DM with ordinary matter.

Acknowledgements This research was supported by the Excellence Cluster ORIGINS which is funded by the Deutsche Forschungsgemeinschaft (DFG, German Research Foundation) under Germany's Excellence Strategy - EXC-2094 - 390783311.

Data Availability Statement This manuscript has no associated data or the data will not be deposited. [Authors' comment: The data will be published respecting the time needed by the collaboration approval.]

Code Availability Statement The manuscript has no associated code/software. [Author's comment: No code/software was generated for the presented work.]

Open Access This article is licensed under a Creative Commons Attribution 4.0 International License, which permits use, sharing, adaptation, distribution and reproduction in any medium or format, as long as you give appropriate credit to the original author(s) and the source, provide a link to the Creative Commons licence, and indicate if changes were made. The images or other third party material in this article are included in the article's Creative Commons licence, unless indicated otherwise in a credit line to the material. If material is not included in the article's Creative Commons licence and your intended use is not permitted by statutory regulation or exceeds the permitted use, you will need to obtain permission directly from the copyright holder. To view a copy of this licence, visit <http://creativecommons.org/licenses/by/4.0/>.

Funded by SCOAP³.

References

1. P. Salucci, *Found. Phys.* **48**(10), 1517 (2018)
2. R. Massey et al., *Rep. Prog. Phys.* **73**(8), 086901 (2010). <https://doi.org/10.1088/0034-4885/73/8/086901>
3. Planck collaboration, N. Aghanim et al., *Astron. Astrophys.* **641**, A6 (2020). <https://doi.org/10.1051/0004-6361/201833910>
4. CRESST collaboration, G. Angloher et al., *Phys. Rev. D* **107**, 122003 (2023). <https://doi.org/10.1103/PhysRevD.107.122003>
5. A.H. Abdelhameed et al., *Eur. Phys. J. C* **82**(9), 851 (2022). <https://doi.org/10.1140/epjc/s10052-022-10829-5>
6. S. Pirro, P. Mauskopf, *Annu. Rev. Nucl. Part. Sci.* **67**(1), 161 (2017)
7. K. Pretzl, *Nucl. Instrum. Methods Phys. Res. Sect. A* **454**(1), 114 (2000)
8. N. Kurinsky et al., *Phys. Rev. D* **99**, 123005 (2019). <https://doi.org/10.1103/PhysRevD.99.123005>
9. S.M. Griffin et al., *Phys. Rev. D* **101**(5) (2020). <https://doi.org/10.1103/PhysRevD.101.055004>
10. E. Gatti, P.F. Manfredi, *La Rivista del Nuovo Cimento* (1978-1999) **9**(1), 1 (1986). <https://doi.org/10.1007/BF02822156>
11. P. Adari et al., *SciPost Phys. Proc.* **001** (2022). <https://doi.org/10.21468/SciPostPhysProc.9.001>
12. S. Yellin, *Phys. Rev. D* **66**, 032005 (2002). <https://doi.org/10.1103/PhysRevD.66.032005>
13. S. Yellin (2007). [arXiv:0709.2701](https://arxiv.org/abs/0709.2701)
14. F.J. Kerr, D. Lynden-Bell, *Mon. Not. R. Astron. Soc.* **221**(4), 1023 (1986). <https://doi.org/10.1093/mnras/221.4.1023>
15. P. Salucci, F. Nesti, G. Gentile, C.F. Martins, *Astron. Astrophys.* **523**, A83 (2010). <https://doi.org/10.1051/0004-6361/201014385>
16. M. Smith et al., *Mon. Not. R. Astron. Soc.* **379**(2), 755 (2007). <https://doi.org/10.1111/j.1365-2966.2007.11964.x>
17. CRESST collaboration, G. Angloher et al., *Eur. Phys. J. C* **77**(9), 637 (2017). <https://doi.org/10.1140/epjc/s10052-017-5223-9>

Acknowledgments

I would like to use this last page to thank all the people who made this work possible. First of all, I would like to thank Prof. Dr. Otmar Biebel for his supervision, good advice, and valuable feedback throughout these years.

A special thanks goes to Federica Petricca for giving me the opportunity to join the CRESST group at the MPP. Thank you for your excellent supervision throughout these years, accurate proofreading of this thesis, and valuable feedback. In the last three years, I have learned so much from you, and the great working environment you created made me always feel valued and supported, making my stay at the CRESST MPP group a wonderful experience.

Therefore, a big thank you goes, of course, to all the members of the group, present and past. Thank you for everything I have learned from each of you and for all the good time we have had together.

In particular, I am very thankful to Michele Mancuso, who was always explaining me with enthusiasm all the activities in the lab despite his very tight schedule.

I am also very grateful to Lucia Canonica, who included me in the diamond project, and with whom I really enjoyed working.

Thank you to Abhijit Garai, Heerak Benerjee, Antonio Bento, Pedro Guillaumon, and Beatrice Mauri for contributing to the proofreading of this thesis.

A big thanks also goes to the CRESST analysis group. Thanks to everyone who participated in the discussions in our meetings, from which I learned so much. A special thank you goes to Martin Stahlberg for always helping me whenever I needed assistance on the software side.

Thank you to all the members of the CRESST collaboration, especially the Gran Sasso team, without whom the data presented in this work would not exist.

On a more personal note, I would like to thank Francesca Pucci, Dominik Fuchs, and Vanessa Zema for being not only great co-workers but also amazing friends. Thank you for all the fun we had together and all the help you gave me throughout these years. Knowing you significantly improved my experience as a PhD student.

Last but not least, I would like to thank my parents and my sister who always supported me during my studies, and Miguel who always helps me see the bright side of everything.